AD-A118 973 FOREIGN TECHNOLOGY DIV WRIGHT-PATTERSON AFB OH F/G 12/1
ACTA AERONAUTICA ET ASTRONAUTICA SINICA.(U)
JUL 82
UNCLASSIFIED FTD-ID(RS)T-0518-82 NL

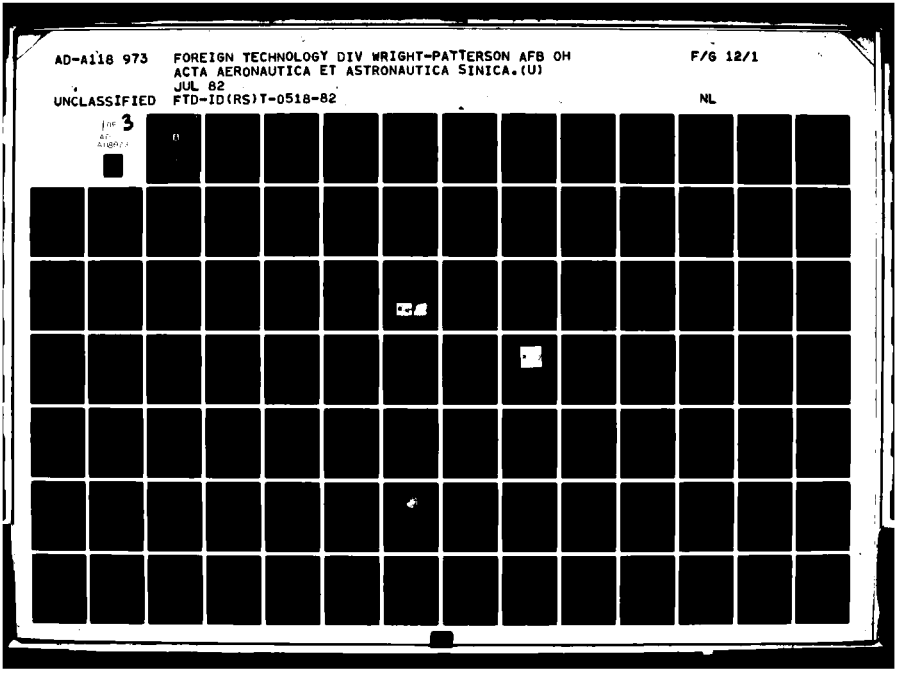

FTD-ID(RS)T-0518-82

FOREIGN TECHNOLOGY DIVISION

ACTA AERONAUTICA ET ASTRONAUTICA SINICA

Approved for public release;
distribution unlimited.

EDITED TRANSLATION

FTD-ID(RS)T-0518-82 28 July 1982

MICROFICHE NR: FTD-82-C-001024

ACTA AERONAUTICA ET ASTRONAUTICA SINICA

English pages: 212

Source: Acta Aeronautica et Astronautica Sinica, Vol. 2, Nr. 4, December 1981 pp. 1-103

Country of origin: China
Translated by: LEO KANNER ASSOCIATES
F33657-81-D-0264
Requester: FTD/TQTA

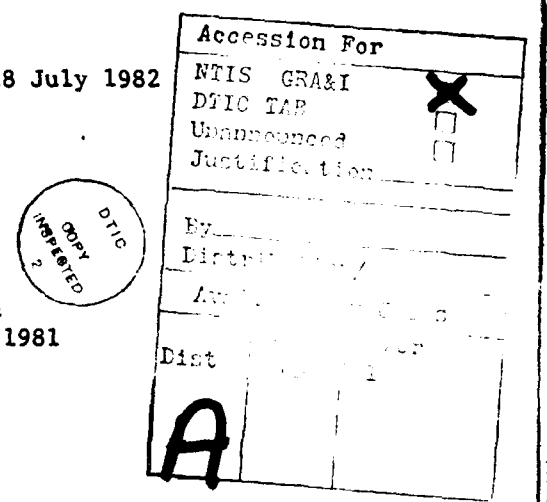

PREPARED BY:

TRANSLATION DIVISION
FOREIGN TECHNOLOGY DIVISION
WP-AFB, OHIO.

ACTA AERONAUTICA ET ASTRONAUTICA SINICA

(Quarterly)

Volume 2 Number 4 December 1981

CONTENTS

RESEARCH NOTES

SOCIETY NEWS

(See next page)

SOCIETY NEWS

GRAPHICS DISCLAIMER

All figures, graphics, tables, equations, etc. merged into this translation were extracted from the best quality copy available.

NUMERICAL SOLUTION FOR THE SUPERSONIC INVISCID FLOW AROUND NON-SYMMETRICAL BODIES

by Guo Zhiquan and Zhang Lumin
(Aerodynamic Research and Development Center of China)

Abstract

This paper describes a numerical method for evaluation of the three-dimensional inviscid supersonic flow around the re-entry vehicles of non-symmetrical bodies. The method is devoted to determining the initial-boundary value problem for three independent variable first order stationary quasi-linear hyperbolic partial differential equations. MacCormack's explicit finite difference schemes with second order accuracy is adopted.

The numerical examples of the bent sphere cones and the re-entry vehicles with control flaps have been worked out to demonstrate the capability of this computation method. The accuracy of this technique has been found to be satisfactory.

Symbols

A	the total drag on the body's surface in front of the solution section
a	local sonic velocity ($a=\sqrt{\gamma P/\rho}$)
a_e, b_e	the curvilinear - ellipsoid long and short semi-axes of the body's surface on the solution section (see figs. 1 and 2)
C_p	pressure coefficient on surface $\left(C_p=\frac{P-1}{\frac{1}{2}\gamma M_\infty^2}\right)$
J_o, K_o	total number of radial and peripheral solution crunodes in the solution section

M, M_∞	local and free flow Mach numbers
P	pressure
r, z, φ	radial, axial and peripheral (meridian angle) coordinates in the cylindrical coordinate system
r_b, r_s	the heights of the body's surface and shock wave surface (radial)
$r_{b_z}, r_{s_z}, r_{b_\varphi}, r_{s_\varphi}$	the first order derivatives of r_b or r_s for the lower angular coordinates
$r_{b_{zz}}, r_{b_{z\varphi}}, r_{b_{\varphi\varphi}}$	the second order derivatives of for the lower angular coordinates
R_N	flow around blunt nose radius of body
S	entropy ($S=P/\rho\gamma$)
u, v, w	axial, radial and peripheral velocity components
$u_\infty, v_\infty, w_\infty$	axial, radial and peripheral components of free flow velocity
$V_{n\infty}$	normal velocity in front of shock wave
α	free flow attack angle
γ	specific heat ratio, $\gamma=1.4$ in ideal gas
$\Delta z, \Delta\xi, \Delta\Phi$	axial radial and peripheral network step lengths
δ_N	included angle (below called bent angle) of front and back cone axes
ζ_1	included angle of the tapered plane and body axis (called "tapered surface angle" for short) in the "tapered cone"
ζ_2	included angle (control angle) of the control wing and body axis
$\theta_B, \theta_C, \theta_{FC}$	semi-cone angle of each cone
ξ, Φ	radial and peripheral coordinates after transformation
$\xi_r, \xi_z, \xi_\varphi$	first order derivatives of ξ for lower angular coordinates
ρ	density
Φ_φ	derivative of Φ for φ

Upper Corner Symbols

n	(axial) solution section code

Lower Corner Symbols

i	code of sectional cylindrical coordinate system
j,k	radial and peripheral codes of solution crunodes

I. Preface

The great majority of high performance maneuverable re-entry vehicles draw support from the non-symmetricality of the configuration to attain control moment and to cause it to produce a predetermined balanced angle of attack. In this way, there is then maneuvering flight. Therefore, attention must be given to the solution of the three-dimensional inviscid flow around non-symmetrical bodies.

The flow field of the supersonic inviscid flow can be divided into two sections according to differences in quality: the subsonic and transonic area, and the rear supersonic area. This paper only discusses the solution of the rear supersonic area and the nose flow fields are taken from references [3,4].

Solutions for the rear area of non-symmetrical bodies began during the 1960's in foreign nations and during the 1977-1979 period many technical achievements were attained. By the end of 1979, domestic work showed results as seen in references [1,2]. The major distinctions of this paper are:

(1) The coordinate systems are different. For bent sphere cones, different oriented cylindrical coordinate systems are used in different cone regions yet they are not the coordinate systems where "the original points of the coordinates shift along the body's axis and the direction is invariant."

(2) The beginning equations are a set of conservation law flow equations whose differential forms are separately given in reference [2].

(3) There are differences in the solution method for the body's surface.

(4) When there was a relative lack of experimental and numerical computations, we used the total mass, total energy and total momentum conservation examination technique.

The method used in this paper can be extended to situations where there is non-symmetrical yaw (slip angle) and the results obtained were satisfactory (to be published in a separate article).

We would like to thank Zhang Hanxin, Li Songbo and Lao Shuchun for all of their help in the work for this paper.

II. Basic Equations and Boundary Conditions

1. The Selection of the Coordinate Systems[1]

The bent sphere cones (including the multiple region bent vehicle) were mostly multiple region cones and the body's axis was not on the same straight line. Therefore, different body axis cylindrical coordinate systems o_i-$z_i r_i \varphi_i$ were used for the different cone regions. Given this type of regional cylindrical coordinate system, each region's corresponding basic equation had completely identical forms. To be sure, the joining areas of the front and back coordinate systems could present trouble: firstly, as the beginning surface $Z_{i+1}=Z_{i+1,o}$ of the back axis coordinate system computation, we must give the "initial value"; secondly, as the end region $(Z_{ei0} \leqslant Z_i \leqslant Z_{ei1})$ of the front axis

1. Zhang Hanxin offered valuable suggestions for the determination of the coordinate systems.

coordinate system computation, it not only has aerodynamic solution integral limitation problems but it also only provides interpolation data results for the above mentioned "initial values." These are easily resolved.

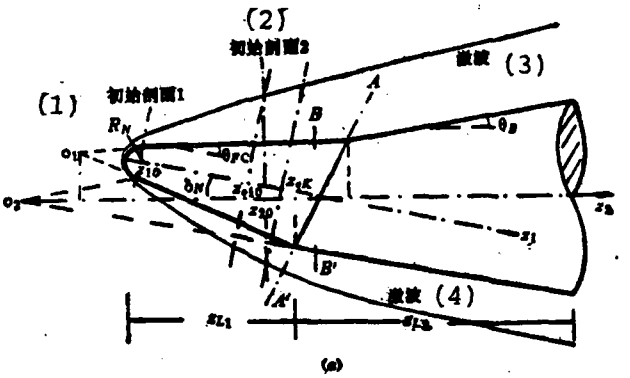

(a)

Fig. 1(a) Coordinate System and Sketch of a Bent Sphere Cone

Key: 1. Beginning section I
2. Beginning section II
3. Shock wave
4. Shock wave

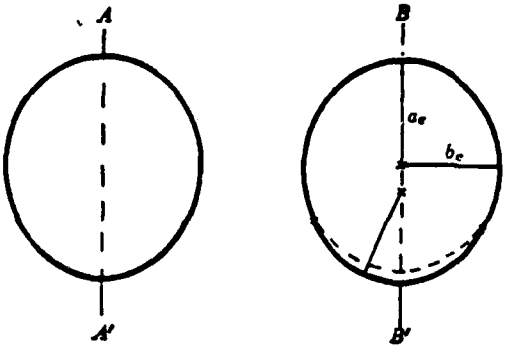

(b)

Fig. 1(b) Contour in Sections A-A' and B-B'

2. Basic Equations

In the (body's axis) cylindrical coordinate o-zrφ (omitting the lower angular coordinate i), if the body's surface and

shock wave surface are separately indicated as

$$r=\bar{r}_b(z,\ \varphi),\quad r=r_s(z,\ \varphi) \tag{1}$$

and we introduce the following transformations

$$z=z,\quad \xi=\frac{r-r_b}{r_s-r_b},\quad \Phi=\mathrm{tg}^{-1}\left(\frac{b_e}{a_e}\,\mathrm{tg}\,\varphi\right) \tag{2}$$

(for a_e and b_e see fig. 1(b)), using this type of non-dimensionalization: P and ρ are separately divided by free flow pressure P_∞ and free flow density ρ_∞ ; the velocity is divided by $\sqrt{P_\infty/\rho_\infty}$ z ; r etc. indicates that the length is divided by blunt nose radius R_N. Thus, the three-dimensional inviscid stationary flow equations are

$$\frac{\partial\vec{A}}{\partial z}+\frac{\partial\vec{B}}{\partial\xi}+\frac{\partial\vec{C}}{\partial\Phi}+\vec{D}=0 \tag{3}$$

$$u^2+v^2+w^2+\frac{2\gamma}{\gamma-1}P/\rho=C_0 \tag{4}$$

In the equations

$$C_0=\gamma M_\infty^2+\frac{2\gamma}{\gamma-1}$$

$$\vec{A}=(\rho u,\ \rho u^2+P,\ \rho uv,\ \rho uw)^T$$

$$\vec{B}=\xi_z\vec{A}+\xi_r\vec{B}^*+\xi_\varphi\vec{C}^*$$

$$\vec{C}=\left(\frac{a_e}{b_e}\sin^2\Phi+\frac{b_e}{a_e}\cos^2\Phi\right)\vec{C}^*$$

$$\vec{D}=\vec{D}^*-\xi_r(r_{b_z}-r_{s_z})\vec{A}-\left[\xi_r(r_{b_\varphi}-r_{s_\varphi})+\left(\frac{a_e}{b_e}-\frac{b_e}{a_e}\right)\sin 2\Phi\right]\vec{C}^*$$

and

$$\vec{B}^*=\begin{bmatrix}\rho v\\ \rho uv\\ \rho v^2+P\\ \rho vw\end{bmatrix},\quad \vec{C}^*=\frac{1}{r}\begin{bmatrix}\rho w\\ \rho uw\\ \rho vw\\ \rho w^2+P\end{bmatrix},\quad \vec{D}^*=\frac{1}{r}\begin{bmatrix}\rho v\\ \rho uv\\ \rho(v^2-w^2)\\ 2\rho vw\end{bmatrix}$$

The region of solution is

$$z_{i_0}\leqslant z_i\leqslant z_{ei},\quad 0\leqslant\xi_i\leqslant 1,\quad 0\leqslant\Phi_i\leqslant\pi\qquad(i=1,\ 2,\ \cdots)$$

3. Boundary Conditions

(1) On the body's surface (ξ =0), there are non-permeating conditions:

$$ur_{b_x}-v+wr_{b_\varphi}/r_b=0 \tag{5}$$

(2) On the shock wave surface (ξ =1), there is the Rankine-Hugoniot relational formula. It can be rewritten as

$$\left.\begin{aligned}
&V_{n\infty}^2=\frac{\gamma+1}{2}P+\frac{\gamma-1}{2}\\
&\rho=V_{n\infty}^2/(1+V_{n\infty}^2-P)\\
&r_{i_x}=-\frac{1}{u_\infty^2-V_{n\infty}^2}\{u_\infty(v_\infty-w_\infty r_{i_\varphi}/r_i)\\
&\qquad+V_{n\infty}\sqrt{(v_\infty-w_\infty r_{i_\varphi}/r_i)^2+(u_\infty^2-V_{n\infty}^2)(1+r_{i_\varphi}^2/r_i^2)}\}\\
&v=v_\infty+V_{n\infty}\left(1-\frac{1}{\rho}\right)/\sqrt{1+r_{i_x}^2+r_{i_\varphi}^2/r_i^2}\\
&u=u_\infty-(v-v_\infty)r_{i_x}\\
&w=w_\infty-(v-v_\infty)r_{i_\varphi}/r_i
\end{aligned}\right\} \tag{6}$$

In the equations, $V_{n\infty}$ is the normal velocity in front of the wave and u_∞, v_∞ and w_∞ are separately the (free flow) velocity components in front of the wave:

$$\left.\begin{aligned} u_\infty &= \sqrt{\gamma}\, M_\infty \cos\alpha \\ v_\infty &= -\sqrt{\gamma}\, M_\infty \sin\alpha \cos\Phi \\ w_\infty &= \sqrt{\gamma}\, M_\infty \sin\alpha \sin\Phi \end{aligned}\right\} \qquad (7)$$

(3) If we take into consideration the problem of maneuvering within the surface and that the body has a symmetrical surface ($\Phi = 0, \pi$) we can apply symmetrical conditions on it.

4. Initial Conditions

On the left end surface (initial section) $z_i = z_{io}$ of the solution region, the initial values of its flow field and shock wave parameters can be interpolated from the values of the upstream area.

For the initial boundary value problem of the set of hyperbolic equations (3), its applicable conditions are the initial value sections of the space towards the curved surface.

III. Differential Equations and Boundary Processing

If the equidistance on the variation region [0, 1] of ξ gives J_o crunodes, the distance between the crunodes is $\Delta\xi = (J_o - 1)^{-1}$; if the equidistance on the variation region of Φ gives K_o crunodes, $\Delta\Phi = \pi/(K_o - 1)$. In the solution of each layer along the axis, after the network point flow parameters on the $z = z^{(n)}$ section are known, all of the points on the $z = z^{(n+1)} = z^{(n)} + \Delta z$ section can be separately calculated as follows:

1. Calculation of Inner Points

In the network's inner points ($1 < j < J_o$, $1 < k < K_o$), MacCormack's explicit finite difference schemes with second order form are used for the structure of the set of equations (3):

$$\tilde{\vec{A}}_{j,k} = \vec{A}^n_{j,k} - \Delta z\left[(\vec{B}^n_{j+1,k} - \vec{B}^n_{j,k})/\Delta\xi + (\vec{C}^n_{j,k+1} - \vec{C}^n_{j,k})/\Delta\Phi + \vec{D}^n_{j,k}\right] \qquad (8)$$

$$\vec{A}^{n+1}_{j,k} = \frac{1}{2}\left\{\vec{A}^n_{j,k} + \tilde{\vec{A}}_{j,k} - \Delta z\left[(\tilde{\vec{B}}_{j,k} - \tilde{\vec{B}}_{j-1,k})/\Delta\xi + \left(\tilde{\vec{C}}_{j,k} - \tilde{\vec{C}}_{j,k-1}\right)/\Delta\Phi + \tilde{\vec{D}}_{j,k}\right]\right\} \qquad (8a)$$

Equation (8) is the predicted step, "$\sim$" is the predicted value and equation (8a) is called the correction step.

After each step of computation attained $\vec{A}_{j,k}$, the simultaneous Bernoulli integral can then obtain the predicted (or corrected) values of the flow field's inner point flow parameters $\vec{U}_{j,k} = (u, v, w, P, \rho)^T_{j,k}$.

2. Calculation of Shock Wave Surface

At this time, it is also necessary to determine shock wave parameters r_s, r_{s_z} and $r_{s\varphi}$. For this reason, the set of equations in (6) are not closed. We can simply use a method analagous to calculating the inner points (yet in the predicting step, we change to use the backwards difference quotient for the differential quotient of ξ). First we determine the wave and then the prediction or correction value of pressure $P_{Jo,k}$. As for r_s, we use the improved Youla (?) broken line method:

Predicted step —— $(\tilde{r}_s)_k=(r_s)^n_k+\Delta z(r_{s_z})^n_k$ (9)

Correction step —— $(r_s)^{n+1}_k=\frac{1}{2}\left[(r_s)^n_k+(\tilde{r}_s)_k+\Delta z(\tilde{r}_{s_z})_k\right]$ (9a)

$r_{s\varphi}$ is determined by using a central difference quotient

$$(r_{i_\varphi})_k=\begin{cases}0 & k=1,\ K_\varphi\\ \frac{1}{2\Delta\Phi}[(r_i)_{k+1}-(r_i)_{k-1}] & 1<k<K_\varphi\end{cases} \tag{10}$$

In this way, we can compute the flow parameters after the wave from equation (6) and the prediction values and correction values of the shock waves.

3. Computations of Body's Surface

On the body's surface, aside from the boundary conditions in equation (5) the flow should satisfy the following quasi-wave characteristic equation

$$\frac{\partial P}{\partial z}=-\frac{a(G-ur_{b_x})}{u^2-a^2}\left\{\xi_r\frac{\partial P}{\partial\xi}-\frac{1}{r_bG}\left[\Phi_\varphi\left(\frac{uw}{a}+\frac{u^2-a^2}{G-ar_{b_x}}\frac{r_{b_\varphi}}{r_b}\right)\frac{\partial P}{\partial\Phi}\right.\right.$$
$$+\rho au\xi_r r_\varphi\left(\frac{\partial v}{\partial\xi}-r_{b_x}\frac{\partial u}{\partial\xi}-\frac{r_{b_\varphi}}{r_b}\frac{\partial w}{\partial\xi}\right)-\rho a\Phi_\varphi\left(w\frac{\partial u}{\partial\Phi}-u\frac{\partial w}{\partial\Phi}\right)$$
$$\left.\left.+\rho uva\right]\right\}+\frac{\rho a}{G}\left[\left(u^2r_{b_{xx}}-\frac{w^2}{r_b}\right)+\frac{w}{r_b}(2ur_{b_{x\varphi}}-2vr_{b_\varphi}/r_b+wr_{b_{\varphi\varphi}}/r_b)\right] \tag{11}$$
(1)(其中 $G=\sqrt{u^2(1+r^2_{b_x}+r^2_{b_\varphi}/r^2_b)-a^2(1+r^2_{b_\varphi}/r^2_b)}$)

Key: 1. In the equation

and flow characteristic equations

$$\frac{\partial w}{\partial z} = -\frac{1}{r_\phi \mu}\left[w\Phi_* \frac{\partial w}{\partial \Phi} + \frac{1}{\rho}\left(\Phi_* \frac{\partial P}{\partial \Phi} - \xi_* r_{\phi_*} \frac{\partial P}{\partial \xi} \right) + vw \right] \tag{12}$$

$$\frac{\partial S}{\partial z} = -\frac{w}{r_\phi \mu} \frac{\partial S}{\partial \Phi} \Phi_* \tag{13}$$

We also used MacCormack's explicit finite difference schemes with second order form to calculate equations (11)-(13). When we considered the body's surface j=1, the differential quotients of ξ were all replaced by difference quotients when in the first and second order.

It must be pointed out that although the above method of computing the body's surface was able to accurately reflect the inviscid flow characteristics, yet for the computation of longer cone sections (for example, when its length is greater than 50 times the nose radius) and the leeward surface it cannot go down continuously. This is because as the rear body high entropy layer becomes thinner, the local Mach number on the body's surface becomes smaller. As soon as the axial velocity is subsonic, the applicable conditions of the initial boundary value problem of the hyperbolic equations are destroyed. For the the computation to go down continuously, the entropy must be decreased. We can begin from any suitable section and change and use the set of equations in (3), (4) and (5) (deleting the third equation in the equations of (3)). The large majority of experiment computations have shown that this type of non-strict decreased entropy method was functional and the computation results of the body's surface pressure were quite accurate.

4. Handling the "Singular Line" of the Body's Surface

On the "edge" of the non-continuous slope of the body's

surface, the flow is multi-valued. The non-continuity of the flow only occurs on the normal plane of the edge line. The points on the edge are "expansion angle points" or "compressed angle points." They are determined by whether the air flow deflection angle on the edge line normal plane of the point is positive or negative (if the body's surface curve on the normal plane is protruding, then the air flow deflection angle is defined as "positive", otherwise it is "negative"). After calculating the upstream flow value of a certain computed point on the edge, we used the method found in reference [1] to determine the downstream flow value of the point. However, there is an error in equation (4.9) in reference [1] and it should be changed to

$$\left.\begin{aligned} &\chi^3+c_1\chi^2+c_2\chi+c_3=0\\ &c_1=-(1+2/M^2)-\gamma\sin^2\theta_1\\ &c_2=(2M^2+1)/M^4+[(\gamma+1)^2/4+(\gamma-1)/M^2]\sin^2\theta_1\\ &c_3=-\cos^2\theta_1/M^4 \end{aligned}\right\} \qquad (14)$$

Here, χ is the sine square of the shock wave angle and θ_1 is the air flow deflection angle.

IV. Stability Conditions

Step length Δz must be limited by the stability conditions. A necessary condition for MacCormack's explicit finite difference equations is that for any one point in the solution region, the dependence region of the differential equation should be completely included in the dependence region of the difference equation, that is

$$\frac{\Delta\xi}{\Delta z}\geqslant \max_{\substack{1\leqslant j\leqslant J_0\\ 1\leqslant k\leqslant K_0}}\{(\sigma_1)_{j,k},\ (\sigma_2)_{j,k},\ (\sigma_3)_{j,k}\} \qquad (15)$$

In the formulas

$$\sigma_1=\frac{1}{u^2-a^2}\left\{\left|u\left(u\xi_x+v\xi_r+w\xi_\varphi/r\right)-a^2\xi_x\right|\right.$$
$$\left.+a\sqrt{\left(v\xi_r+w\xi_\varphi/r\right)^2+\left(u^2-a^2\right)\left(\xi_r^2+\xi_\varphi^2/r^2\right)}\right\}$$

$$\sigma_2=\frac{\Phi_\varphi}{r\left(u^2-a^2\right)}\frac{\Delta\xi}{\Delta\Phi}\left\{|uw|+a\sqrt{u^2+w^2-a^2}\right\}$$

$$\sigma_3=\frac{1}{u^2-a^2}\left\{\left|u\left[u\xi_x+v\xi_r+\frac{w}{r}\left(\xi_\varphi+\Phi_\varphi\frac{\Delta\xi}{\Delta\Phi}\right)\right]-a^2\xi_x\right|\right.$$
$$\left.+a\sqrt{\left[v\xi_r+\frac{w}{r}\left(\xi_\varphi+\Phi_\varphi\frac{\Delta\xi}{\Delta\Phi}\right)\right]^2+\left(u^2-a^2\right)\left[\xi_r^2+\left(\xi_\varphi+\Phi_\varphi\frac{\Delta\xi}{\Delta\Phi}\right)^2/r^2\right]}\right\}$$

Because of this

$$\Delta z=\mu\Delta\xi/\max_{\substack{1\le j\le J_0\\ 1\le k\le K_0}}\left\{(\sigma_1)_{j,k},\ (\sigma_2)_{j,k},\ (\sigma_3)_{j,k}\right\} \tag{16}$$

μ can generally take 0.9

V. Computation Examples

1. Cone - Cylinder - Flare Symmetrical Bodies

We programmed and computed the bent sphere cone $(\delta_N=0)$. It can be seen from fig. 2 that the two types of computations are basically the same and match well the experimental results.

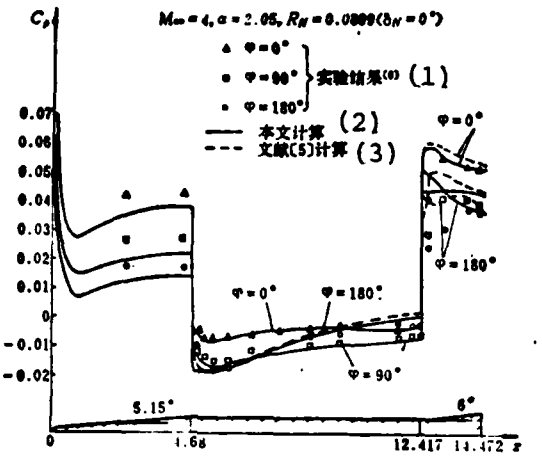

Fig. 2 C_p Curves as Compared to Computational Results of [5] and the Experimental Results of [6]

Key: 1. Experimental results of [6]
2. *Computations of this paper*
3. Computations of reference [5]

2. Bent Sphere Cone

The flow fields were computed for the configurations shown in fig. 1(a), $\theta_{FC}=10^\circ$, $\theta_B=5^\circ$, under different bend angles ($\delta_N=0^\circ \sim 6^\circ$), different free flow Mach numbers (M_∞ =5,8,10) and different attack angles ($a=0^\circ \sim 10^\circ$). Fig. 3 gives the partial pressure distribution curve and fig. 4 presents the pressure of the different bend angles (x_{C_p}/L) which change the curve in accordance with the attack angle and have similar variation tendencies as reference [2] (in this reference, they only give the curve but no measurements so that there is no way of making a quantitative comparison).

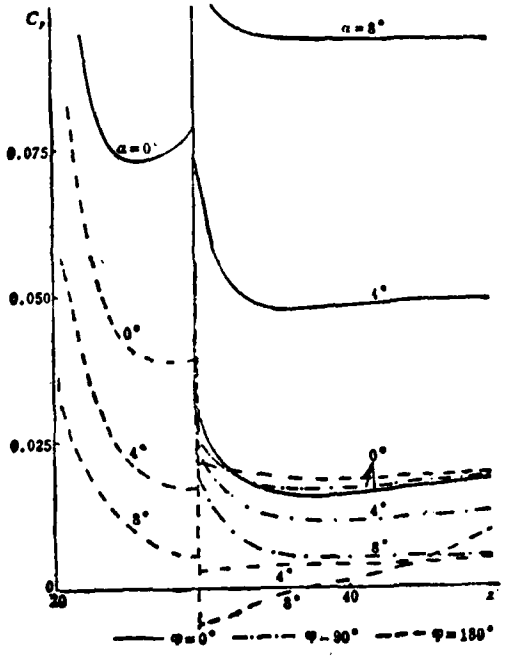

Fig. 3 Pressure Distribution of a Bent Sphere Cone

$M_\infty = 5,\ \theta_{FC}=10^\circ,\ \theta_B=5^\circ,\ \delta_N=2^\circ$

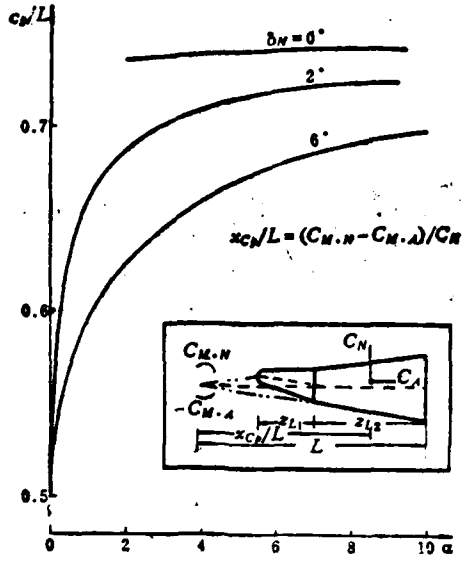

Fig. 4 x_{C_p}/L Vs. a Curves of a Bent Sphere Cone

$M_\infty = 8$, $\theta_{FC} = 10^\circ$, $\theta_B = 5^\circ$, $z_{L1} = 9.8$, $z_{L2} = 20$

3. Tapered Cone With Control Flaps

Its configuration is shown in fig. 5.

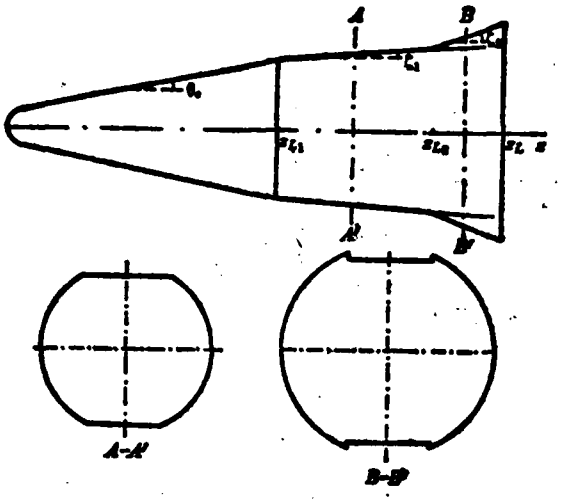

Fig. 5 Sketch of a Tapered Cone With Control Flaps

We computed different free flow Mach numbers M_∞ =5 and 10, different attack angles $\alpha=0^\circ \sim 10^\circ$ and different body shapes (tapered on a single surface, on two surfaces, on four surfaces etc.) for $\theta_c=10^\circ$, $\zeta_1=7.5^\circ$ and $\zeta_2=14.5 \sim 21^\circ$. Fig. 6 gives a set of pressure distribution curves.

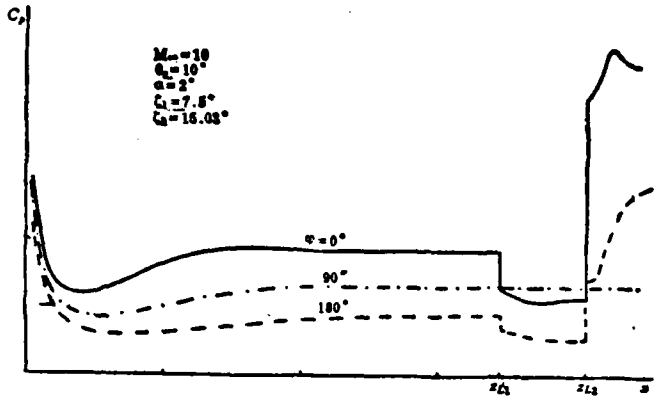

Fig. 6 Pressure Distribution of a Tapered (on Both Sides) Cone With Control Flaps

4. Tapered Double Cone

This is the bent-tapered cone (δ_N=0) and is the only complete results found in the references. This paper uses the "bent-tapered cone" sequence to carry out computations and a comparison with the results of reference [1] are derived from fig. 7 and listed in the following table:

φ / z	0° (2) 本(1)文	0° (2) 文献[1]	30° (3) 本 文	30° (4) 文献[1]	90° (5) 本 文	90° (6) 文献[1]	(7)计算网格 (8) 本 文	(7)计算网格 (10) 文献[1]
1	0.3569	0.3576	0.3357	0.3362	0.2238	0.2246	$J_0=21$ $K_0=13$	$J_0=15$ $K_0=13$
15	0.4402	0.4399	0.4079	0.4074	0.2336	0.2331		
34.1	0.0746	0.0744	0.0646	0.0643	0.0196	0.0195	$J_0=21$ $K_0=13$	$J_0=15$ $K_0=25$
35.6	0.0497	0.0354*	0.0645	0.0642	0.0195	0.0194		
38.6	0.0347	0.0383*	0.0625	0.0624	0.0193	0.0193		
40.6	0.0362	0.0381*	0.0599	0.0603	0.0193	0.0193	$J_0=21$ $K_0=25$ (等距)(9)	$J_0=15$ $K_0=33$ [0°,96°]内25个等距点，[96°,π]内8个非等距点(11)
43.1	0.0375	0.0378	0.0561	0.0563	0.0194	0.0194		
44.6	0.0373	0.0375	0.0536	0.0538	0.0193	0.0194		

(12)表中φ=30°，90°的值[1]是经作者插值得到的。

Table 1

Key: 1. This paper
2. Reference [1]
3. This paper
4. Reference [1]
5. This paper
6. Reference [1]
7. Computation network
8. This paper
9. Equidistance
10. Reference [1]
11. 25 equidistant points in $[0^\circ, 96^\circ]$, 8 non-equidistant points in $[96^\circ, \pi]$
12. The values of $\varphi = 30^\circ$ and 90° in this table [1] are interpolations made by the authors

There is only a 0.2 percent difference between the two in front of the "tapered surface." The difference within the "tapered surface" is somewhat larger and the largest difference occurs on the extreme left end of the "tapered surface." The reason for this is that reference [1] does not use equal entropy relational formula (13) in computing the body's surface but rather uses the so-called decreased entropy method (the entropy attained by interpolating the inner point entropy on the body's surface). In two types of computations, the upstream pressure value on the left end point of the "tapered surface" (z=35, $\varphi = 0^\circ$) were

identical. Due to the decreased entropy, the point's upstream density was higher than the value of the equal entropy method (reference [1] does not give density values and thus no comparison can be made), and the local Mach number was higher and because of this expanded sharply. Therefore, the point's downstream pressure value was also lower. The differences in the initial end of the "tapered surface" which was caused by the different handling of the entropy had a very small effect on the pressure of the body's surface outside the "tapered surface." Even inside the "tapered surface" its differences also gradually decreased and disappeared in accordance with the downstream propulsion.

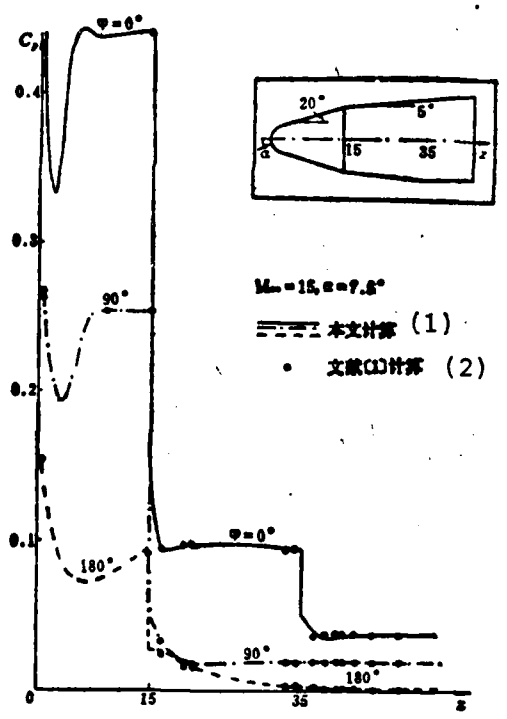

Fig. 7

Fig. 7 Pressure Distribution of a Tapered Double Cone as Compared With the Results of Reference [1]

Key: 1. Computations of this paper
2. Computations of reference [1]

VI. Analysis of Precision

Given that there is a lack of comparison of experimental and other numerical computations, to examine the reliability of this method, we mainly used the total mass, total energy and total momentum conservation technique to carry out investigations.[1]

The shock wave on the solution section was taken as the outward boundary to make a flow tube. If the outer flow control surface is S_o, the annular region between the shock wave and body's surface on the solution surface is S_1. The total mass and total momentum are recorded as G_o and M_o, and the corresponding symbols on S_1 are G_1 and M_1. Furthermore, if the body surface's total drag in front of the solution section is A, then the total mass and total momentum conservation can be written as:

$$G_0 = G_1 \tag{17}$$

$$M_0 = M_1 + A \tag{18}$$

1. Zhang Hanxin and Gao Shuchun participated in discussions of this problem.

Noted as

$$\Delta G = \frac{G_0 - G_1}{G_0} \tag{19}$$

$$\Delta M = (M_0 - M_1 - A)/M_0 \tag{20}$$

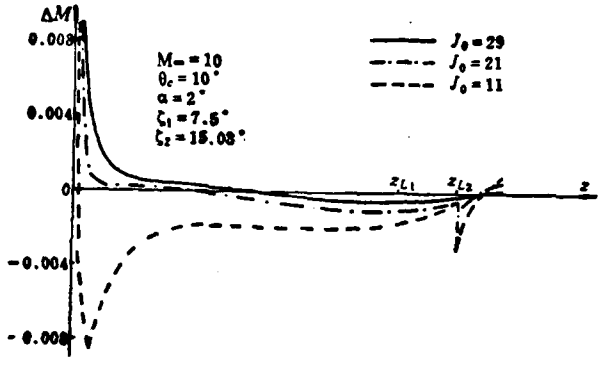

Fig. 8 Errors of Computed Total Momentum of a Tapered Cone With Control Flaps

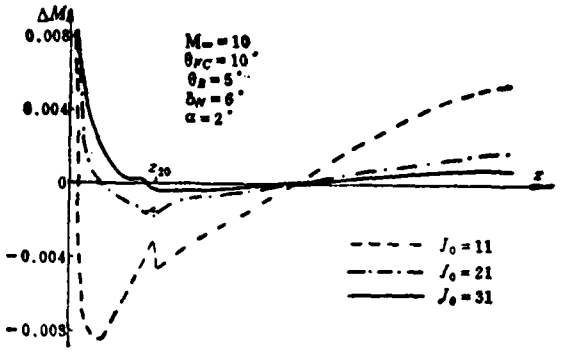

Fig. 9 Errors of Computed Total Momentum of a Bent Sphere Cone

Computations show that for a scattered network, the precision is lower (e.g., J_o=11, the max(Δ M) of the bent sphere cone is about 1 percent, the tapered cone is about 0.5 percent); the precision gradually rises as the network becomes denser and when J_o=31 the bent sphere cone is 0.1 percent and the tapered cone is about 0.3 percent.

As shown in figures 8 and 9, the larger errors occur in the initial section and extreme left end of the "tapered surface". This is due to the use of the interpolation formula in these sections which causes larger truncation errors.

To sum up, this method can attain relatively high precision under total mass, total energy and total momentum conservation.

References

[1] J.M. Solomon. "A Program for Computing Steady Inviscid Three-Dimensional Supersonic Flow on Re-entry Vehicles" (Vol. I-I. 1977) AD-A044544.

[2] C.L. Kynss and T.B. Harris "A Three-Dimensional Flow Field Computer Program for Maneuvering and Ballistic Re-entry Vehicle" Report No AD-A 063355 (Vol.3) 1979.

[3] Li Songbo et.al. "Stabilization Method For Computing Flow Fields Around a Blunt Nose Body", 1979.2. Acta Aeronautica Ft Astronautica Sinica.

[4] А. Н. Любимов. В. В. Русанов. "Течения Газа Около Тупых Тел" (Часть I) 1970.

[5] Zhu Youlan et.al., "A Numerical Computation Method for the Initial Boundary Value Problem of a Set of Hyperbolic Equations and Its Application", 1977.3 Journal of Applied Mathematics.

[6] "Pressure Measurements on Four Cone-Cylinder-Flare Configurations at Supersonic Speeds" Report No RD-TM-69-11. 1969. 10.AD 699539.

EXPERIMENTAL STUDY ON HEAT TRANSFER TO ROUGH WALLS

by Tian Wenbing, Li Xue and Mao Mingfang
(Beijing Institute of Aerodynamics

Abstract

Experimental results of heat transfer to rough walls are given in this paper for sphere cone models at Mach number 5. The nose radius of the models is 27.4 mm and its base diameter is 60 mm. Five models have been tested and the different roughness in its bend diameters are separately 0,0.3,0.5,0.7 and 0.9 mm. The tests were conducted in a conventional hypersonic wind tunnel at total pressures p_t of 10-45 kg/cm^2 and Reynold's numbers Re$_D$ of (0.8-3.6) $\times 10^6$.

The test results indicate that the smooth wall model heating is the laminar flow heating, its heat flux stagnation point is quite close to the laminar flow theoretical data, and the influence of roughness at low total pressure (10kg/cm^2) occurs mainly to promote the transition and development of a boundary layer. With the increasing total pressure in the wind tunnel the static pressure on model and local Reynolds numbers correspondingly increase. In this case, the effect of roughness on heat transfer becomes remarkable and the most remarkable region appears at the sonic point region on the nose. At the highest total pressure (p_t=45 kg/cm^2) and with the largest roughness (d=0.9 mm), the ratio of rough wall heat flux to laminar flow smooth one (q_i/q_{s0}) could be up to 4 except at stagnation point where it could approach 6. Its raise seems to be related to the local shape change in the vicinity of the stagnation point.

I. Preface

The problem of roughness and equivalent roughness was already studied during the 1930's [1]. Recently, following the extended use of the warhead ablation plan, this has been given greater attention. During the re-entry process, the sonic point region on the nose becomes very rough. For example, the average height of these small protrusions is several times and up to over ten times the ideal thickness of the laminar flow boundary layer. At this time, the roughness not only influences the transitions of the boundary layer but also influences the velocity and temperature section structure of the entire boundary region. Further, this can also cause the heat flow on the surface to increase greatly and there can be a several fold disparity with the classic computation results.

Since the 1970's, although much experimental research has been done abroad [2,3,4], yet because the problems are so complex or because the experiments themselves are difficult, up to the present the inherent influences and mechanisms are still not totally clear. Because of this, we measured several types of bead rough wall model heat flows with a small scale hypersonic wind tunnel to compare and also measure the heat flow value of the smooth wall model.

Because the increasing effects of roughness on heat flow are closely related to the given Reynolds regions as well as the geometric shape of the model, we selected typical sphere cone shapes. Five models were used and the rough bead diameters on the surfaces of the models were 0,0.3,0.5,0.7 and 0.9mm, the Mach number is 5, the wind tunnel total pressure p_t was 10-45 kg/cm^2, and the corresponding Reynolds numbers Re_D were (0.8-3.6) $x10^6$. For convenience of analysis, we also gave the laminar flow around smooth wall sphere cones under similar conditions, and the theoretical computation values of the turbulent heat flow.

II. Symbols

c	material's specific heat (kilocalories/kg^{o}C)
d	rough bead diameter (mm)
D	model's base diameter (mm)
K	equivalent height of roughness (mm)
p	pressure (kg/cm^2)
q	heat flow (kilocalories/meter^{2}seconds)
R	radius of nose (mm)
Re_∞	Reynolds numbers $\rho_\infty u_\infty D/\mu_\infty$
Re_s	local Reynolds numbers on surface of model $\rho_e u_e s/\mu_e$
s	distance along surface beginning from stagnation point (mm)
T	Temperature (K)
t	time (seconds)
u	velocity (meters/second)
ρ	air flow or material density (kg/meter^2)
δ	thickness of model wall or boundary layer (mm)
θ	included angle between surface's normal line and model's symmetrical axis (degrees)
μ	granularity coefficient (kg·seconds/meter^2)
ϕ	meridian angle (degrees)

Lower Symbols

e	outer boundary value of boundary layer
i	different measuring point values
s_o	stagnation point value of smooth wall
t	flow stagnation conditions
∞	flow conditions

III. Test Conditions

1. Wind Tunnel

This experiment was carried out in a second order firing

free efflux type conventional hypersonic wind tunnel. In order to have a sufficient Reynolds number variation range, we selected relatively low experiment Mach numbers. The concrete experiment conditions for Mach number 5 are as follows:

(1) p_t 公斤/厘米^2	10	20	30	45
$Re_D \times 10^{-6}$	0.8	1.6	2.4	3.6
T_t K	473			

Key: 1 p_t kg/cm^2

Following the increases of the total pressure, the Mach number decreased slightly. This can be disregarded in the experiment.

2. Experiment Model

The nose radius R of the sphere cone selected for the experiment is 27.4 mm, the base diameter D is 60 mm and to make it convenient to connect with the tail strut, the model's base was extended to the cylinder section (for details see fig. 1).

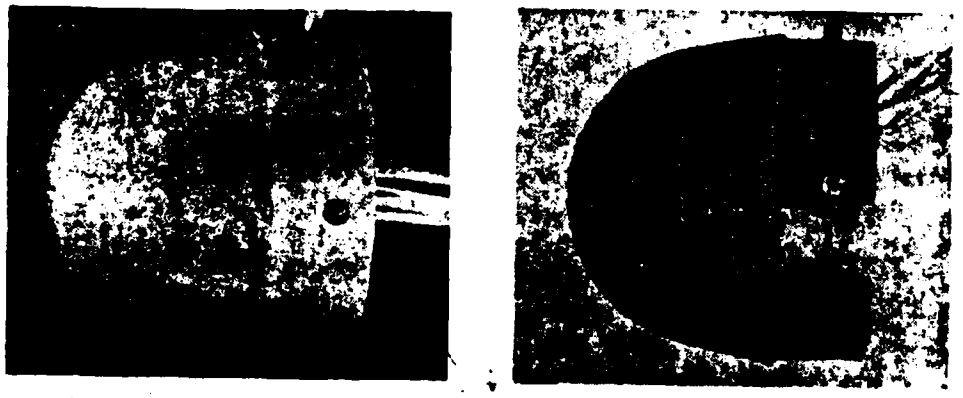

(a) 光滑壁模型 Smooth wall model

(b) 粗糙壁模型 d=0.9毫米 Rough wall model d=0.9mm

Fig. 1 Photographs of Partial Models

The models used common heat transfer to test the thin wall structure. The models are electroformed: on the preprocessed plastic (polystyrene) sphere cone model and on uniform glue the small plastic spheres go through a sieve with different diameters. After electroplating forms a red copper matrix there is nickel-plating to corrode the copper film. This base machining attains a rough heat transfer model with a surface which has small spheres with different diameters. The small spheres are stuck closely and firmly together and do not allow piling up. The glue cannot be too thick so as to avoid having gaps blocking up the small spheres. Therefore, formation is relatively difficult. There are five types of formed models; the d=0 smooth wall model and the d=0.3,0.5,0.7 and 0.9mm rough wall models. The d values given here are approximate values. The thermocouple is welded on the inner surface and a spot welder is used on the two meridian surfaces of $\phi = 0^{\circ}$ and 180°. Altogether ten 0.2 mm diameter nickel chromium-nickel aluminum thermocouples are welded on. The nominal thicknesses of the experiment models is 1 mm and they are limited by the time of electroplating. In reality, this cannot be done, a point which will be further discussed below.

3. Experimental Process and Instruments

In order to obtain very large aerodynamic heating and relatively uniform initial temperature for the model, during the blowing process the model is first hidden in the stagnant water area outside the "excess tube" of the wind tunnel. Air is used for cooling and after the wind tunnel starts we close the cool air. At the time of the experiment, the model is released as a free falling body and because there is a relatively large disparity in inner and outer pressure during the experiment the falling velocity is very fast. The entire release throw is about 0.2 seconds and the time of passing from the jet flow boundary to the core flow is even shorter.

The temperature changes on the surface of the model are sent from the wind tunnel's examination equipment to the Chinese-built 121 computer for print out. The examination sampling speed is 200 points/second, precision is $\pm$ 0.5° and the final data processing is completed on the Chinese-built 320 computer. Flow field photography uses laser technology so that one by one conventional instruments are being phased out.

IV. Data Processing

1. Related Constants

After eliminating radial heat conduction, the heat flow computation formula for the common thin wall heat transfer model is:

$$q_i = \rho c \delta_i \frac{dT_i}{dt} \qquad (1)$$

In the formula, ρ and c are the related physical characteristic parameters of the model's material and c is the function of the wall temperature. An approximate constant quantity can be taken from our useful temperature range. Here, we take the value when the wall temperature is 20°C, ρ =8900 kg/meter^3, c=0.106 kilocalories/kg°C.

δ_i is the model's wall thickness in the thermocoupler's welding point area. Because the model has a curved surface and small spheres, even though the electrode shape makes a corresponding change, the wall thickness of the model is still not uniform. Even the smooth wall model also usually has thin stagnation points and a thicker cone surface. Furthermore, the thermocoupler's welding point is welded on the inner surface of model according to the printed marks and the welding point. After the welding points are dropped on the outer surface small spheres they also fall in the spaces of the small spheres which are difficult to know. Therefore, the δ_i which depend on direct measurement

or computation all pose difficulty. If the welding is bad, small concave hollows may appear and thus change the wall thickness. For this reason, this experiment was calibrated on *self-made* static calibration equipment with a 30 kilowatt infrared iodine tungsten lamp set. The standard for static calibration is to take a material with known thickness of similar nickel plate and a heat insulation plate is put on the model and nickel plate surface between the commonly prepared Chinese ink, test piece and lamp set. At the time of calibration, the heat insulation plate is quickly taken out and a six pen recorder is used to record the temperature change curve of the two., We can convert the δ_i。 of each welding point on the model from equation (1). See table 1 for detailed numerical values.

(1)测点序号	1	2	3	4	5	6	7	8	9	10
θ 或 (2)φ=0°	0°		20°		40°		60°			
s/R	180°		10°		30°		50°		70°	1.44	1.62

(3)序号 \ d / δ_i	0	0.3	0.5	0.7	0.9
1	0.73	1.08	0.84	0.77	0.65
2	0.60	1.06	0.82	0.80	0.70
3	0.70	0.96	0.87	0.81	0.82
4	0.85	1.11	0.88		0.76
5	0.70		0.74	0.80	0.84
6	0.70	1.10	0.70	0.94	0.78
7	0.88	0.75	0.86	0.88	1.00
8	0.96	1.10	0.81	0.98	0.80
9	0.93	0.83	1.00	0.94	1.08
10	0.93	0.78	1.03	0.86	1.00

(4)表中δ_i是多次静校平均值。单位毫米。

Table 1 Coordinates of the Measuring Points and the Wall Thickness of the Model at Those Points (Static Calibration)

Key: 1 Sequence number of measuring points

Key: 2. Or
3. Sequence number
4. In the table, δ_1 is the mean value of multiple static calibration; the unit is millimeters

2. Computation of Derivative dT_i/dt

Most often prior to the experiment the temperature changes in accordance with the time and the shape of the T-t curve is unknown. Moreover, the curves differ in accordance with the differences of the experimental conditions, model shape and positions of the measuring points of each wind blow. For example, in this experiment, the temperature in the vicinity of the smooth wall sphere cone's stagnation points rises very quickly and for the most part there are conic and cubic curve changes of time t. Yet on the cone's surface, the temperature gradually rises linearly. It is very difficult to find a general equation nor is it rational.

In consideration of the above special points, we selected a multiple regression analysis method commonly used in mathematical statistics. In principle, it can automatically select appropriate curve equations for each measuring point from the elementary function. Moreover, the mean square deviation of these curves is minimal. This is different from the method found in reference [3] and naturally the method is overelaborate. This is not difficult to resolve due to checking and the application of computers.

During the experimental process, before the model is inserted into the air flow the wall temperature is uniform and after the wind tunnel starts there are not very large fluctuations. After being inserted, because the sequence of each measuring point of the model making contact with the air flow

differ the times the wall temperature departs from the initial line are different. Furthermore, some of the heat flows of each measuring points are large and some small and some seem to be invisible. These pose certain difficulties for the automatic processing of the data and so require proper formulations. To analyze the actual circumstances of this experiment and make an integrated comparison we selected each wind blow to be more or less close to (or an average of) the initial temperature of $25^{\circ}C$, usually a little higher than room temperature. Afterwards, the last measuring point regression curve sticks in or out to the corresponding found time t of the wall's temperature and is fixed as the effective time of the wall temperature beginning to depart from the initial line. The corresponding dT_i/dt is the desired derivative value. The data points in the unstable process where the T-t curve's initial section heat flow is too low are set aside beforehand. Naturally, they can also be rejected in a certain order or corrected afterwards.

There is a strong relationship between the results of regression analysis and the selection of the elementary function. It is often necessary to seek help from professional knowledge and here we selected a quintic multi-item formula of time t. The T-t curve regression analysis mean square deviation of the experimental point is about $\pm 0.5^{\circ}$. Yet this is only preliminary and still awaits further improvement. See reference [5,6] for the mathematical writing of this method.

V. Results of Experiment and Discussion

The results of the experiment, that is the different roughnesses, are given separately in figs. 2-6. Due to the limit of space, the data table cannot be given again and we will only quote from it when necessary. The data in the figures are the regression computation results of 10 experimental points obtained

in one second. For convenience of analysis and comparison, besides independently giving the smooth walls stagnation point heat flows, for the rest we gave the specific heat flow (q_i/q_{so}) forms equivalent to the smooth wall's stagnation point experimental values.

1. Heat Flow of Smooth Wall

From the form given by the data, the selection of q_{so} itself is worthy of attention. Here we use the mean value of the cubic repeatability experiment which is relatively close to the theoretical computation results for the laminar flow stationary points given by J.A. Fay and F.R. Riddell [7]:

p_t(公斤/厘米) (1)		10	20	30	45
(2) q_{so} (大卡/米²秒)	实验值 (3)	20.82	29.58	33.43	36.91
	理论值 (4)	19.16	27.09	33.18	40.63

Key: 1. p_t (kg/cm)
2. (Kilocalories/meter^2 seconds)
3. Experimental value
4. Theoretical value

For convenience of analysis, we used L. Lees ' method [7] and the reference enthalpy method [7,9] to make corresponding computations of the partial laminar flow of the sphere cone models and the turbulent flow and heat flow distribution. The computation results are separately indicated with broken lines in figures 2-6.

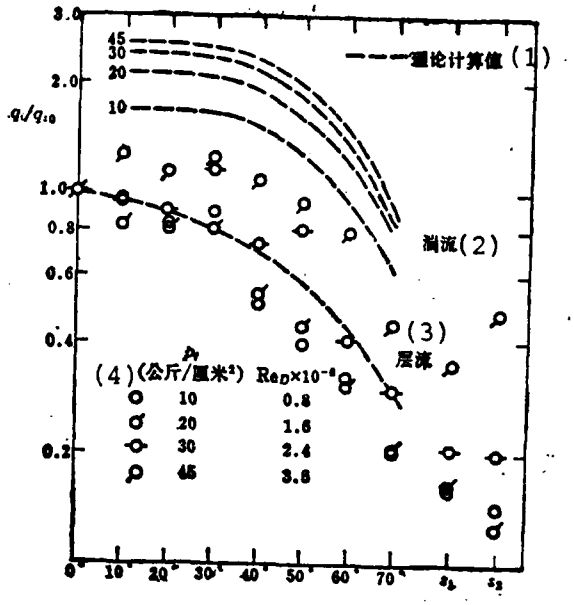

Fig. 2 Heat Flux Distribution Along Surface for Smooth Wall Model With d=0

Key: 1. Theoretical computation values
2. Turbulent flow
3. Laminar flow
4. (Kg/cm^2)

Fig. 2 is a comparison of the experiment and theoretical conditions of the distribution of the smooth wall's (d=0) heat flow. In the figure, the experimental points indicate the results of each experiment (usually we took the results of the first experiment). It can be seen from the figure that the distribution of a part of the nose's heat flow is similar to the computation values of the laminar flow. It rises with the enlarging of the wind tunnel's total pressure p_t, that is the enlarging of the Re_D, yet, in general, it is still in a laminar

flow state. This is also very close to the analysis of the model surface's partial Reynolds number Re_r computation results. When p_t=45 kg./cm^2, in the θ=50°, 70° area Re_r is separately 5.8x10^5 and 6.37x10^5. It can be said that in most situations it is in a transition boundary state. There is possible transition on the sphere cone surface and when in the cone surface's two measuring points (measuring points numbers 9 and 10) of the T-t curve, a double slope situation appears. Theoretical computations could not be made because there were too few measuring points.

2. The Influence of a Rough Wall on the Heat Flow

To analyze the influence of roughness by simply referring to the heights of the rough beads is not sufficient. It is also related to the distribution densities and configurations of the beads. Usually, the concept of equivalent roughness is used but the influence mechanism is not clear and it is also difficult to have a unified method. Here we used the experimental results of reference [1] on the equivalent bead roughness with the aim that it approximately comprehends the equivalent measure. We also take the ideal smooth wall laminar flow boundary layer thickness δ as the reference quantity. When p_t=10 kg/cm^2, the computation results are as follows:

d (毫米) (1)	K(毫米) (2)	$K/\delta_{\theta=6°}$	$K/\delta_{\theta=70°}$
0.3	0.19	2.64	0.67
0.5	0.31	4.40	1.12
0.7	0.44	6.16	1.56
0.9	0.56	7.92	2.01

(3)表中 $\delta_{\theta=6°}$ =0.071毫米, $\delta_{\theta=70°}$ =0.28 毫米。

Key: 1. (mm)
2. (mm)
3. In the table, δ_θ =5°=0.071 mm,
δ_θ =70°=0.28 mm

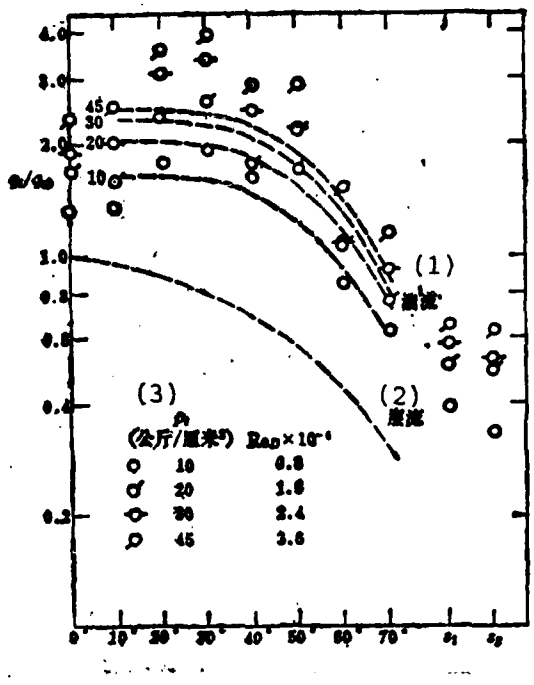

Fig. 3 Heat Flux Distribution Along Surface For Rough Wall Model With d=0.3 mm

Key: 1. Turbulent flow
2. Laminar flow
3. (kg/cm^2)

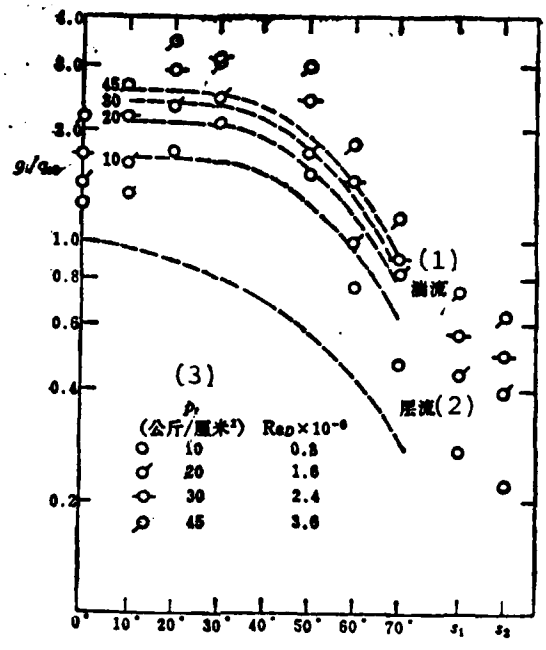

Fig. 4 Heat Flux Distribution Along Surface For Rough Wall Model With d=0.5 mm

Key: 1. Turbulent flow
2. Laminar flow
3. (kg/cm^2)

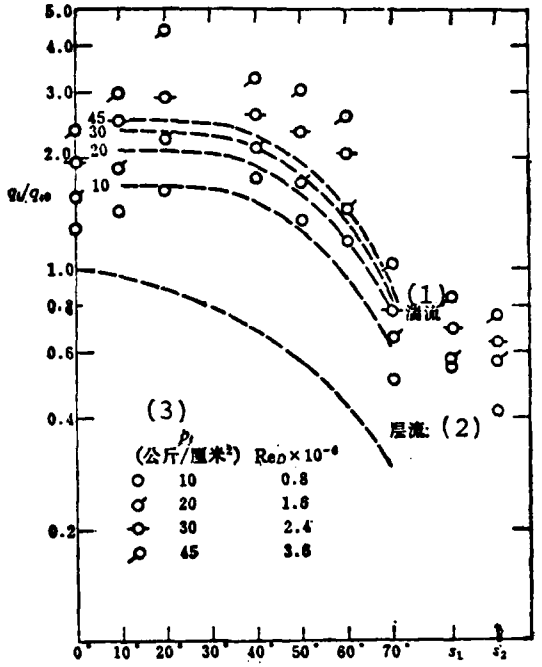

Fig. 5 Heat Flux Distribution Along Surface For Rough Wall Model With d=0.7 mm

Key: 1. Turbulent flow
2. Laminar flow
3. (kg/cm^2)

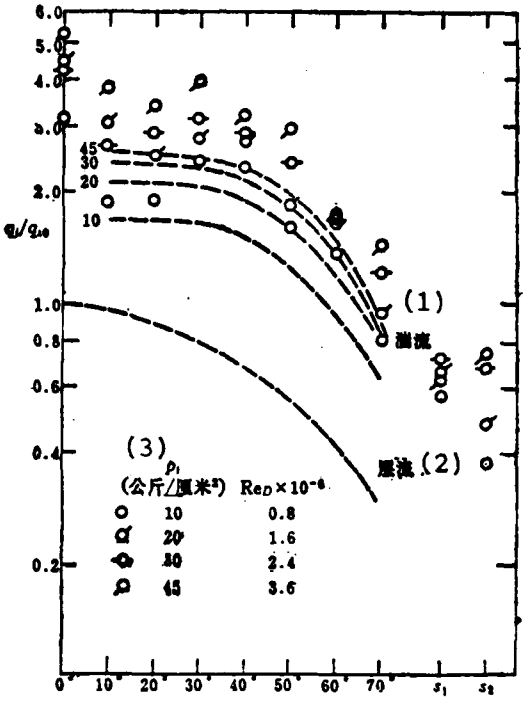

Fig. 6 Heat Flux Distribution Along Surface For Rough Wall Model With d=0.9 mm

Key: 1. Turbulent flow
2. Laminar flow
3. (kg/cm^2)

In figures 3-6, in order for experimental points with the same roughness and different total pressure to be put on a figure, we used logarithmic coordinates. Thus, when looking at the figures one must keep this in mind.

It is not difficult to see from the figures that under all of the experimental conditions the obvious transition and development was the turbulent flow. After $\theta = 20^{\circ}$, all basically

surpassed their respective turbulent flow theoretical values (as shown in broken lines) and there was a very large increase of the cone surface's heat flow as compared to the results for the smooth wall.

Under the same roughness conditions, the experimental points under low total pressure were very close to the turbulent flows theoretical broken line. For example, when d=0.3,0.5 and 0.7 mm, the results of p_t=10 kg/cm^2 were all like this and when d~0.9 mm, aside from the stagnation points, they were also basically this same way. Following the enlarging of P_t and Re_δ the effects of the enlargement of roughness on the heat flow was even more obvious. If d=0.3 mm, when total pressure p_t=10,20,30,45 kg/cm^2, the peak values of q_i/q_{so} were 2.09,2.41,3.09 and 3.44. The range of increase was quite large.

Under different roughness conditions and similar total pressure, following the enlarging of the roughness of the small sphere diameter d, the heat flow value had only a slight increase or small variation. This shows that the roughness of the small sphere diameter is sufficiently large. At the same time, it also shows that even under relatively large roughness, because the total pressure is low, the roughness only affects boundary layer transition. Yet, under high total pressure, this type of heat flow variation is not large and it possibly signifies that the influence of roughness on heat flow increases carries certain limitations.

The rough wall heat flow distribution along the surface is generally lower at the two ends and the peak value heat flow is in the vicinity of the sonic point region. Taking the d=0.9 mm model as an example, aside from the stagnation point the peak value heat flow q_i/q_{so} in the vicinity of the sonic point region approaches 4, and when the conditions of the stagnation point

differ from other models including low pressure data, the heat flow clearly increases. When the maximum total pressure is p_t=45 kg/cm^2, q_i/q_{so} approach 6 and it seems that this is possibly related to the stagnation point's local configuration changes.

Furthermore, it can also be seen from figures 3-5 that there appears to exist a transition region with less than ideal turbulent flow heating between the stagnation point and θ =20° measuring point. Whether or not this signifies the existence of a laminar flow region, the influence of the roughness of this region on heating is not critical.

The influence of roughness on the heat flow being this large is worthy of attention and naturally the problems are quite complex. Below we will summarize and simply discuss the existing test results.

We can see from the data fluctuations that p_t is a parameter worthy of attention and seems to cause an "enlarging" effect. The changes of p_t are also affected by surface static pressure p_e and local Reynolds number Re_x.

Under low pressure conditions, the roughness acts as the laminar flow boundary layer's unstable factor and this type of unstable small disturbance strengthens with the increase of roughness. After the roughness is sufficiently large, transition appears under relatively low Res conditions and a turbulent flow boundary layer develops and forms just as is seen in the p_t=10 kg/cm^2 data situation. The artificial transition rough area method commonly used in wind tunnel experiments is based on analagous principles.

Following the enlarging of wind tunnel total pressure p_t

there is also a corresponding enlargement of model wall surface static pressure p_e. The small disturbance caused by the roughness seems to strengthen and this causes the temperature distribution inside the entire surface boundary region to be even more uniform. This in turn causes an enlargement of the temperature gradient in the vicinity of the surface which can result in a manifold increase of the rough wall heat flow. It appears that a more rational equivalent roughness concept is that the surface's static pressure p_e (or p_t) should be a variable worthy of attention.

The influences of Re_θ are easily understood. Following the enlargement of p_t, Re_θ has a corresponding enlargement and the thickness of the boundary layer then decreases. Here, we will again use the results of the laminar flow of a smooth wall. When p_t=45 kg/cm^2, $\delta_{\theta-\theta^*} = 0.033$ mm and thus the corresponding K/δ_θ has a manifold increase and in essence enlarges the corresponding roughness. Summarizing these two aspects it is not difficult to conceive that the region of the critical influence of roughness on heat flow is on the end of the nose.

Fig. 7 Laser Schlieren Photograph d=0.9 mm, p_t=20kg/cm^2

Looking at the photograph in fig. 7 of the related flow field of the rough wall model can help us further discuss the problem.

It can be seen from the photograph that there is an obvious oblique shock waves group in the vicinity of the sonic point region. (θ =30°-40°). Their strength increases with the enlargement of the total pressure and roughness. After there is sufficiently large roughness and waves, the rise of static pressure p_e often produces complex shock wave boundary layer disturbance and separated reattached flow because of this. It seems that this phenomenon is a very important factor contributing towards the many fold increase of this region's heat flow. In the subsonic area in front of the sonic point, the roughness influence shown

in the experiment was not an important fact but seemed to be very good collateral evidence for the crux of the problem. The transition under low pressure conditions mentioned above also appears to be related to the separated vortex group transition which again proves the influence of roughness on heating and the configuration. Naturally, this discussion is very preliminary and awaits further detailed experiments.

References

[1] Herman Schlichting "Boundary layer theory" pp 519-531 1955.

[2] R.L. Varwing "Effect of roughness on heating at the forward surface of a sphere at Mach 5" AD 708471.

[3] R.E. Phinney, F.P. Baltakis "Influence of roughness on heat transfer and transition" NOL TR=73-231 (AD77384).

[4] C.L. Jaeck "Analysis of pressure and heat transfer test on surface roughness elements with laminar and turbulent boundary layers" NASA CR-537.

[5] "The Regression Analysis Method," Statistics Group of the Mathematics Institute of the Academia Sinica.

[6] Ye Wenhu et.al.,"Fitting Problems of Experimental Curves," Beijing BG-515, 1977.

[7] Lu Hanjiang, "Theory of Attached Surface Layer Natural Defense Industrial Publications.

[8] H.G.Timmer "Aero thermodynamic characteristics of slender ablating re-entry vehicles". AIAAPaper 70-826.

[9] Pan Meilin, MBG6-124, Beijing Institute of Aerodynamics, 1968.1.

A GENERALIZED J-INTEGRAL OF *TWO DIMENSIONS*

by Zhang Xing and Wu Guoxun
(Beijing Institute of Aeronautics and Astronautics)

Abstract

Beginning from the energy release rate, this paper derived the generalized J-integral for support of surface forces and body forces of plates with variable thickness in non-uniform temperature fields. It also proved the conservation properties of the generalized J-integral.

I. Preface

We know that J.R. Rice proposed the J-integral for plates with equal thickness under non-body force and equal temperature conditions [1] and that the J-integral was later extended and applied widely in engineering. Very recently, there have been articles which have considered the influences of body force and temperature [2,4].

Yet, like the importance of a turbine disk in an aircraft engine, it not only supports surface forces and body forces but the plate itself is a plate with variable thicknesses in a non-uniform temperature field.

Beginning from the energy release rate, this paper derives the generalized J-integral for the support of surface forces and body forces of plates with variable thicknesses in non-uniform temperature fields. It also proved the conservation property of the generalized J-integral.

Due to the limit of space, the relationship of generalized J-integral and crack tip singularity will be discussed in another article.

We have seen the results of reference [2] from other writers [3] but did not see the original article.

II. Energy Expressions of Physical Equations

1. Linear Elasticity

Based on elastic mechanics, we considered that the temperature effect of the elastic stress and strain relation possesses the following form:

$$\sigma_{ij}=2\mu e_{ij}+\delta_{ij}\lambda\delta_{kl}e_{kl}-\delta_{ij}k3\alpha T \qquad (1)$$

In the above formula, σ_{ij} is the stress component, ε_{ij} is the strain component, λ and μ are Lamé constants, k is the volume's elastic constant, T is the temperature, α is the linear expansion coefficient, and δ_{ij} is the Kronecker Delta.

The unit volume of deformation potential energy W is equivalent to [5]

$$W=\int_0^M \sigma_{ij}de_{ij}+\frac{k}{2}(3\alpha T)^2 \qquad (2)$$

When formula (1) is substituted into formula (2), after integration we can obtain

$$W=\mu e_{ij}e_{ij}+\frac{\lambda}{2}\delta_{ij}e_{ij}\delta_{kl}e_{kl}-k\,3\alpha T\delta_{ij}e_{ij}+\frac{k}{2}(3\alpha T)^2 \qquad (3)$$

Based on formulas (1) and (3), we can prove that:

$$\frac{\partial W}{\partial e_{ij}} = \sigma_{ij} \qquad (4)$$

At the same time

$$\frac{\partial W}{\partial T} = -3ka\delta_{ij}e_{ij} + 9ka^2T \qquad (5)$$

2. Elasto-Plastic Conditions

Taking σ and ε to separately represent the mean stress and the mean strain, the stress spherical quantity and stress partial quantity are

$$\sigma'_{ij} = \delta_{ij}\sigma, \qquad \sigma''_{ij} = \sigma_{ij} - \delta_{ij}\sigma \qquad (6)$$

and the strain spherical quantity and strain partial quantity are

$$\varepsilon'_{ij} = \delta_{ij}\varepsilon, \qquad \varepsilon''_{ij} = \varepsilon_{ij} - \delta_{ij}\varepsilon \qquad (7)$$

Based on Илюшин's total quantity theory [6], we can know that:

$$\left.\begin{aligned} \sigma'_{ij} &= 3k(\varepsilon'_{ij} - \delta_{ij}\alpha T) \\ \sigma''_{ij} &= \frac{2}{3}\frac{\sigma_s}{\varepsilon_s}\varepsilon''_{ij} \end{aligned}\right\} \qquad (8)$$

In the above formula, σ_s and ε_s are separately the equivalent stress and equivalent strain. They are equal to

$$\sigma_s = \sqrt{\frac{3}{2}\sigma''_{ij}\sigma''_{ij}} \qquad (9)$$

$$\varepsilon_s = \sqrt{\frac{2}{3}\varepsilon''_{ij}\varepsilon''_{ij}} \qquad (10)$$

The deformation potential energy of the unit volume is still equal to

$$W=\int_0^M \sigma_{ij}de_{ij}+\frac{k}{2}(3\alpha T)^2=\int_0^M(\sigma'_{ij}+\sigma''_{ij})(de'_{ij}+de''_{ij})+\frac{k}{2}(3\alpha T)^2 \quad (11)$$

When we substitute formula (8) into formula (11) and take into consideration formulas (9) and (10), we can obtain:

$$W=\int_0^M \sigma_e de_e+\frac{k}{2}\delta_{ij}e_{ij}\delta_{kl}\varepsilon_{kl}-k\,3\alpha T\delta_{ij}e_{ij}+\frac{k}{2}(3\alpha T)^2 \quad (12)$$

We can know from formulas (8) and (12) that:

$$\frac{\partial W}{\partial \varepsilon_{rs}}=\sigma_{rs} \quad (13)$$

At the same time

$$\frac{\partial W}{\partial T}=-3k\alpha\delta_{ij}e_{ij}+9k\alpha^2T \quad (14)$$

III. The Generalized J-Integral and Energy Release Rate

We know that the system's total potential energy Π is equal to

$$\Pi=\int_A W\,dA-\int_{C_s}S_iu_i\,ds-\int_A B_iu_i\,dA \quad (15)$$

In the above formula, S_i is the surface force, B_i is the body force, u_i is the displacement, A is the area of the plate and C_s is the boundary of the force (fig. 1).

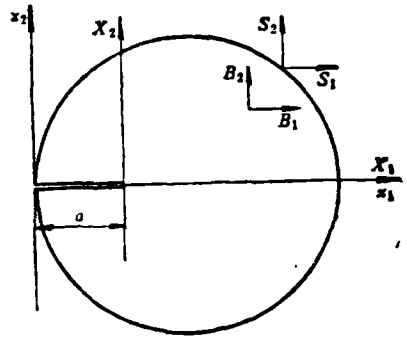

Fig. 1 Generalized J-Integral and Energy Release Rate

Thus, energy release rate G is equal to

$$G = -\frac{1}{t_a}\frac{d\Pi}{da} = \frac{1}{t_a}\left\{\int_{C_a} S_i \frac{du_i}{da}\, t ds + \int_A B_i \frac{du_i}{da}\, t dA - \int_A \frac{dW}{da} t dA\right\} \quad (16)$$

In the above formula, t_a is the plate thickness in the crack tip area.

On given displacement boundary C_u, there is no relation between displacements u_i and a. Thus $\frac{du_i}{da} = 0$, therefore at C_u

$$\int_{C_a} S_i \frac{du_i}{da}\, t ds = 0 \quad (17)$$

Taking the above formula into consideration, we can rewrite formula (16) as follows:

$$G = \frac{1}{t_e}\left\{\int_C S_i \frac{du_i}{da}\, t ds + \int_A B_i \frac{du_i}{da}\, t dA - \int_A \frac{dW}{da}\, t dA\right\} \qquad (18)$$

In the above formula, C is the entire boundary of the plate.

We introduce a flow coordinate system (X_1, X_2) which takes the crack tip as the point of origin and the crack's extended line as the horizontal coordinate. It has the following relationship (fig. 1) with the original fixed coordinate system (x_1, x_2):

$$X_1 = x_1 - a, \qquad X_2 = x_2 \qquad (19)$$

When compared to a fixed point, x_2 remain unchanged. When a has changes, X_1 likewise changes. Thus, the change of any physical quantity P is:

$$dP = \frac{\partial P}{\partial a} da + \frac{\partial P}{\partial X_1} dX_1 \qquad (20)$$

At the same time, we can know from formula (19) that:

$$dX_1 = -da \qquad (21)$$

Thus

$$\frac{dP}{da}=\frac{\partial P}{\partial a}-\frac{\partial P}{\partial X_1} \tag{22}$$

It should be pointed out that in the above formula,

$$\frac{dP}{da}=\frac{\partial P}{\partial a}\Big|_{x_1,x_2} \quad \frac{\partial P}{\partial a}=\frac{\partial P}{\partial a}\Big|_{X_1,X_2}$$
$$\frac{\partial P}{\partial X_1}=\frac{\partial P}{\partial X_1}\Big|_{a,X_2}$$

Based on the law of composite function partial derivation,

$$\frac{\partial P}{\partial X_1}=\frac{\partial P}{\partial x_1}\frac{\partial x_1}{\partial X_1}+\frac{\partial P}{\partial x_2}\frac{\partial x_2}{\partial X_1}=\frac{\partial P}{\partial x_1}\frac{\partial x_1}{\partial X_1}=\frac{\partial P}{\partial x_1} \tag{23}$$

If formula (23) is substituted into formula (22), we have:

$$\frac{dP}{da}=\frac{\partial P}{\partial a}-\frac{\partial P}{\partial x_1} \tag{24}$$

Taking formula (24) into account, we can know that:

$$\int_C S_i\frac{du_i}{da}\,tds=\int_A S_i\frac{\partial u_i}{\partial a}\,tds-\int_A S_i\frac{\partial u_i}{\partial x_1}\,tds \tag{25}$$
$$\int_A B_i\frac{du_i}{da}\,tdA=\int_A B_i\frac{\partial u_i}{\partial a}\,tdA-\int_A B_i\frac{\partial u_i}{\partial x_1}\,tdA \tag{26}$$
$$\int_A \frac{dW}{dA}\,tdA=\int_A \frac{\partial W}{\partial a}\,tdA-\int_A \frac{\partial W}{\partial x_1}\,tdA \tag{27}$$

Based on the law of composite function partial derivation, the above formulas can be rewritten as follows:

$$\int_A \frac{dW}{da} t\,dA = \int_A \frac{\partial W}{\partial \varepsilon_{ij}} \frac{\partial \varepsilon_{ij}}{\partial a} t\,dA + \int_A \frac{\partial W}{\partial T} \frac{\partial T}{\partial a} t\,dA - \int_A \frac{\partial W}{\partial x_1} t\,dA \qquad (28)$$

Because T is not the function of a, based on formula (24) we can know that:

$$\frac{dT}{da} = \frac{\partial T}{\partial a} - \frac{\partial T}{\partial x_1} = 0\,, \quad \frac{\partial T}{\partial a} = \frac{\partial T}{\partial x_1} \qquad (29)$$

If formula (29) is substituted into formula (28), we have:

$$\int_A \frac{dW}{da} t\,dA = \int_A \frac{\partial W}{\partial \varepsilon_{ij}} \frac{\partial \varepsilon_{ij}}{\partial a} t\,dA + \int_A \frac{\partial W}{\partial T} \frac{\partial T}{\partial x_1} t\,dA - \int_A \frac{\partial W}{\partial x_1} t\,dA \qquad (30)$$

Taking this a step further, based on the partial integral formula and surface integral — linear integral transformation formula, we can know that:

$$\int_A \frac{\partial W}{\partial x_1} t\,dA = \int_A \frac{\partial W t}{\partial x_1} dA - \int_A W \frac{\partial t}{\partial x_1} dA = \int_C W t\,dx_2 - \int_A W \frac{\partial t}{\partial x_1} dA \qquad (31)$$

Taking into consideration formula (31), formula (30) can be rewritten as follows:

$$\int_A \frac{dW}{da} t dA = \int_A \frac{\partial W}{\partial e_{ij}} \frac{\partial e_{ij}}{\partial a} t dA - \int_C W t dx_2 + \int_A W \frac{\partial t}{\partial x_1} dA + \int_A \frac{\partial W}{\partial T} \frac{\partial T}{\partial x_1} t dA \quad (32)$$

Based on the principle of virtual work, we have

$$\int_C S_i \frac{\partial u_i}{\partial a} t ds + \int_A B_i \frac{\partial u_i}{\partial a} t dA = \int_A \sigma_{ij} \frac{\partial \varepsilon_{ij}}{\partial a} t dA \quad (33)$$

Furthermore, based on physical equation (4) or (13), we can know that:

$$\sigma_{ij} = \frac{\partial W}{\partial e_{ij}} \quad (34)$$

Thus

$$\int_C S_i \frac{\partial u_i}{\partial a} t ds + \int_A B_i \frac{\partial u_i}{\partial a} t dA = \int_A \frac{\partial W}{\partial e_{ij}} \frac{\partial e_{ij}}{\partial a} t dA \quad (35)$$

If formulas (25), (26) and (32) are substituted into formula (18) and we take into consideration formula (35), we have:

$$G=\frac{1}{t_0}\left\{\int_C W t\,dx_2-\int_A W\frac{\partial t}{\partial x_1}\,dA-\int_A\frac{\partial W}{\partial T}\frac{\partial T}{\partial x_1}t\,dA\right.$$
$$\left.-\int_C S_i\frac{\partial u_i}{\partial x_1}t\,ds-\int_A B_i\frac{\partial u_i}{\partial x_1}t\,dA\right\} \qquad (36)$$

The right side of the equal sign is the generalized J-integral when the path of integration is the boundary of the plate.

IV. The Definition of the Generalized J-Integral and its Path Independent Property

The Γ curve is taken as a curve which begins from the lower surface of the crack and ends on the upper surface of the crack including the crack tip. Letting Ω represent the surrounding area of the Γ curve and upper and lower surfaces of the crack (fig. 2) then the J-integral is defined as follows:

$$J=\frac{1}{t_0}\left\{\int_\Gamma W t\,dx_2-\int_\Gamma S_i\frac{\partial u_i}{\partial x_1}t\,ds-\int_\Omega B_i\frac{\partial u_i}{\partial x_1}t\,dA\right.$$
$$\left.-\int_\Omega W\frac{\partial t}{\partial x_1}\,dA-\int_\Omega\frac{\partial W}{\partial T}\frac{\partial T}{\partial x_1}t\,dA\right\} \qquad (37)$$

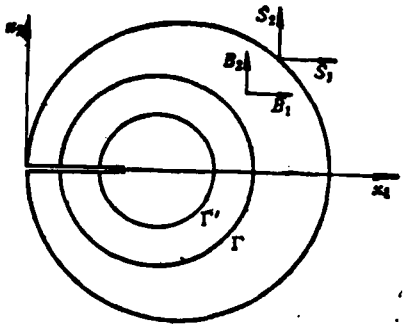

Fig. 2 Generalized J-Integral and Its Path Independent Property

Below we will prove that there is no relation between the generalized J-integral and its path. For this reason, the Γ' curve is a curve which begins from the lower surface of the crack and ends on the upper surface of the crack including the crack tip. Ω represents the surrounding area of the Γ' curve and upper and lower surfaces of the crack. We let Γ^* represent the closed curve formed from Γ, Γ' as well as the upper and lower surfaces of the crack, and Ω^* represent the surrounding area of Γ^*. When we consider that on the upper and lower surfaces of the crack

$$dx_1 = 0 \tag{38}$$

$$S_i = 0 \tag{39}$$

then based on the definition of the J-integral, we have:

$$J-J'=\frac{1}{t_0}\left\{\int_{\Gamma^0}Wtdx_2-\int_{\Gamma^0}S_i\frac{\partial u_i}{\partial x_1}tds-\int_{\Omega^0}B_i\frac{\partial u_i}{\partial x_1}tdA\right.$$
$$\left.-\int_{\Omega^0}W\frac{\partial t}{\partial x_1}dA-\int_{\Omega^0}\frac{\partial W}{\partial T}\frac{\partial T}{\partial x_1}tdA\right\} \tag{40}$$

Based on the linear integral—surface integral transformation formula, we have:

$$\int_{\Gamma^0}Wtdx_2=\int_{\Omega^0}\frac{\partial}{\partial x_1}(Wt)dA \tag{41}$$

Based on the law of composite function partial derivation,

$$\frac{\partial}{\partial x_1}(Wt)=t\frac{\partial W}{\partial \varepsilon_{ij}}\frac{\partial \varepsilon_{ij}}{\partial x_1}+t\frac{\partial W}{\partial T}\frac{\partial T}{\partial x_1}+W\frac{\partial t}{\partial x_1} \tag{42}$$

If formula (42) is substituted into formula (41), we can know that:

$$\int_{\Gamma^0}Wtdx_2=\int_{\Omega^0}\frac{\partial W}{\partial \varepsilon_{ij}}\frac{\partial \varepsilon_{ij}}{\partial x_1}tdA+\int_{\Omega^0}\frac{\partial W}{\partial T}\frac{\partial T}{\partial x_1}tdA+\int_{\Omega^0}W\frac{\partial t}{\partial x_1}dA \tag{43}$$

If formula (43) is substituted into formula (40), we can obtain:

$$J-J'=\frac{1}{t_0}\left\{\int_{\Omega^0}\frac{\partial W}{\partial \varepsilon_{ij}}\frac{\partial \varepsilon_{ij}}{\partial x_1}tdA-\int_{\Omega^0}B_i\frac{\partial u_i}{\partial x_1}tdA-\int_{\Gamma^0}S_i\frac{\partial u_i}{\partial x_1}tds\right\} \tag{44}$$

Based on physical equation (4) or (13), we can know that:

$$\frac{\partial W}{\partial \varepsilon_{ij}}=\sigma_{ij} \tag{45}$$

Further, based on the principle of virtual work, we have:

$$\int_{\Omega^*}\sigma_{ij}\frac{\partial \varepsilon_{ij}}{\partial x_1}tdA=\int_{\Omega^*}B_i\frac{\partial u_i}{\partial x_1}tdA+\int_{\Gamma^*}S_i\frac{\partial u_i}{\partial x_1}tds \qquad (46)$$

If formula (45) is substituted into formula (46) and then formula (46) is substituted into formula (44), we can obtain:

$$J-J^*=0 \qquad (47)$$

If the attained surface force and body force for a plate with variable thickness is located in a non-uniform temperature field, the generalized J-integral also has no relation to the path of integration.

V. Application Examples of Generalized J-Integral

After applying the conventional finite element method to find the nodal point displacement, we can then calculate the value of the generalized J-integral. We know that under linear elastic conditions the energy release rate is equal to

$$G=\frac{1}{E}(K_{\mathrm{I}}^2+K_{\mathrm{II}}^2)\ (\text{平面应力}) \qquad (48)$$

Key: 1. Plane Stress

In the above formula, K_1 and K_{II} are the stress intensity factors. Because

$$G = J \qquad (49)$$

therefore

$$J=\frac{1}{E}(K_{\mathrm{I}}^2+K_{\mathrm{II}}^2) \qquad (50)$$

If the crack is located on the component's geometrically symmetrical line, we can use the principle of superposition to find K_I and K_{II}; when the crack is located on a non-geometrically symmetrical line, we can find the stress intensity factors under non-composite conditions.

VI. Conclusions

1) The generalized J-integral can be defined as:

$$J=\frac{1}{t_0}\left\{\int_\Gamma W t\,dx_2-\int_\Omega W\frac{\partial t}{\partial x_1}\,dA-\int_\Omega \frac{\partial W}{\partial T}\frac{\partial T}{\partial x_1}t\,dA\right.$$
$$\left.-\int_\Gamma S_i\frac{\partial u_i}{\partial x_1}t\,dA-\int_\Omega B_i\frac{\partial u_i}{\partial x_1}t\,dA\right\}$$

2) According to the above definition, the J-integral has the property of path-independence.

3) Based on the above property, the J-integral is equal to the energy release rate of the system.

4) In consideration of the above property, we can calculate the stress intensity factors after the nodal point displacements have been obtained by the finite element method in linear elastic fracture mechanics.

5) In elasto-plastic fracture mechanics, we obtained results similar to those of Huchinson [7], that is the stress field in the vicinity of the crack tip was determined by the generalized J-integral. Thus, the generalized J-integral can be used to establish a fracture criterion under elasto-plastic conditions. This problem was prepared according to precedent and it is discussed in another article.

References

[1] H.Liebowitz:Fracture Vol. I P.192-308 1968.

[2] Ban Tian: See references mentioned in reference [3].

[3] Gong Benbo, Tufan Minggong, Jigang Zhunfu et.al. The Cracking Strength of Rotating Spherical Plates, Collection of Essays from the Mechanics Meetings of Japan (A edition), Vol. 45, No. 396 (297u-82).

[4] W.K. Wilson and L.W. Yu: The use of J-integral in thermal stress crack problems. International Journal of Fracture Vol.15 No. 4 1979.

[5] Boley Weiner: Theory of thermal stress P.262-269 1960.

[6] А. А. Ильюшин: Пластичность P. 97~98 1948.

[7] J.W. Huchinson: Singular behaviour at the end of a tensil crack in a hardening material. J. Mech. and Phys. of Solids. Vol. 16 P.13-18 1968.

DESIGN CONSIDERATIONS ON GLASS FIBER REINFORCED PLASTIC COMPOSITE STRUCTURES

by Zhu Yiling
(Shanghai GRP Research Institute)

Abstract

When using glass fiber reinforced plastic/composite materials for structural design, it is at least necessary to take the following three points into account: designability of the material's properties; non-restriction of the structure's configuration; and the linear dispersion strength of the material.

Composite materials possess many excellent properties, yet they are not "only of one family." They must also exist and develop in competition with other materials. If they can simultaneously use two or more of the above strong points, their future is bright. The commonly known glass fiber reinforced plastic aircraft nose radar cap used the strong points of composite materials transmitting radar waves and high specific strength, and the cap has not deteriorated after 40 years. There has been vigorous research carried out in the field of composite materials, especially in the areas of varieties of raw materials and their applications. There have also been great developments in researching properties, yet proper attention has not been given to the long term accumulation of reliable design data. There are many structures which are made of composite materials most of which are still in the "replacement design" stage, that is, under conditions where the shape, load and application environment of the prototype materials is unchanged, it is necessary to make full use of the strong points of composite materials

when using composite materials to replace prototype materials when manufacturing parts.

This paper only takes into account that when designing a structure with composite materials, it is at least necessary to pay attention to the following three points: designability of the material's properties; non-restriction of the structure's shape; linear elasticity and the dispersion strength of the material.

I. Designability of Material's Properties,

The designability of a composite material's properties relates to the forming of two large categories of materials for composite materials, basic and reinforcement materials, which can be selected according to design requirements. It is necessary that the properties of both the basic and reinforcement materials be understood clearly beforehand. The selection of different reinforcement and basic materials as well as their content ratio and various layer forms can make up various composite materials with different properties. Taking the ratio of shearing elastic modulus G and longitudinal elastic modulus E as an example, if we select conventional materials, then G/E is a constant for the specially designated materials. If we select and use fibrous composite materials then G/E is a designable numerical value which gives designers an extra degree of freedom. Naturally, the various property values of the composite materials are conditioned by the selected materials.

The composite mechanism of these two large categories of materials are basically physical composites and thus the properties of composite materials can be estimated according to the properties of the component materials. This can generally be simulated by using the parallel type model and series type model as shown in fig. 1.

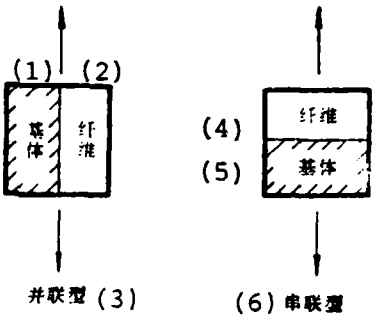

Fig. 1 Primary Models

Key: 1. Basic body
2. Fiber
3. Parallel type
4. Fiber
5. Basic body
6. Series type

For example, the elastic modulus along the fiber direction is calculated by the parallel type model:

$$E_c=E_fV_f+E_mV_f$$

In the formula, E represents the elastic modulus, V indicates the volume content, and the lower symbols c,f and m successively indicate the composite material, fiber and basic body (all of which will be similar hereafter). They are very similar to the test values and the longitudinal strength can also be estimated by analagous formulas. The elastic modulus of the vertical fiber direction can be estimated by the series type model:

$$\frac{1}{E_c}=\frac{V_f}{E_f}+\frac{V_m}{E_m}$$

This estimated value is lower than the measured data and so to more accurately reflect the real conditions we can further use the series parallel composite model [1]. Other estimations such as for heat and electric properties can also use the same type of model. This type of composite takes the properties of an independent component material as the criterion and does not consider their boundary surface influences. However, some properties focus on boundary surface effects such as fracture toughness but the above mentioned series parallel model cannot be used for simulation.

In consideration of application requirements, composite materials can be designed into three typical forms [2]:

1) Isotropic Composite Material. It can be composed of short cut fibers and also use 0°, $\pm 60^{\circ}$ or 0°, $\pm 45^{\circ}$ and 90° direction continuous fibers. There are also 3,4 and 7 direction composit materials. The strength and stiffness of this type of material is relatively low and it is suitable for use on structures with relatively large load randomness.

2) Orthogonal Balanced Composite Material. It can be composed of 0° and 90° direction continuous fibers and can also use interwoven fabric for formation. There is relatively high strength and stiffness in the two main directions (longitudinal and latitudinal directions), yet the strength and stiffness of the 45° angle it forms with the main direction is relatively weak. It is suitable for structures with strength and stiffness requirements in the two vertical directions, for example the plate and shell. We can still use this type of composite material for plates (shells) with different frame and rib distances yet its main direction is not suitable to be parallel with the frame and rib but should form a 45° with it. In this way, when in a large degree of deflection it is even more advantageous to bringing

out the strength properties of the fibers. It also has a strong shearing strength in the plate (shell) surface. China's design of a wooden bed frame strung with crisscross coir ropes is a good example of the use of fibers.

3) Unidirectional Composite Material. This is a type of composite material wherein the entire fiber is placed in the same direction. There is especially high strength and stiffness in the fiber direction yet it is weakest in the vertical fiber direction. We can only use this type of composite material when the load conditions are very clear, for example for cable. In most calculations beams and columns have simple direction stress analysis. This is because the second direction strength of isotropic materials is not sufficiently large and thus it is not necessary to calculate the stress of the second direction. Taking a square tube sectional beam of a wall with equal thickness as an example, we take unit beam length ds as the detached body (as shown in fig. 2), the bearing moment of bending on the section is M, bearing pressure stress σ_1 is on the upper surface plate, and the bearing pressure stress σ_1 is on the lower surface plate. Because the beam's bend and the bearing pressure on the upper surface plate are not on one straight line, the pulling force on the lower surface plate is also on different lines.

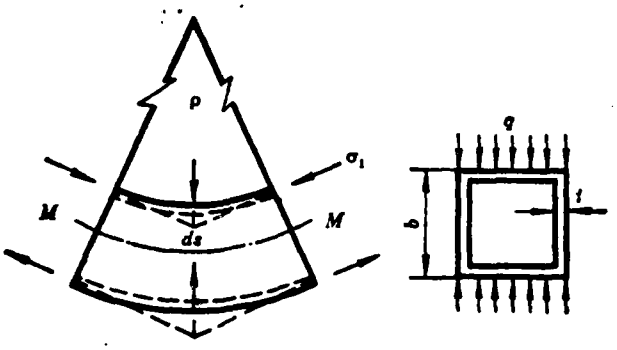

Fig. 2 Square Tube Subjected to Bending

They form the pressure of a pair of opposite pressurized tubes. Their degree of accumulation q is:

$$q=\frac{2\sigma_1 t}{ds}\left(\frac{ds}{2\rho}\right)=\frac{\sigma_1 t}{\rho}=\frac{M_1}{E_1 J_1}\sigma_1 t=\frac{(\sigma_1 J_1)/(b/2)}{E_1 J_1}\cdot\sigma_1 t=\frac{2\sigma_1^2}{E_1}\left(\frac{t}{b}\right)$$

The largest bend M_2 in the square tube section is obtained by using any structural mechanics method

$$M=\frac{1}{16}qb^2$$

The largest stress is

$$\sigma_2=\frac{6M_2}{t^2}=\frac{6}{16}q\left(\frac{b}{t}\right)^2=\frac{3}{4}\frac{\sigma_1^2}{E_1}\left(\frac{b}{t}\right)$$

The calculations of the upper surface show that the beam, column and rod also only require second direction fiber. When estimating, not calculating the basic body's strength and hardness, we obtained the strength and hardness of the composite material as $E_1=\frac{n_1}{n_1+n_2}E_0$, $\sigma_{1B}+\frac{n_1}{n_1+n_2}\sigma_0$, $\sigma_{2B}=\frac{n_2}{n_1+n_2}\sigma_0$. In the formulas, n_1 and n_2 are the first and second direction fiber quantities of the composite material. E_o and σ_o represent the elastic modulus and strength of the fibers. From

$$\sigma_1\leqslant\sigma_{1B},\ \sigma_2\leqslant\sigma_{2B}$$

we obtained the ratio of the two directions of fibers

$$\frac{n_2}{n_1}=\frac{\sigma_2}{\sigma_1}=\frac{3}{4}\frac{\sigma_0}{E_0}\left(\frac{b}{t}\right)$$

Other sectional forms can also use this method for processing. Only if there is a rationally disposed fiber quantity can the strength properties of the fibers be brought into full play.

The strength and elastic modulus of the fibers are far greater than the strength and elastic modulus of the basic body, that is $\sigma_{fb} \gg \sigma_{mB}$ and $E_f \gg E_m$. When in the preliminary design, by not calculating the strength and elastic modulus of the basic body excessive, errors will not occur. In this way, the strength design of the structure can be summarized in one sentence: arrange a fixed quantity of fibers in a certain direction. This is sometimes called network analysis. When linked to technical feasibility and load randomness, it is not possible to place all of the fibers on the main stress direction and it is only possible to place the fibers in the main stress direction within a certain area. The stress in this area can still have σ_1, σ_2 and τ_{12}, and besides requiring fibers in one and two directions it is also necessary for the 45° direction fibers to have bearing shearing force. The example shown in fig. 3 illustrates this.

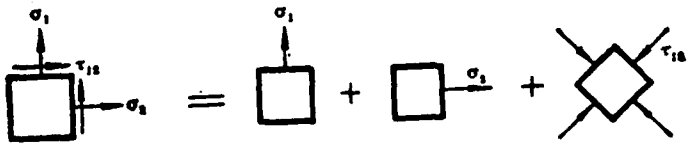

Fig. 3 Stress Ratio Vs. Fiber Volume Ratio

The Stress ratio is σ_1: σ_2: τ_{12}=1:0.5:0.2; the fiber volume ratio is 1:0.5: (0.2+0.2)

After first selecting the fiber volume ratio, the formation of this layered plate is known and afterwards the stress of a single layer is calculated according to the analysis method for layered plates. Further, a suitable strength criterion is selected for examinations and revisions are carried out so that thickness

reaches the thinnest state. The properties of composite layer plates are superior to the properties of single layer plates.

Attention should be given so that the resin base composite material has three low property values: tensile strength σ_{TB} of the vertical fiber direction; and shearing strength τ_{LTB} and shearing elastic modulus G_{LT} of the vertical fiber direction. The use of unidirectional thread composite layered plates is not necessarily the more appropriate plan. The use of fabric with the same longitudinal and latidudinal directions or (and) fabric with different longitudinal and latitudinal directions as the reinforcement material is sometimes suitable.

II. Non-Restriction of Structure's Configuration

At present, the structural designs of glass fiber reinforced plastic composite materials are still in the "replacement design" stage. During the preliminary stage, this type of design is the only way. Yet it should be stated that it is not a good method owing to the fact that when there is replacement of individual parts, they are constrained by the surrounding structures so that full play cannot be given to the points of the composite materials for the simultaneous design of materials and structure.

Prior to molding, the fibers are soft, the basic body is flowing and the supporting mold forms the composite material product. It is unlike the customarily used metal or wood materials which require the assemblage of complete materials. Because of this, the size and thickness of the component is not influenced by becoming full sized but can be determined according to design requirements. When beginning to consider structural designs on composite materials, we should, as far as possible, join the joinable structural components into a part. For example, beam, rib and plate structures do not necessarily need to first mold

beams, ribs and plates but later we can carry out the putting together so that one composite part is formed at a time. In this way, we decreased the joining, the amount of assemblage work and the mold lightened the weight of the structure, and also raised the quality of the product, thus lowering the cost. Fig. 4 is a full GRP antenna. It is composed of 6 ribbed fan surfaces, one central circular surface and one joined cone. The prototype structure is a steel structure composed of a central circular hole, radiating beams and circular rings which are installed on a GRP honeycomb sandwich construction reflecting surface or metal reflecting surface. This type of structure is relatively light in weight and the GRP only acts as the base material of the metal network. It does not bring the special features of the GRP lightness and high strength into full play. The modified design assimilated the structural layout scheme of the metal structure and used the GRP's special features of lightness, high strength and easy formation. This decreased the number of single structural components and the amount of assembly work. At the same time, this caused the weight of each component to decrease so that they can be lifted by a person and put on the back of a horse . If the strong points of the rotating shell are brought into full play, this can cause the structure to be even more succinct. Furthermore, if a helicopter's rotary wing uses composite materials, it is easy to manufacture a twisted rotor blade to replace the conventional level and straight rotor blade and this raises aerodynamic performance [3].

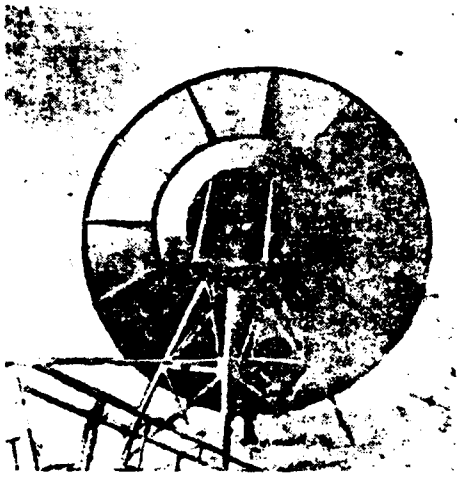

Fig. 4 Full GRP Antenna

The stiffness of the structure is not only related to the elastic modulus of the material but also to the configuration of the structure. To raise stiffness it is necessary to consider two aspects. The first was already given attention, the finding many types of high modulus materials; the second has not been given enough attention. It was mentioned previously that glass fiber reinforced plastic/composite materials have three low material property values and although we can avoid using these low values in lamination designs, should rather use the relatively high values G_{45} and τ_{45}, yet it takes as its cost the sacrifice of the longitudinal elastic modulus and strength. When necessary, we can also use this type of processing so that it slightly loses some longitudinal properties in exchange for raising the shearing properties. By changing the structural configuration we can possibly attain better advantage, be able to manufacture a closed type rod but not an open type rod, and be able to select

a thick type not a thin type structure. Taking a diving board as an example, a metal diving board is a comb type while one made of wood is a solid board. When designing a glass fiber reinforced plastic diving board, if we use a wooden board prototype, then the weight is excessive; if we use a metal structure prototype then very large twisting and swaying can occur. The square tube section (□□□□□□) is much more suitable. To give another example, because considerations for the initial structural configurations of the aircraft nose's radar cap were not complete, it was not able to pass static water pressure tests. Afterwards, although it was strengthened it still lost electronic properties. If considerations were more complete during preliminary designs each radius of the cap's curvature would be suitably adjusted and at the same time we could completely satisfy the mechanical and electronic requirements.

The properties of fiber composite materials possess very strong directionality and even if configuration selection is correct, if at the time of formation we do not control the fiber direction there can be a loss of effectiveness. There can also be difficulty in analyzing strain data during the structural tests because of the unknown elastic modulus of the measuring points. Taking again the above mentioned aircraft nose cap as an example, to fully utilize the properties of the fibers we separated five regions during the formation of the cap and among four of these five we made every effort to use the coincidence of the fiber direction and buckling axis to raise buckling resistance capabilities. For the other region we made the isotropy accurate.

III. The Linear Elasticity and Strength Dispersion of the Materials.

The stress-strain relation up to fractures of many fibers and other composite materials are linear and only in the

unfractured range is there very weak "plasticity." This is caused by the gradual fracturing of the fibers. It is different from metal and therefore this type of composite material has no apparent plasticity area. Thus it does not have the capabilities to alleviate the defective area's high stress so that relatively large strength dispersion occurs. People have frequently blamed composite material properties as being unstable and when a composite material breaks down quite a few material properties are unstable yet rarely do people consider the problems of design or material properties selection indices. Actually, whether a material's properties are stable or not is related to the selection index. Taking the yield limitations of number 3 steel as an example, the smallest value measured is 17 kg/mm^2, maxmimum value is 42 kg/mm^2 at a difference of $2\frac{1}{2}$ times. If we take 30 kg/mm^2 as the yield index for number 3 steel, it is feared that many will say that the properties of the steel are unstable. However, the use of 24 kg/mm^2 as the yield index guarantees an over 99 percent probability of exceeding this index and thus people will say the properties of the steel are stable. This type of index should also be fixed for composite materials. Taking non (low)-alkali glass fiber as an example, when its strength discrete coefficient is about 10 percent, if we strictly control the manufacturing techniques of the composite materials, its discrete coefficient can be smaller than 10 percent. This is because the probability of the weakest point of each fiber appearing simultaneously on a section is very small. However, because in most glass fiber reinforced plastics the partial difference of the fiber direction and the resin content are not uniform, this causes the discrete coefficient to reach 15 percent and when compared to the 8 percent discrete coefficient of the number 3 steel's yield limitation, the property dispension of the glass fiber reinforced plastic materials is a little greater. It is necessary for structural designers to recognize that this dispersion is an objectively existing and suitably correct limiting performance value. The two limiting values for criterion in the standard 5A

used by the United States military are: one is the "A" criterion which takes a performance value guaranteed 99 percent probability under 95 percent believability as the limiting value. Generally used after efficiency is lost it causes a situation wherein the totality of the structure is lost. The other is the "B" criterion which takes a performance value guaranteed to exceed 90 percent probability under 95 percent believability. Generally used after efficiency is lost the outer load is redistributed to other bearing force components [4]. These types of considerations are also suitable for composite materials. After determining the limiting value, it is also necessary to formulate a safety factor. British standards consider six factors. The first is basic safety factor 3 and the other five are factor 1.4-3 related to production methods, 1.2-2 related to bearing time, 1-1.25 related to operating temperature, 1.1-2 related to alternating frequency, and factor 1.1-1.5 related to the solidification system. The product results range from 6 to 40 [5]. The use of these types of safety factors cause the strong points of the composite materials, lightness and high strength not to be manifested.. In the NACA Lewis Research Center of the Structural Composite Materials Industrial Company (SCI Inc.) of the United States, the operating pressure of the modelled epoxy Kevlar 49 spherical container is 1.9 kg/mm^2, the blast pressure is 3.27 kg/mm^2 [6], and the corresponding safety factor is 1.7. When the glass fiber reinforced plastic diving board was mentioned previously for the preliminary design, we first used safety factor 10 for the dead load design and after the dynamic load was checked and we obtained a safety factor of 2.37, the selected safety factor appeared a little smaller when fractures appeared in the small batch of plates used. It should be determined which composite material safety factors are worth examining. Taking glass fiber reinforced fiber as an example, even though we have a fixed quantity of products, nevertheless most of the designs are reasonable. Some don't even have the properties of raw materials,,

and the lack of daily records causes there to be no way of carrying out analysis after structural efficiency is lost. Designers should know in relative detail the load and utilization environment and should also obtain relatively reliable material property data from sufficiently large subsamples so as to formulate relatively reasonable safety factors.

We already know that fiber strength is related to the defects which exist in the fibers and the distribution of the defects are random. The longer the fiber length, the greater the probability of defects appearing and thus its strength will be lower. On the contrary, when fiber length is shorter there is a smaller probability of large defects appearing and the strength can then be higher. It is very natural that when designing composite material structures we must consider the relationship of the structure's measurements and the material's strength. Taking the example shown in fig. 5, three simply supported beams are subjected to maximum bending moment $\frac{1}{4}$ PL and we can no doubt select equal measurement beams among conventional materials.

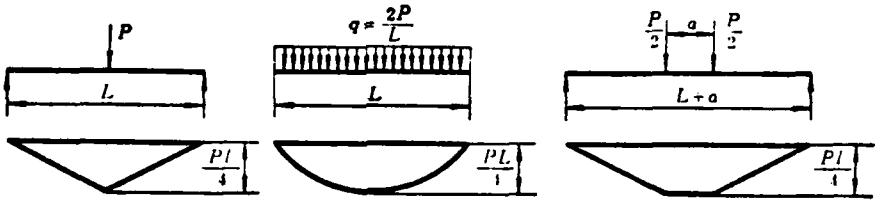

Fig. 5 Three Simply Supported Beams Subject to Equal Bending Moment

This can also be done for composite materials. The most suitable method should consider thesize of the area occupied by an equal stress level and the largest stress area of the three points of the additional load beam are much smaller than the largest area of the four points of the additional load beam. Secondly, the

large stress area is also smaller than the evenly distributed load beam. Thus, the sectional measurements of these three beams should be different and the measurements of the latter two should be larger than the three points of the additional load beam. These problems are not very outstanding on small measurement structures, yet consideration should be given on large scale structures. When handling these problems, we can use the weakest chain analytical method to establish the relationship of strength and length as shown in fig. 6.

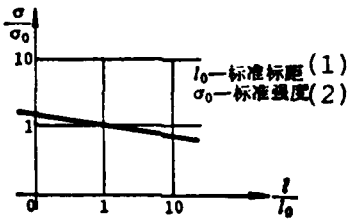

Fig. 6 The Relationship of Strength and Length

Key: 1. Standard scale distance
2. Standard strength

This relationship is also suitable for width. For the relationship of strength and thickness we can consider that the probability of the weakest position of each thin layer concentrating on the same section is very small. When thickness increases, the strength can be raised close to the mean strength as shown in fig. 7 and the use of the weakest strength of the thin layer for design tends to be safe.

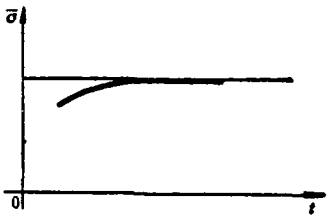

Fig. 7 The Relationship of Strength and Thickness

IV. Conclusion

To design well a composite material structure, it is first necessary to understand the outer loads clearly, especially the secondary loads. This is because the second direction strength of single direction composite materials is very weak. Furthermore, it is also necessary to sufficiently understand the operational environment of the structure so as to be able to select suitable base body and reinforcement materials. Secondly, it is also necessary to have full knowledge of the material's properties as well as needing to obtain reliable data on the material's properties of large subsamples. Lastly, designers must carry out analysis in as much detail as possible so that normal work can be carried out on structures even under the worst conditions.

References

[1] Zhu Yiling, "Summary of the Mechanical Characteristics of Glass Fiber Reinforced Plastics and Other Composite Materials," Mechanics and Practice, Vol.2,No.1(1980),pp.1-6.

[2] The Shanghai Research Institute of Glass Fiber Reinforced Plastic Structures, "The Design of Glass Fiber Reinforced Plastic Structures," China Architecture Industry Publication (1980).

[3] Holmes, R.D. "S-glass Reinforced Plastics Adopted for Helicopter Rotor Blades" SAMPE Quarterly Vol. 7 No1. PP 28-41 Oct. 1975.

[4] Jones B.H. "Probabilistic Design and Reliability" 《Composife Materials》 Vol.8 PP32-72 Academic Press 1975.

[5] Moore,P.T. "A New Design Method for Structures of Laminated Constructions" 《Proceeding of the 1975 International Conference of Composite Materials》 Vol.2 PP52-71.

[6] 《SPI exhibited Products guide》 35th annual conference & exhibited reinforced plastics/Composites 1980.

COMPUTATION OF STRENGTH AND STABILITY FOR A BUILT STRUCTURE

by Cai Yiping, Song Zenghao, Wang Zhihua, Zhang Xianwu
(Computation Technique Research Institute of the China Aviation Research Institute)

Zhang Zugian
(Design Institute of the Hongan Aircraft Company)

Abstract

This paper is devoted to solving strength and stability problems of a built structure by using the finite element method and the increment method for the geometrical nonlinear structural problem. Structural elements include bar, plane, beam, space beam, triangular and rectangular plates with membrane stresses, rectangular plate element with bending deformations. Harmonization between platebar and beam is carried out by using infinitely stiff component. When the generalized eigenvalue problem is solved with the aid of a simultaneous iteration algorithm, the initial test vector may be automatically generated by means of random numbers. In the paper some techniques in computational procedure are also described, and a few numerical examples are given.

We have written a general purpose program in FORTRAN IV language. The program possesses the advantages of short computing time, good generality and convenience for use.

I. Preface

Among structural problems, when deflection is large enough to cause noticeable changes in the structure's geometrical

configuration to the point where an equilibrium equation must be established based on the configuration after deformation, geometrically nonlinear phenomena occur. An important condition of geometrically nonlinear problems is large displacement and small strain. The properties after elastic buckling of the structure is one example of this subcategory.

The computation of the stability of complex structures is an important problem for structural analysis. Because of the existence of geometric nonlinearity the stress conditions of the beams and plates are generally relatively complex and the boundary conditions are generally very difficult to determine. Thus, to attempt to find a solution beginning from differential equations is quite difficult.

Since the 1960's, the development of the finite element method and numerical value analysis method have been brought forth as powerful tools for solving this problem. Used for linear structures, it combines the developed matrix analysis method with the gradually linearized increment method, being a means with which to solve nonlinear structure analysis problems. At present, there are many methods used for solving the large deflection problems of geometrical nonlinear analysis and generally speaking they can be divided into three categories: the increment method, iteration method and combination method. The good and bad points of the methods have been discussed by many writers [1] and is not within the scope of this paper. Therefore, we will use the increment method because that method is relatively intuitive, is convenient to use and is able to entirely describe the load-deflection characteristics.

Mathematically, computation of stability requires solving a generalized eigenvalue problem

$$K_E q + \lambda K_G q = 0$$

In the formula, K_E is the total elastic stiffness matrix and K_G is the total geometric stiffness matrix. Based on the model's smallest eigenvalue we can compute the structure's destabilized critical load. Further, the corresponding characteristic vector is a destabilized waveform.

We used FORTRAN IV language to write a general purpose program for computing the strength and stability of the plate, bar and beam built structure as well as to compute some examples and problems. The results were relatively satisfactory.

II. Computation Methods

1. When an elastic continuous medium is in a small deflection, the strain-displacement equation can be viewed as linear and when existing within external force p and displacement U, there is the following linear relation:

$$KU = p \qquad (1)$$

Yet, when the structure has large deflection, we must consider the geometric configuration changes caused by displacement. At this time, the high order item (nonlinear item) in the strain-displacement equation cannot be overlooked. These nonlinear items cause the element's stiffness matrix k to be changed into

$$k = k_E + k_G \qquad (2)$$

K_E is the ordinary elastic stiffness matrix and k_G is the geometric stiffness matrix. They are not only related to the geometric measurements but also connected to the internal force existing when the computation steps begin. After the elastic and geometric stiffness matrices are ascertained, we can form the total stiffness matrix

$$K = K_E + K_G \qquad (3)$$

In this way, we can use a conventional method to solve the displacement and stress.

2. To consider the geometric configuration changes when the external load gradually increases, we used a series of linear steps to make approximations for the nonlinear problem. Each step represented one load increase. This method is called the increment method [1,2].

While using the increment method procedure, each step should compute the model's nodal point coordinates based on the displacement increased changed structure and then proceed to find the new stiffness matrix and geometric matrix.

3. When a certain metric standard p* is selected for the external load, the external load is

$$p = \lambda p^*$$

Because the geometric stiffness matrix forms a ratio with the internal force when the steps begin, thus

$$K_G = \lambda K_G^*$$

Therefore we have

$$(K_s+\lambda K_G^*)U = \lambda p^*$$
$$U = (K_s+\lambda K_G^*)^{-1}\lambda p^*$$

We can see from this that when

$$|K_s+\lambda K_G^*| = 0 \qquad (4)$$

displacement U tends to be infinitely great. We found the modular minimum value of λ from equation (4) and represented it as $\lambda_{critical}$. Thus we can obtain the structure's destabilized

critical load

$$p_{cr}^{(1)} = \lambda_{cr}^{(2)} \cdot p^{*} \qquad (5)$$

Key: 1. Critical; 2. Critical

It can be seen from equation (4) that the structure's destabilization equation is

$$(K_E + \lambda K_G^{*}) q = 0 \qquad (6)$$

This is a generalized eigenvalue problem. The minimum eigenvalue found is $\lambda_{critical}$ and its corresponding characteristics vector is a destabilized waveform.

4. The structural elements include the bar triangular and rectangular plates rectangular plate element with bending deformations, beam and space beam. Their elastic stiffness matrix and geometric stiffness matrix can be seen in references [3,4,5]. To economize on the contents and extend the scale of computations, all of the elastic stiffness matrices and geometric stiffness matrices after total loading used a one-dimensional change band width store pattern.

5. The harmonization between the beam, plate and bar used the infinite stiffness element process method. The stiffness component used in the joining area of the plate, bar and beam can guarantee that the deformations in each element are harmonized. The use of the rigid body displacement law can determine the displacement relation of each nodal point on the infinite stiffness component and the use of the principle of virtual work can find the relation of each nodal point on the rigid body. Here, we will only give as an example the joining of bar jk and beam as showing in fig. 1. Other cases can be attained analogously [5].

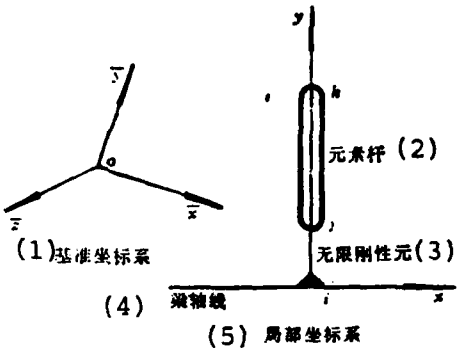

Fig. 1 A Case of Joining Bar to Beam

Key: 1. Basic standard coordinate system
2. Element bar
3. Infinite stiffness element
4. Beam axis line
5. Local coordinate system

Here, component ji is an infinite stiffness component, point i is the fixed joining point, point j is the hinge point, and the displacement of joint j is determined by the displacement and corner of point i, that is

$$\{\delta_j\}_{3\times 1}=[T_{ji}]_{3\times 6}\{\delta_i\}_{6\times 1} \qquad (7)$$

In the formula

$$[T_{ji}]_{3\times 6}=[I_3 \quad b_{ji}]$$

$$[b_{ji}]_{3\times 3}=l_{ji}\begin{bmatrix} 0 & \cos\gamma & -\cos\beta \\ -\cos\gamma & 0 & \cos\alpha \\ \cos\beta & -\cos\alpha & 0 \end{bmatrix}$$

I_3 is the third order unit matrix, λ_{ji} is the length of stiffness component ji, and $\cos\alpha$, $\cos\beta$ and $\cos\gamma$ are the direction cosines of $\vec{ij}$.

If the jk bar's original stiffness matrix is $[\bar{k}_{jk}]_{6\times6}$, after using point i displacement to replace point j displacement, the stiffness matrix of bar jk is

$$(k_{jk})_{6\times6}=\begin{bmatrix} T_{ji} & \\ & I_3 \end{bmatrix}^T_{6\times6}(\bar{k}_{jk})_{6\times6}\begin{bmatrix} T_{ji} & \\ & I_3 \end{bmatrix}_{6\times6} \tag{8}$$

The equilibrium equation is

$$\begin{Bmatrix} Q_{xi} \\ Q_{yi} \\ Q_{zi} \\ M_{xi} \\ M_{yi} \\ M_{zi} \\ Q_{xk} \\ Q_{yk} \\ Q_{zk} \end{Bmatrix} = (k_{jk})_{6\times6}\begin{Bmatrix} u_i \\ v_i \\ w_i \\ \theta_{xi} \\ \theta_{yi} \\ \theta_{zi} \\ u_k \\ v_k \\ w_k \end{Bmatrix} \tag{9}$$

This type of point j does not appear in the total stiffness matrix and in the same way the external load on point j must also have an equivalent transformation up to point i

$$\{p_i\}=(T_{ji})^T\{p_j\} \tag{10}$$

6. To obtain the characteristic value and characteristic vector as well as the partial characteristic value and characteristic vector of equation (6), we used a simultaneous iteration algorithm [7]. At this time, equation (6) can be written in the following forms:

$$Bx=\frac{1}{\lambda}Ax$$

or

$$Bx=\mu Ax \qquad (11)$$

In the formula, A(e.g. K_E) and B(e.g.-K_G^*) are both real symmetrical matrices and A is fixed. Using Cholesky decomposition, $A=LL^T$, equation (11) then changes into the ordinary characteristic value problem of the real symmetrical matrix

$$L^{-1}BL^{-T}y=\mu y \qquad (12)$$

In the equation $y=L^Tx$ (13)

Several characteristic values of μ_i, are the largest derived by a simultaneous iteration algorithm but we required the smallest λ_i. Thus, when using this method we exchanged the K_E and K_G^* positions.

It should be pointed out that before using a simultaneous iteration algorithm, we must first carry out matrix compression of K_E and K_G^*, and delineate the lines and rows corresponding to the known displacements. This is more complex than using the one-dimensional change band width stored K_E and K_G^*. If the method is not suitable and the order of the matrix is high, expenditures will be startling. Our designed "revised fixed position method" computed and determined the positions of each element after delineating the lines and rows from back to front so that it was only necessary for each element to shift once. This greatly economized on time.

It is worth pointing out that if a person hopes to find l characteristic values then it is much better to use m ($>l$) vectors for iteration. This is because the converging speed of k characteristic vectors depend on $|\mu_{m+1}/\mu_k|$, and the smaller the specific value the faster the convergence. Taking m $>l$, the extra amount of work expended for each time of iteration is compensated for because of the large raising of convergence speed. Experience has proven that taking m as about 1.5 times of l is relatively suitable.

Finally, we think that a simultaneous iteration algorithm not only improves convergence but also does not necessitate anything like the power method wherein after each time of finding a characteristic value it is necessary to carry out contraction of the matrix. When an initial approximation is provided for the characteristic vector, the computer program still possesses the function of using random numbers to produce initial test vectors.

III. Computation Examples

Example 1. On p. 268 of reference [2] there is an analysis of the stability of a simple truss. Our computation results are the same as those of reference [2].

Example 2. We also carried out stability analysis of a column with one end solidly joined and the other end hinged which was found on p. 271 of reference [2]. Computation results were identical.

Example 3. We analyzed the stability of the plate and bar built structure shown in fig. 2. The structure is composed of 20 bars, 6 triangular plates and 8 rectangular plates. There are a total of 12 nodal points: the 4 nodal points on the lower part are fixed and the 4 on the top part separately sustain external

loads of 1,000 kilograms. The bar element's sectional area is $A=1\ cm^2$ and the plate element's thickness is $t=0.1$ cm. Elastic modulus $E=0.72\times10^6 kg/cm^2$. Poisson's ratio $\mu=0.3$, and the load increments are $0.1P^*$, $0.3P^*$, $0.3P^*$, $0.3P^*$, respectively.

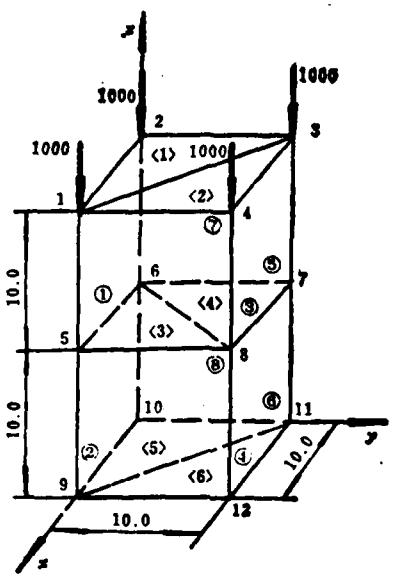

Fig. 2 A Structure Built of Plates and Bars

After computations we obtained

$$\lambda_{critical}=115.3$$

Thus, on the top four points there is

$$P_{critical}=115.3\times10^3 \text{ kilograms}$$

Computation results prove that the distribution of displacement and stress conforms to the pattern, and the $\lambda_{critical}$ value and related materials match.

IV. Conclusion

1. In essence, the stability problem of a built structure

should belong in the nonlinear theoretical range of elastic mechanics. In computations, we used the microdisturbance criteria of the nonlinear large deflection theory and elastic stability theory. A built structure is not a perfect system and a large quantity of computations have shown that the critical loads of built structures are extreme. When a built structure reaches critical load, the level of the structure's main support force component stress is relatively low but the levels of stress of certain secondary components is relatively high. Thus, proper adjustment of the geometric measurements of components with higher stress levels is advantageous to raising the structure's critical load.

2. When using the increment method for solution, the external loads make up gradual step loading. During each step nonlinear influence is small and it is only necessary that the load increment be sufficient. The solution of each step's increment can be obtained accurately and the precision of the displacement's total value and internal force can be raised. In reality, even if we use the relatively large linear computation steps of these problems, we will still obtain results very close to the structure's real nonlinear properties.

Because the first step of the increment method is an elastic solution, the added load increment must be as small as possible so as to decrease the computational errors of the displacement.

3. After testing several examples, computations were carried out for a certain fuselage composite beam computation model and the results were satisfactory.

References

[1] C.S. Desai and J.F. Abeier, authors, Jiang Bonan and Yi Zeyong, translators, "The Theory of the Finite Element Method," Science Publications, 1978.

[2] J.S. Puqminisiji, author, Wang Derong et.al. translators, "The Theory of Matrix Structural Analysis," National Defense Publications, 1974.

[3] J.S. Przemieniecki, "Discrete-Element Methods for Stability Analysis of Complex Structures", The Aeronautical Journal, 1968, Vol. 12.

[4] A.P. Kabaila, B. Fraeijs, "Bifurcation of Space Frames", AD.704570. 1970.

[5] Song Zenghao, Xiang Zulian, Cai Yiping, Wang Zhihua and Zhang Xianwu, "Computations of the Strength and Stability of Plate, Bar, Beam Build Structures", Materials from the Annual Mathematical Exchange Meeting of Shaanxi Province, 1980.

[6] The Huadong College of Water Conservancy, "The Finite Element Method For Elastic Mechanics Problems", Water Conservancy and Electric Power Publications, 1974.

[7] R.B. Corr, A. Jennings, "A Simultaneous Iteration for Symmetric Eigenvalue Problems", Int.J.Num. Math.Engng, 1976, Vol. 10.

STUDY ON TIME BETWEEN OVERHAULS (TBO) OF AIRCRAFT TURBOJET AND ITS RELIABILITY

by Zhang Yimin
(Shanghai Aviation Industry Corporation)

Abstract

In this paper statistical methods (frequency histogram, probability paper, linear regression, chi-square χ^2 tests) are applied to analyzing TBO of aircraft engines. The calculated results of three types of aeroengines have shown that the normal distribution is an appropriate model for TBO of aircraft engines. Therefore, along with the given value of TBO, it is reasonable to indicate the probability of the actual operating time of aircraft engines exceeding the given TBO. It is suggested to express the TBO by $H(R_K\%)$. Thus many unnecessary overhauls can be avoided which is of significant economical importance. The mean TBO of normal distribution $\bar{H}=H(50\%)$ is recommended as the parameter of aircraft engines for overhaul. While accepting the mean TBO concept, on-condition maintenance and condition monitoring technology must be adopted in engine operation in order to obtain sufficient flight safety. If the over 50% actual operating time of aircraft engines is greater than the mean TBO in airline operations, the TBO can be prolonged. The method for estimating the prolonged life is also given.

Reliability is obviously very important in the operating performance of aircraft engines. This is because the reliability of an aircraft engine is directly related to the flight safety. At the beginning of the 1950's when turbojets were first put into operation, very stringent TBO control methods were adopted to

guarantee the reliability of engine operation. Yet operation experiences showed that TBO could not be an index for the reliability of flight operation [1] and that after a large number of engines operated in excess of the TBO they could still operate normally. However, many engines had breakdowns within the stipulated TBO period and moreover the reliability of the engines did not increase with operation time to a certain value but noticeably worsened. Therefore, we indicated the reliability with probability, within a fixed amount of time and under stipulated operation conditions, there was no hindrance to giving play to the probability of stipulated performance. Fig. 1 gives the frequency histogram of the TBO distribution for 284 CF6 engines within 917,500 flight hours. The longest reached to over 6,000 hours and the shortest was only 100 odd hours. The TBO mean value $\bar{H}$ was 3,231 hours and variance s was 1,358 hours. Fig. 1 also gives the curve calculated according to the normal distribution, Weibull distribution and exponential distribution which shows that the CF6's TBO distribution is close to the normal or Weibull distributions.

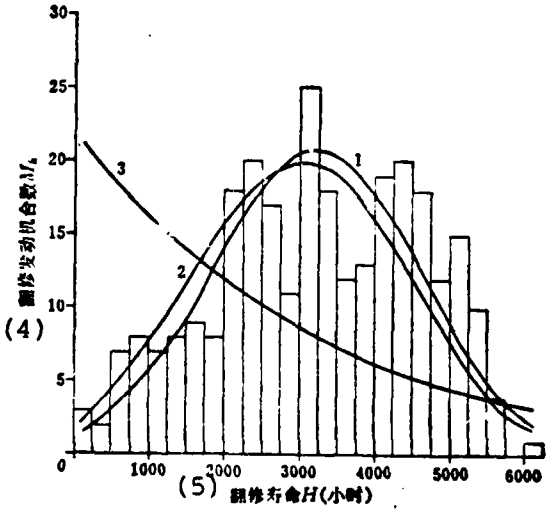

图 1 CF6翻修寿命频数直方图
(1—正态分布 (2—威布尔分布 (3—指数分布

Fig. 1

AD-A118 973 FOREIGN TECHNOLOGY DIV WRIGHT-PATTERSON AFB OH F/G 12/1
ACTA AERONAUTICA ET ASTRONAUTICA SINICA.(U)
JUL 82
UNCLASSIFIED FTD-ID(RS)T-0518-82 NL

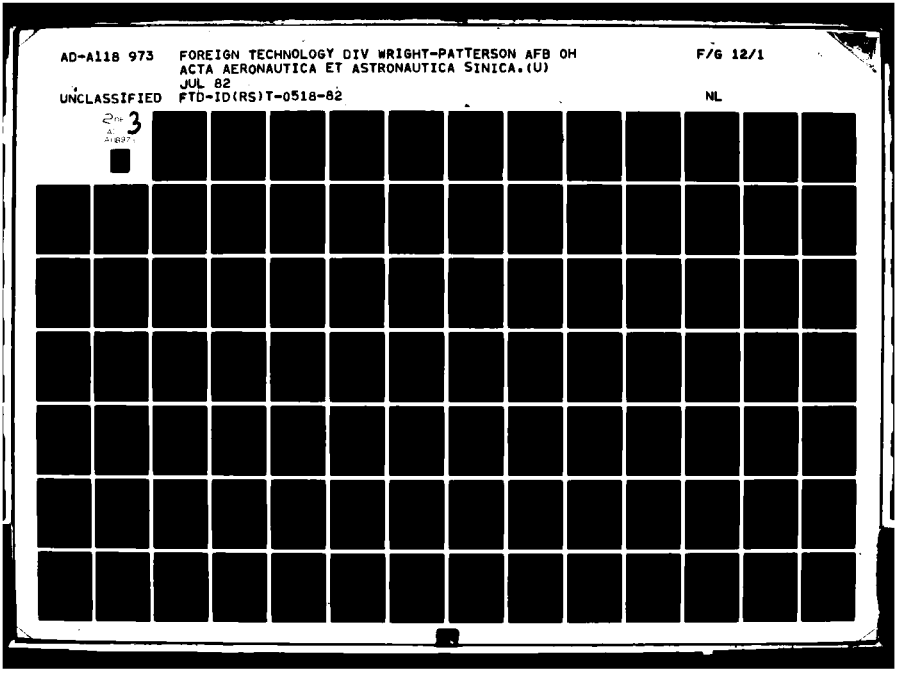

Fig. 1 Frequency Histogram For TBO Data of CF6

Key: 1. Line 1 - normal distribution
2. Line 2 - Weibull distribution
3. Line 3 - exponential distribution
4. Number of overhauled engines M_k
5. TBO H (hours)

Further, the operation reliability and TBO relation of the CF6 is separately drawn on normal distribution probability paper, logarithmic coordinate paper and Weibull distribution coordinate paper. Operation reliability R_k is the percentage occupied in a normally operating engine within stipulated time H_k. It is also the engine percentage when the TBO exceeds H_k hours. Therefore:

$$R_k = 1 - \frac{\sum_{i=1}^{k} M_i}{N} \qquad (1)$$

In the formula, M_k is the TBO's engine number in the i interval and N is the total number of operating engines within this batch.

We used linear regression analysis for the 24 groups of statistical data for the CF6 in fig. 1 to find its regression function formula. In this way, there were many errors yet calculations were convenient, could be carried out on a programmed calculator (such as TI-59) and need not use a computer. For standard normal distribution N (0,1), standard deviation Z was the variable [2], and the definition of Z is:

$$Z = \frac{H - \bar{H}}{\sigma} \qquad (2)$$

In the formula, σ is the generating variance. Yet, when the TBO is based on the normal distribution, the relation between reliability and Z is

$$R_k = 1 - \Phi(Z_k) = 1 - \int_{-\infty}^{Z_k} \frac{1}{\sqrt{2\pi}} e^{-\frac{Z^2}{2}} dZ \qquad (3)$$

In the formula, $\Phi(Z_k)$ is called the normal probability integral and we can table look-up [2] or use a program stored in the TI-59 calculator for calculations.

The 23 groups of data in CF6 (see fig. 1, the one group of R_k=0 is deleted) finds R_i based on equation (1) and then from the derived R_i we find Z_i by using equation (3). We then derive 23 groups of data for H_i and Z_i and by regression analysis obtain:

$$Z = -2.43175 + 0.00077158H \qquad (4)$$
$$r = +0.9876$$

The correlation coefficient is r=+0.9876. Equation (4) and the 23 groups of data (H_i, Z_i) are drawn on normal probability coordinate paper. We know from fig. 2 that the 23 groups of data (H_i, Z_i) are very close to regression line (4) and that when the correlation coefficient is close to 1 the TBO of CF6 coincides with the pattern of normal distribution.

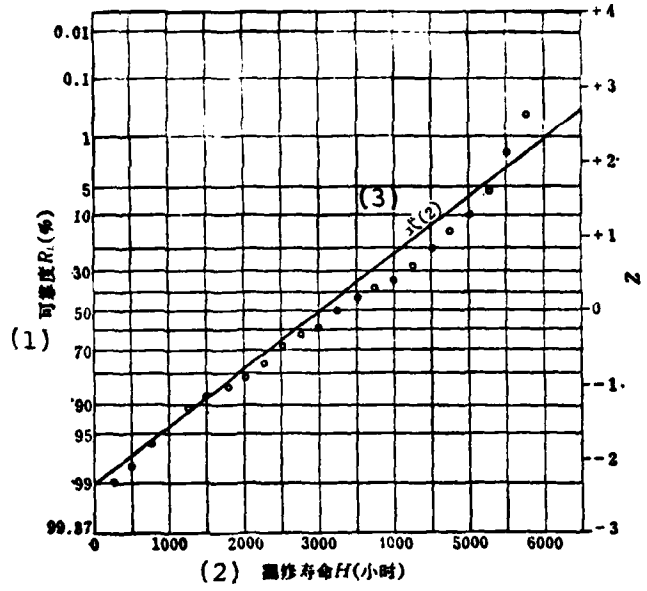

Fig. 2 Estimated Regression Line According to Normal Distribution and Reliability of CF6

Key: 1. Reliability R_k (%)
2. TBO H (hours)
3. Equation (2)

When we used the same regression analysis method (23 points) for the exponential distribution, we obtained:

$$\lg R = 2.44308 - 0.00030828H \qquad (5)$$

When correlation coefficient r= -0.83821, this shows that the linear relation between lgR and H is not close and from fig. 3 we know that the actual measuring points are far apart from the regression line.

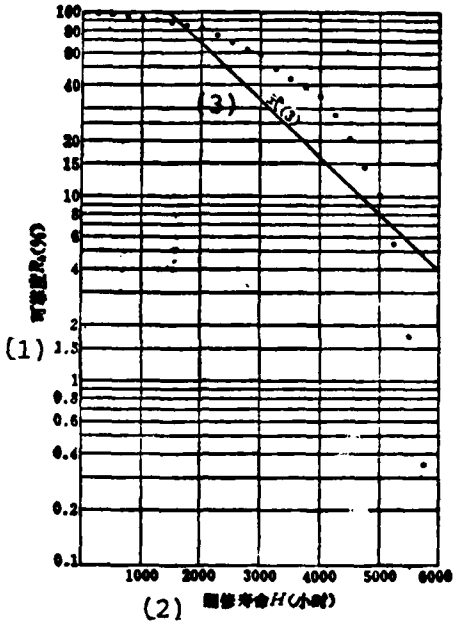

Fig. 3 Estimated Regression Line According to Exponential Distribution and Reliability of CF6

Key: 1. Reliability R_4 (5)
2. TBO H (hours)
3. Equation (3)

For the Weibull distribution, we used regression analysis to determine configuration parameter m and measurement parameter S_o; we determined position parameter a_o based on the χ^2 in the χ^2 test which is the minimum value condition. χ^2 is determined by the following equation:

$$\chi^2 = \sum_{k=1}^{n} \frac{(NP_k - M_k)^2}{NP_k} \qquad (6$$

In the equation, P_k is the probability of the operating TBO in the k interval. See table 1 for the calculated results of the χ^2 tests. It was more suitable for a_o to be taken as -1200.

(1) 分布类型	(2) 正态分布	(3) 指数分布	(4) 威布尔分布			
			$a_0 = 0$	$a_0 = -1100$	$a_0 = -1200$	$a_0 = -1300$
(5) 相关系数 r	0.9876	0.83221	0.96016	0.99537	0.99538	0.99534
$\chi^2 = \sum_{k=1}^{24} \chi_k^2$	34.75	262.81	49.91	32.247	32.246	32.868

Table 1 The Calculated Results of χ^2 Test

Key: 1. Type of distribution
2. Normal distribution
3. Exponential distribution
4. Weibull distribution
5. Correlation coefficient r

In this way, we find that the Weibull distribution regression formula is:

$$\ln \ln \frac{1}{R_k} = -30.9575 + 3.64786 \ln(H + 1200) \qquad (7)$$

When correlation coefficient r=0.99538, this shows that its linear degree of correlation is relatively good. We know from fig. 4 that each actual measuring point is relatively close to the line (equation 7).

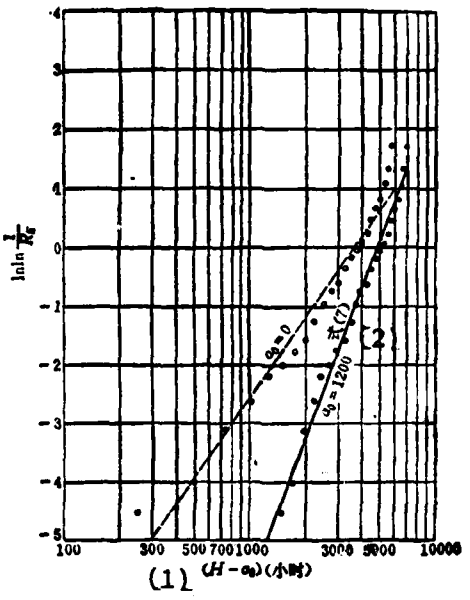

Fig. 4 Estimated Regression Line According to Weibull Distribution and Reliability of CF6

Key: 1. (Hours)
2. Equation (7)

Therefore, we know from regression analysis that the real distribution and normal distribution or Weibull distribution of CF6 are all quite close.

To carry out the χ^2 test for the normal distribution, we took samples of $\bar{H}$ and s as the μ and σ of the generating population, took significance a as 0.05 (e.g. believability was 0.95) and degree of freedom v=n-3=21 so as to satisfy the following conditions [2]:

$$\chi^2_{v,\frac{\alpha}{2}} < \chi^2 < \chi^2_{v,1-\frac{\alpha}{2}} \quad (8)$$

Then, the original supposition could be accepted and $\chi^2_{21,0.025}=10.283$ $\chi^2_{21,0.975}=35.479$. We know from table 1 that both the normal distribution and Weibull distribution satisfy the conditons of (8) and this can accept the supposition of the normal distribution and Weibull distribution. When $\chi^2_e=262.81$ during exponential distribution, this does not satisfy the conditions of (8) and thus eliminates the supposition of the exponential distribution.

Further, taking the JT3D-7 engine as an example, there was a total of 224,798 flight hours from July, 1974 to August, 1980. The greatest number of flight hours for one aircraft was 8,039 hours while the manufacturing plant's recommended TBO was 9,000 hours. According to the old TBO concept, it is not necessary to dismantle an engine for overhaul. Yet during this period of actual operation 4 engines stopped in midair and 34 were changed early. The midair stoppage rate was 0.0178 and the early change rate was 0.165. The total flight time of these 38 engines between overhauls was 127,221 hours; there were 4 which did not operate up to 1,000 hours before having to be dismantled for overhaul and the longest time was 7,296 hours. The 38 engines were divided into 7 intervals, $\bar{H}$ was 3, 316 hours and variance was 1,798 hours. According to the

χ^2 test carried out for normal distribution, $\chi^2=\sum_{k=1}^{7}\chi^2_k=5.771$. We know from reference [2] that $\chi^2_{4,0.025}=0.484$ and $\chi^2_{4,0.025}=0.484$ and $\chi^2_{4,0975}=11.143$ which satisfy the conditions of (8) and therefore can accept the supposition of normal distribution. Based on χ^2 as the minimum value condition, we found the Weibull distribution regression formula:

$$\ln \ln \frac{1}{R_t} = -22.9449 + 2.68287 \ln(H_t + 1300) \qquad (9)$$

Correlation coefficient r=0.99345 and $\chi^2 = \sum_{k=1}^{7} \chi_k^2 = 4.675$ satisfy the conditions of (8) and can therefore also accept the supposition of the Weibull distribution.

Statistics on 55 TBO for AH-20M have shown that because of the influence of the old TBO concepts, after the operation of 19 ofthese engines reached the stipulated TBO of 3,000 hours they were dismantled and sent for overhaul without having broken down. Thus, testing should be carried out using one-sided truncated normal distribution and linear regression analysis should be used to determine the mean TBO and variance:

$$Z = -1.84169 + 0.000768046H. \qquad (10)$$

The correlation coefficient is r=0.99581. By comparing formulas (2) and (10), we can know that $\frac{1}{\sigma}$ =1/0.000768046 and $\frac{\overline{H}}{\sigma}$ =1.84169. Therefore, when the variance is 1,302 hours, the mean TBO is 2,398 hours and we calculate $\chi^2 = \sum_{k=1}^{7} \chi_k^2 = 4.177$ which satisfies the conditions of (8). Thus it can accept the one-sided truncated normal distribution supposition. If the truncated supposition is not used, even though we consider the TBO of the 19 dismantled 3,000 hours, $\overline{H}$ os 2.136 hours, s is 890 hours, and $\chi^2 = \sum_{k=1}^{7} \chi_k^2 = 19.208$ which do not satisfy the conditions of (8). Thus, it is necessary to use the one-sided truncated normal distribution. In the same way, we also use one-sided truncated Weibull distribution for testing. Using regression analysis we can obtain:

$$\ln \ln \frac{1}{R_k} = -23.0046 + 2.78383 \ln (H_k + 1000) \qquad (11)$$

Correlation coefficient r-0.99538 and $\chi^2 = \sum_{k=1}^{7} \chi_k^2 = 3.617$.

Thus, it can accept the one-sided truncated Weibull distribution. The above calculations can be completed on TI-59 programmed calculator programming and a stored calling program.

Based on the TBO statistical tests of the above three types of engines, the normal distribution and Weibull distribution are both acceptable. Yet m is about 3 in both the normal and Weibull distribution so that the use of normal distribution was convenient for analysis and calculations and therefore normal distribution was used in later analysis. It can be seen from the above examples that changes in TBO concepts have caused great changes in engine operation and maintenance.

1. According to the old TBO concept of the 1950's, even if the stipulated TBO for the JT3D-7 was 1,000 hours, 10.5% of the engines would not reach the stipulated TBO but would have to be dismantled and overhauled by the manufacturing plant. Because the other 34 engines would have already reached TBO by 1,000 hours of operation, they also had to be dismantled and overhauled. This caused the 34 engines to have 92,388 fewer flight hours occupying 73.1% of the total flight time of 126,388 hours for the 34 engines. This is unnecessary waste and shows that the use of the new concepts possesses significant economic worth.

2. Along with providing the TBO we should also give the probability of the operating life reaching the indicated TBO. The higher the requirements for reliability the shorter the TBO (see table 2).

(1)翻修寿命 / (2)发动机型号	JT3D-7	CF6	АИ-20М
(3) R_k=5%时的翻修寿命, $H(5)$	6500	5250	>3000
(4) R_k=50%时的翻修寿命, $H(50)$	3000	3250	2300
(5) R_k=90%时的翻修寿命, $H(90)$	1000	1250	625

Table 2 The Relationship Between TBO and Reliability For Several Aeroengines

Key: 1. TBO
2. Engine Model
3. R_k=5% of the time TBO, H(5)
4. R_k=50% of the time TBO, H(50)
5. R_k=90% of the time TBO, H(90)

Therefore, the use of $H(R_k\%)$ is proposed for indicating TBO and we can use the mean TBO to replace the old TBO. However, if the relationship between the probability of the actual operating life reaching the mean TBO and its distribution is subordinated to normal distribution, its probability is 50% and thus one half of the engines can reach the mean TBO. Table 3 gives the percentages of the operating lives of several engines which exceed the mean TBO. All approach 50%. Table 3 also gives TBO statistics for several engines used by the United States military [3] which shows that the above new concept for TBO is also applicable in engines for military use.

(1) 发动机型号 (装用飞机)	CF6 (DC-10)	JT3D-7 (波音707)	АИ-24	АИ-20М	Д57-П19 (B-52D)	Д57-П21 (F-100)	TF30-P-3 (F-111)	TF41-A1 (A-7D)
统计台次 (3)	284	(2) 38	102	55	113	167	137	115
平均寿命，小时 (4)	3231	3348	3099	2398	3666	752	556	333
超过平均寿命，R_k% (5)	49.65	42.11	51.96	47.27				
最高翻修寿命，小时 (6)	8125	7296	>4000	>3000	4000	1000	1000	750

Table 3 The Mean TBO of Several Aeroengines

Key: 1. Engine model
2. (Boeing 707)
3. Statistical numbers
4. Mean life, hours
5. Exceeding mean life, R_k%
6. Highest TBO, hours

3. The use of the midair stoppage rate as an aircraft reliability index. After using the mean TBO concept, about one half of the aircraft still did not reach the mean TBO but had breakdowns. Therefore, within each 1,000 engine flight hours the number of times the engine itself had midair stoppage and the number of times it had to be changed early are called the midair stoppage rate and early change rate. We used the midair stoppage rate as the main engine reliability index. Engine manufacturing plants carry out overhauling of engines for early changes but are not responsible for inclusive repairs. They are only responsible for the proportional compensation of important parts damage owing to design and manufacturing during the guarantee period but the parts guarantee period is obviously less than their life. For example, the operation limit of a JT3D compressor disc can reach 20,000 hours yet the guarantee period is only 4,000 hours.

4. On-condition maintenance and condition monitoring must be used. The use of the mean TBO concept signifies that one half of the engines will reach the aforementioned requirement changes of the mean TBO. Thus, if there is a breakdown and the engine does not reach the designated time for changes, there will be midair stoppage or delayed error flight. The approximate relation can be indicated by the following formula:

$$IFSD \approx \frac{500}{\overline{H}} - PER \qquad (12)$$

In the formula, IFSD and PER separately represent the midair stoppage rate and early change rate. Thus it is necessary to use on-condition maintenance and the condition monitoring technique which is not dismantling and overhauling engines according to a stipulated time limit but monitoring the engine's important parameters as well as adopting appropriate measures to monitor the engine's key parts under undecomposed engine conditions and make on-condition changes of parts when necessary. As regards the stipulated total life and total rotational life of discs and axes, these techniques can promptly discover possible breakdowns and utilize early change to guarantee flight safety.

5. The expectation of the mean TBO. According to the statistical materials on navigation operations, over 50% of the engines exceed the stipulated TBO. The mean TBO can then be estimated by the following formulas:

$$\overline{H} = \frac{Z_1 H_2(R_2) - Z_2 H_1(R_1)}{Z_1 - Z_2} \qquad (13)$$

$$\sigma = \frac{H_1(R_1) - H_2(R_2)}{Z_1 - Z_2} \qquad (14)$$

In the formulas, Z_1 and Z_2 are based on the R_1 and R_2 numerical

values determined from formula (3).

The calculation results from formulas (13) and (14) are listed in table 4.

(1) H_1小时	R_1%	H_2小时 (2)	R_2%	Z_1	Z_2	$\bar{H}$小时 (3)	σ小时 (4)
1000	84.1	2000	30.85	-1.0	+0.5	1667	667
1000	84.1	2000	38.2	-1.0	+0.3	1769	769
1000	97.7	2000	84.1	-2.0	-1.0	3000	1000

Table 4 The Estimated Mean TBO According to Operating Statistical Information of Aeroengines

Key: 1. H_1 hours
2. H_2 hours
3. $\bar{H}$ hours
4. σ hours

To decrease estimation errors, the statistical engine numbers should be larger than 100 and generally R_1 should be greater than 0.5. At this time, the error variance of test statistical value R_1 is smaller than one-tenth of R_1. If there is statistical data for more than two points, we can then use the linear regression analysis method to estimate $\bar{H}$ and σ.

Aeroengines can also use the prolonged operating life method. For example, the United States Air Force operates twelve F100 engines. Their TBO is 500 hours, the continuous flight of two F100 engines exceeded 500 hours and TBO was extended to 750 hours [4]. Among the operational N engines, the operating life is lower than the TBO of the D. Among the spot checked n engines, the probability of m number of unqualified engines can be derived by the following formula:

$$P = \frac{C\left(\frac{D}{m}\right) C\left(\frac{N-D}{n-m}\right)}{C\left(\frac{N}{n}\right)} \qquad (15)$$

Table 5 gives the probabilities of continually having two engines exceeding 500 hours and based on the maximum estimated D-0～3 they can continuously have two engines exceeding 500 hours.

(1) 寿命小于 500小时的台数，D	0	1	2	3	4	5	6
(2) 使用寿命大于 500小时的百分数，R_k%	100	91.67	83.33	75	66.67	58.33	50
(3) 连续两台超过 500小时的概率，%	100	83.33	68.18	54.55	42.42	31.82	22.73
(4) 一台超过 500小时，一台小于 500小时的概率，%	0	16.67	30.30	40.91	48.48	53.03	54.55
(5) 两台均小于 500小时的概率，%	0	0	1.52	4.55	9.10	15.15	22.73

Table 5 The Probabilities of Two "Pacer Century" Engines' TBO Exceeding the Mean TBO in 12 Operational Aeroengines

Key: 1. Life is smaller than the number of engines of 500 hours

2. Percentage with operating life greater than 500 hours, R_k%

3. Probability of continuously having two engines exceed 500 hours, %

4. Probability of one engine exceeding 500 hours and one engine being less than 500 hours, %

5. The probability of both engines being less than 500 hours, %

Because point estimation error is relatively great, to be safe we take D=3 and if H(75)=500 hours from formula (2) we can obtain:

$$H(50)=H(R_k)-Z_k\sigma \qquad (16)$$

In the formula, Z_k is based on R_k which is derived from formula (3) and therefore H(50=H(75)=0.67450 so that the engine can prolong the life 0.6745 σ hours. If we take σ to be $\bar{H}/2.33$ which is 214.6 hours, we can prolong the life 145 hours. Therefore, using probability analysis we can continuously operate several engines in excess of the mean TBO and this can prolong the life. To guarantee flight safety, we should also carry out tests on key parts and test and verify acceleration simulated test runs in the manufacturing plant. We should use proper on-condition maintenance and condition monitoring measures in operations maintenance to guarantee operation reliability.

References

[1] Zhang Yimin, "Standards for Final Test Runs of Foreign Aircraft Turbojet (Including Turbofan) Engines," Foreign Aviation Technology, p.108, 1979.

[2] Irving W. Burr: Applied Statistical methods, Academic Press, 1974.

[3] J.R. Nelson: Life-Cycle Analysis of Aircraft Turbine Engine, AD A050349, Nov. 1977.p.108.

[4] F100 Allowable Operating Time Increased from 500 to 750 Hours, Power Plant, 1977.1.21.p.5

EXPERIMENTAL RESEARCH ON PERFORATED ACOUSTIC LINERS IN TURBOJET ENGINE AFTERBURNERS

by Ou Xuebin and Ni Guoxiong
(Shenyang Liming Machinery Company)

Abstract

The reasonable choice of construction parameters for perforated acoustic liners in turbojet engine afterburners was investigated from the engineer's point of view. The perforated acoustic liner should have as much as possible high oscillation absorptivity in a quite wide frequency range by increasing the volume of acoustic resonant space and the perforated area ratio of the shield. The smooth geometry of the liner can make the secondary flow uniform around the outer chamber shell and, therefore, avoid high temperature stripes proceeding from the gas separated-flow vortex at the wave valley on the perforated acoustic liner. Consequently, the circular temperature difference and the thermal stresses of the shell can be decreased, and the wall temperature of the afterburner shell can be kept down below the allowable temperature of its material. As a result, the afterburner can operate reliabily for a long time.

Table of Major Symbols

a	ripple height (millimeters)
b	ripple span (millimeters)
d	diameter of small holes for oscillation absorption (millimeters)
f_o	intrinsic frequency of perforated acoustic liner (hertz)
f	gas pulse frequency (hertz)
$\overline{G}_1$	ratio of secondary flow and total gas flow (percent)

h	height of wave valley (millimeters)
H	flight altitude (kilometers)
L	length of perforated acoustic liner (millimeters)
l	effective length (millimeters)
M	flight Mach number
n	number of small holes for oscillation absorption (each)
Δp	pulse pressure (kilograms/centimeter^2)
p	mean pressure of gas (kilograms/centimeter^2)
r	radius of ripple curvature (millimeters)
t	temperature (^oC) time (seconds
V	resonant space (meters^3)
x	length of afterburner shell (millimeters)
α	oscillation absorptivity
δ	thickness of perforated acoustic liner (millimeters)
σ	perforated area ratio (percent)
θ	acoustic resistance ratio
χ	acoustic reactance ratio

I. Preface

Following the raising of the afterburning ratio for turbojet aircraft, the oil-gas ratio in the afterburner continually increased thus causing the afterburner to produce a considerable enlargement of the pulse amplitude value. Moreover, the afterburner's shell wall temperature became increasingly higher When designing according to the acoustic resonance principle, when the perforated acoustic liner is placed in the main combustion area it can effectively inhibit and absorb oscillation energy. It especially guarantees smooth combustion in the greater part of the transverse high frequency range. The back part which does not have a heat insulation shield and the afterburner shell are directly exposed to the high temperature gas flow, and the construction of the perforated acoustic liner has a noticeable influence on the afterburner's shell wall temperature [1].

We installed various different types of perforated acoustic liners in similar locations in the same afterburner. This included comparative tests of the perforated acoustic liner oscillation damping temperature drop effects on a rippleless plate perforated acoustic liner carried out on ground rig, high altitude simulated test platforms and in flight. Fig. 1 is a schematic of the afterburner construction.

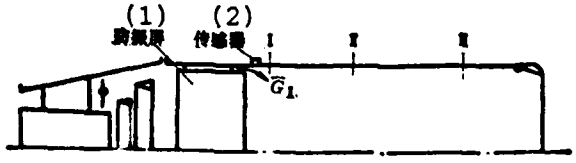

Fig. 1 Schematic of Afterburner Construction

Key: 1. Perforated acoustic liner
2. Transducer

II. Construction and Oscillation Absorptivity of Perforated Acoustic Liners

The construction parameters for different types of perforated acoustic liners are listed in table 1. See. fig. 2 for the construction schematic.

(1) 型别 \ (2) 量 \ (3) 参数	ρ (4)	b (5)	h (6)	L (7)	d (8)	n (9)	r (10)	V (11)	$\bar{G}_1$	δ (12)	σ
	毫米	毫米	毫米	毫米	毫米	个	毫米	米^3	%	毫米	%
I	20	86.7	7	378	5	540	25	1.56×10^{-2}	6.7	0.8	0.85
II	20	84.6	17	378	5	1080	25	2.55×10^{-2}	11.1	0.8	1.7
III	10	176	17	388	5	1320	178	2.32×10^{-2}	9.7	1	2.47

Table 1

Table I Construction Parameters For Different Types of Liners

Key: 1. Type
2. Dimension
3. Parameter
4. Millimeters
5. Millimeters
6. Millimeters
7. Millimeters
8. Millimeters
9. Each
10. Millimeters
11. Meters^3
12. Millimeters

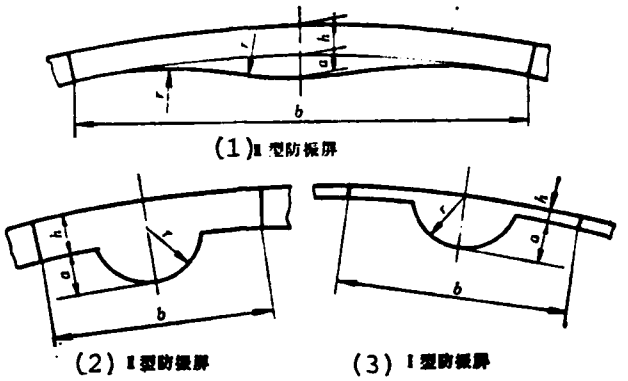

Fig. 2 Schematic of Perforated Acoustic Liners

Key: 1. Type III perforated acoustic liner
2. Type II perforated acoustic liner
3. Type I perforated acoustic liner

For perforated acoustic liners designed according to acoustic resonance principles, when gas pulse frequency f and intrinsic frequency f_o of acoustic resonant space in the combustion chamber both produce resonance, the acoustic reactance ratio is zero. At this time, the perforated acoustic liner's absorption gas oscillation energy is maximum, that is, the liner's oscillation absorptivity is maximum. When the gas pulse frequency deviates from the resonance point, oscillation absorptivity gradually diminishes. Fig. 3 gives the relational curve of oscillation absorptivity a and the gas pulse frequency of class I,II and III

perforated acoustic liners.

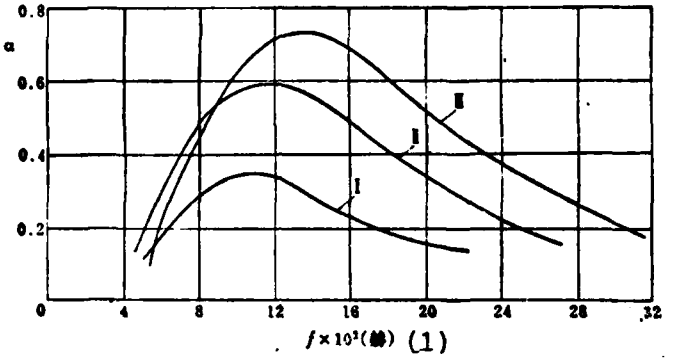

Fig. 3 Relational Curve of Oscillation Absorptivity a and Gas Pulse Frequency f

Key: 1. $fx10^2$ (hertz)

The curve is calculated by the following formula:

$$\alpha = \frac{4\theta}{(\theta+1)^2+\chi^2} \qquad (1)$$

In the formula, θ is the acoustic resistance ratio and x is the acoustic reactance ratio:

$$\theta = \frac{0.37u}{c_0\sigma c_1^2(1+1.9M_0)} \qquad (2)$$

$$\chi = \frac{2\pi l}{c_0\sigma} f_0\left(\frac{f}{f_0} - \frac{f_0}{f}\right) \qquad (3)$$

f_0 is the intrinsic frequency of the resonant space:

$$f_0 = \frac{c_0}{2\pi}\sqrt{\frac{\sigma}{Vl}} \qquad (4)$$

We carried out tests on the influences of the tested perforated area ratio on oscillation absorptivity on a ground rig using an A type engine. When the afterburning oil-gas ratio was $q_{j\Sigma}$ =0.057 ~ 0.060 and when we used type I perforated acoustic liners, the gas relative pulse pressure in the afterburner reached 52.6 percent. Moreover, when there was whistling and component damage, the perforated area ratio of the perforated acoustic liner increased from 0.85 percent to 1.7 percent, that is it doubled. Working under completely identical conditions, the relative pulse pressure amplitude value in the afterburner dropped by one half and the whistling disappeared. The measuring test results match the pattern revealed in formula (1).

Generally, the oscillation absorptivity of the turbojet engines is greater than the 0.2 frequency range and this can effectively inhibit and eliminate the occurence of oscillation combustion. We call this frequency range the effective oscillation absorption frequency band. The tests discussed below wherein there were the antivibration temperature drop effects of the perforated acoustic liners were carried out on a B type engine.

III. Test Results and Analysis

1. Tests on Antivibration Effects of Perforated Acoustic Liners

We used a pressure transducer to measure the gas pulse pressure on the shell wall behind the perforated acoustic liner (see fig. 1).

For the pulse pressure oscillograms of various types of flight conditions with total afterburning see figures 4-9 and for frequency spectrum analysis see fig. 10.

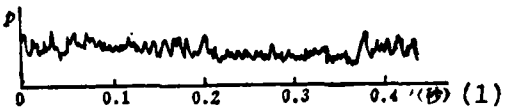

Fig. 4 Oscillogram of Gas Pulse Pressure in the Afterburner With Type I Liner
H=0, M=0, p=2.25 kilograms/centimeter^2, $\frac{\Delta p}{p}$ = 3.8 percent

Key: 1. (Seconds)

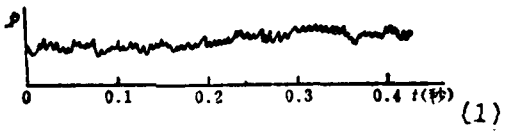

Fig. 5 Oscillogram of Gas Pulse Pressure in the Afterburner With Type II Liner
H=0, M=0, p=2.25 kilograms/centimeter^2, $\frac{\Delta p}{p}$ = 2.5 perent

Key: 1. (Seconds)

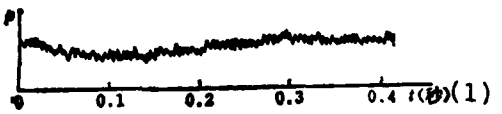

Fig. 6 Oscillogram of Gas Pulse Pressure In the Afterburner with Type III Liner
H=5, M=1.28, p. 2.81 kilograms/centimeter^2, $\frac{\Delta p}{p}$ = 3.7 percent

Key: 1. (Seconds)

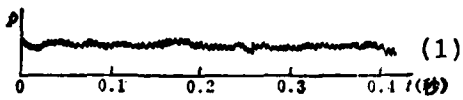

Fig. 7 Oscillogram of Gas Pulse Pressure In the Afterburner With Type III Lines

H=13.5, M=2.18, p=1.86 kilograms/centimeter^2, $\frac{\Delta p}{p}$ = 4.1 percent

Key: 1. (Seconds)

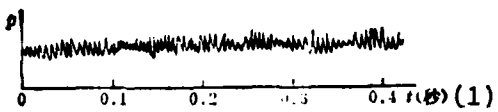

Fig. 8 Oscillogram of Gas Pulse Pressure In the Afterburner With Type III Liner

H=20, M=1.53, p=0.65 kilograms/centimeter^2, $\frac{\Delta p}{p}$ =6.5 percent

Key: 1. (Seconds)

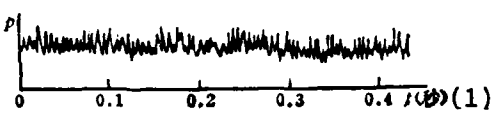

Fig. 9 Oscillogram of Gas Pulse Pressure In the Afterburner With Type I Liner

H=20, M=1.6, p=0.65 kilograms/centimeter^2, $\frac{\Delta p}{p}$ =6.5 percent

Key: 1. (Seconds)

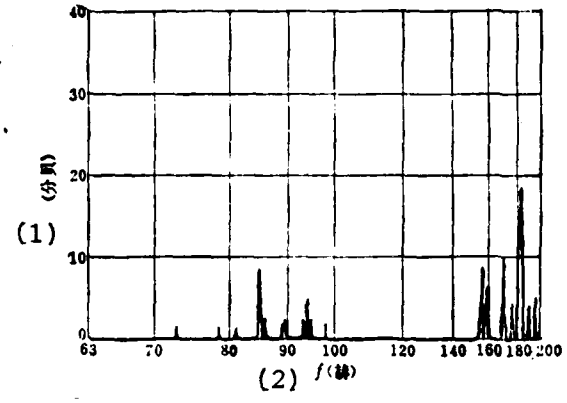

Fig. 10 Frequency Spectrum of Gas Pulse Pressure In the Afterburner With Type III Liner

H=20, M=1.6

Key: 1. (Decibels)
2. (hertz)

2. Analysis of Results of Antivibration Tests

Perforated acoustic liners with designs based on the acoustic resonance principle can inhibit or eliminate pressure oscillation in the afterburner, especially in the high frequency oscillation range. Test results show that:

(1) Gas pressure oscillation in the afterburner changes with flight conditions, and following the gas mean pressure drop in the afterburner there is a corresponding increase of the pulse pressure value.

(2) The increases of the liner's acoustic resonant space and perforated area ratio raised the liner's absorption, storage

and dissipation of oscillation energy and thus raised the oscillation absorption effects of the perforated acoustic liner.

(3) The perforated acoustic linear used a rippled plate construction which caused obstruction of pressure wave propagation and destroyed the resonant effects in the combustion chamber. Thus, there was an antivibration effect. The circular ripple construction helped to inhibit transverse oscillation yet the resonant space and perforated area ratio were close. Among the perforated acoustic liners with very different geometrical shapes there were not noticeable differences in antivibration effects. This shows that the geometric shape of the liner has a secondary influence on total antivibration effects.

(4) The antivibration effects of liners designed according to the acoustic resonance principle and which are perforated, on low frequency oscillation is lacking. By increasing the resonant space we can lower resonant space intrinsic frequency f_o. Yet an excessive enlargement of the resonant space causes the working condition speed in the liner's deep center high temperature gas flow to worsen, for example the type I perforated acoustic liner.

3. Tests of Afterburner's Shell Wall Temperature

There are 12 measured temperature points on the wall surface of the afterburner shell I, II and III sections to measure the afterburning wall temperature (see fig. 1).

See figures 11 and 12 for the section's mean wall temperature changes along the axis of the afterburner and the peripheral distribution of the wall temperatures in section III.

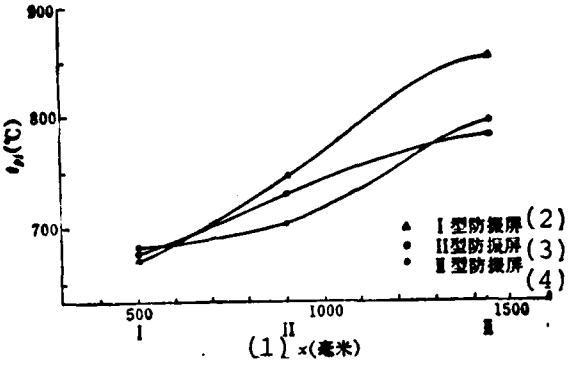

Fig. 11 Variation Curve of Mean Shell Temperatures Along Axis

Key: 1. x (millimeters)
2. Type I perforated acoustic liner
3. Type II perforated acoustic liner
4. Type III perforated acoustic liner

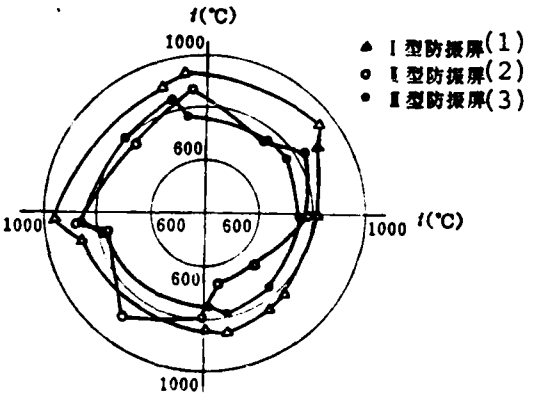

Fig. 12 Peripheral Distribution of Wall Temperatures in Section III

Key: 1. Type I perforated acoustic liner
2. Type II perforated acoustic liner
3. Type III perforated acoustic liner

The test results of measured temperatures show that:

(1) The enlargement of the secondary flow of the perforated acoustic liner and in the shell crevice can cause the highest mean wall temperature of the shell to drop. The wall temperature of the shell's section III with a type III perforated acoustic liner drops about 70°C lower than the shell with type I perforated acoustic liner. Its axial temperature rise gradient drops from 180-200°C/meter to 110-130°C meter.

(2) A uniform secondary flow peripheral distribution in the crevice can cause the shell's peripheral temperature difference to noticeably drop and the peripheral temperature difference of the shell's section III with a type III perforated acoustic liner drops 107°C lower than the shell with a type I perforated acoustic liner.

(3) The above two factors cause the highest thermal point temperature to noticeably drop. The highest thermal point temperature of section III with a type I perforated acoustic liner reaches 950°C and the temperature points above 900°C occupy one half of the section. However, when the highest temperature with a type III perforated acoustic liner is only 860°C, there is a drop of 90°C.

(4) Analysis of Wall Temperature Test Results

Test results show that the geometric shape and measurement of the perforated acoustic liner has a noticeable influence on the afterburner's shell wall temperature.

(1) The enlarging of the secondary flow of the perforated acoustic liner and shell crevice increased the cooling effect of the low temperature secondary flow on the shell's wall surface.

(2) When the liner's ripple geometric shape was made smooth, this caused the secondary flow distribution along the periphery to be uniform which effectively weakened the high temperature stripes produced from the backward stretching concave slot vortex at the wave valley exit on the perforated acoustic liner.

(3) The increase of the secondary flow in the crevice decreased the amount of air of the main combustion area near the perforated acoustic liner. This caused the gas air mixture ratio near the perforated acoustic liner to increase, changed the optimum chemical equivalent ratio during combustion, raised combustion efficiency in that area, weakened the combustion elongated segment due to the compensation combustion of the uncombusted oil, and caused the elongated segment wall temperature to rise slowly.

IV. Preliminary Conclusions

The antivibration effects of perforated acoustic liners mainly determined by the size and perforated area ratio of the resonant space and oscillation absorptivity small holes in the perforated acoustic liner and afterburner shell. The perforated acoustic liner's lowered effects on the afterburner shell are not only determined by the size of the perforated acoustic liner and shell crevice but are also determined to a large extent by the uniformity of the crevice along the periphery. This shows that the geometric shape of the perforated acoustic liner is only a relatively secondary factor for antivibration but it has a noticeable influence on afterburner shell wall temperature.

References

[1] The Number 5 Laboratory of the Institute of Mechanics of the Academia Sinica, "The Design Principle of Perforated Acoustic Liners."

[2] The Aviation Academy of Nanjing, "Principles of Afterburners," 1977.

A TIME INVARIANT STATE ESTIMATOR FOR CONTINUOUS TIME SYSTEMS

by Dai Guanzhong
(Northwestern Polytechnical University)

Abstract

This paper studies the design method of the steady state estimator for linear steady and continuous time systems when the system and measured noise is a smooth white noise process. To improve the transient performance of the traditional Kalman-Bucy filter definitions of two new performance functions are proposed, thus giving two modified Kalman-Bucy filters which can be conveniently applied in engineering.

I. Preface

It is well know that there exists a basic contradiction between transient state and steady state requirements. The traditional Kalman-Bucy filter has "narrow frequency band" problems, that is, there can be an effectively filtered Kalman-Bucy filter for the random noise which is often a relatively remarkable system of dynamic hysteresis [1-4].

When applied in engineering, the transient state and steady state performances of the state estimator must be excellent and one cannot be attended to while losing sight of the other. This is especially the case for state estimators operating for short periods of time where transient performance is very important.

To improve the transient performance of the traditional Kalman-Bucy filter, this paper proposes considering the

requirements of the filter's steady state estimated error and also defines two new performance functions required for its transient performance. In this way, the paper gives the design methods of two modified Kalman-Bucy filters which can be conveniently applied in engineering.

II. System and Filter

The estimated linear steady and continuous time system S is described by the following equations:

$$\dot{x}(t)=Ax(t)+Bu(t)+\Gamma w(t),\quad x(0)=x_0 \tag{1}$$

$$y(t)=Cx(t)+v(t) \tag{2}$$

In the equations, state $x\in R^n$, control $u\in R^r$, output $y\in R^m$, system noise $w\in R^l$, measuring noise $v\in R^m$; A, B, C and Γ are separately the state matrix, control input matrix, output matrix and noise imput matrix of (n,n), (n,r), (m,n) and (n,1).

If control $\{u(t)\}$ is the determined input, and if $\{w(t)\}$ and $\{v(t)\}$ are zero mean values, the mutually exclusive smooth white noise process is:

$$Ew(t)=0,\ Ew(t)w'(\tau)=Q\delta(t-\tau)\quad (Q\geqslant 0) \tag{3}$$

$$Ev(t)=0,\ Ev(t)v'(\tau)=R\delta(t-\tau)\quad (R>0) \tag{4}$$

$$Ew(t)v'(\tau)=0 \tag{5}$$

Further, if initial state x_o is an uncorrelated random vector with $\{w(t)\}$ and $\{v(t)\}$:

$$Ex_0 w'(t) = 0, \quad Ex_0 v'(t) = 0 \tag{6}$$

We know that its mean value and variance matrix are:

$$Ex_0 = \bar{x}_0, \quad E(x_0 - \bar{x}_0)(x_0 - \bar{x}_0)' = P_0 \quad (P_0 \geqslant 0) \tag{7}$$

To guarantee the asymptotic characteristic requirements of the filter, we also assume:

(A,C) is a measureable pair $\left(A, \Gamma Q^{\frac{1}{2}}\right)$ is a controllable pair (8)

Here, $Q^{\frac{1}{2}}$ is the square root of the non-negative system's noise variance matrix Q, that is: for $Q \geqslant 0$, an existing symmetrical matrix $M \geqslant 0$ causes $Q=MM'M^2$, noting $M=Q^{\frac{1}{2}}$.

Because of the corresponding relation of the primitive form and model existing within the estimated system and its state estimator [5], we can assume that the equation of the steady state estimator (filter) S_E is:

$$\dot{z}(t) = Fz(t) + Lu(t) + Gy(t), \quad z(0) = z_0 \tag{9}$$

$$\hat{x}(t) = Hz(t) \tag{10}$$

In the formulas, the filter's state $z \in R^p$, the filter's output $\hat{x} \in R^n$, which is an estimation of state x; F, G, L and H are separately the filter's feedback matrix, forward matrix, control input matrix and output matrix of (p,p), (p,m), (p,r) and (n,p).

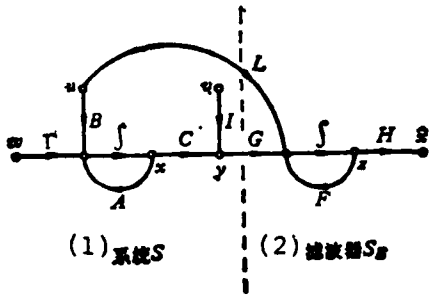

Fig. 1 System and Filter

Key: 1. System S
2. Filter S_E

To sum up, the design of filter S_E is the determination of its dimension p, initial value z_o as well as the F,G,L and H matrices.

It is only necessary to accord with the following state estimation requirements:

(1) Unbiasedness, that is

$$E\hat{x}(t)=Ex(t), \text{ 或}^{(1)} E\tilde{x}(t)=0 \tag{11}$$

Key: 1. Or

(2) Minimum variance, that is

$$t_rP(t)=t_rE\tilde{x}(t)\tilde{x}'(t)=\min \tag{12}$$

In the formulas, $P(t) \triangleq E\tilde{x}(t)\tilde{x}'(t)$ is the estimation error.

(3) Transient performance requirements, that is the matching requirements of the characteristic value $\lambda_i(F)(i=1,2...,p)$ for F.

Usually, there is a contradiction between requirements (2) and (3) and it is necessary, based on the different uses, to lay stress on a certain aspect from the different performance functions.

III. Unbiasedness

From the requirements of unbiasedness, we can determine dimension p, initial value z_o of S_E as well as the relation between the F, G, L and H matrices.

Firstly, when the initial time t=0, then from the unbiasedness requirements

$$E\hat{x}_o = Ex_o = \bar{x}_o$$

Because the initial estimation $\hat{x}_o$ is a nonrandom quantity, therefore

$$\hat{x}_o = \bar{x}_o \tag{13}$$

On the other hand, the initial state z_o of S_E from formula (10) should satisfy:

$$Hz_o = \hat{x}_o = \bar{x}_o$$

In order for there to be only one solution of z_o for an arbitrary $\bar{x}_o$, it is then required that:

$H \in R^{nxn}$ (i.e., p=n) and the H matrix is non-singular (14)

Thus, formulas (9) and (10) can be changed into

$$\frac{d}{dt}\hat{x}(t) = HFH^{-1}\hat{x}(t) + HLu(t) + HGy(t),\ \hat{x}_0 = \bar{x}_0 \tag{15}$$

When comparing formulas (1) and (15), in order to cause the influence of the estimated system S and state estimator S_E on the determined control u(t) to be the same, we should take

$$HL = B \tag{16}$$

Because of this, from the t=0 transient unbiasedness requirements, the S_E equation is then

$$\frac{d}{dt}\hat{x}(t)=HFH^{-1}\hat{x}(t)+Bu(t)+HGy(t),\ \hat{x}_0=\bar{x}_0 \qquad (17)$$

Secondly, based on the unbiasedness requirements, when $t > 0$, we further determine the relation between the F,H and G matrices in formula (17). We can obtain from formulas (1), (2) and (17)

$$\begin{aligned}\frac{d}{dt}\tilde{x}(t)&=Ax(t)+\Gamma w(t)-HFH^{-1}\hat{x}(t)-HG[Cx(t)+v(t)]\\&=(A-HFH^{-1}-HGC)x(t)+HFH^{-1}\tilde{x}(t)+\Gamma w(t)-HGv(t)\end{aligned} \qquad (18)$$

From the unbiasedness requirements: $E\tilde{x}(t)=0$, and therefore $\frac{d}{dt}E\tilde{x}(t)=E\left[\frac{d}{dt}\tilde{x}(t)\right]=0$; further paying attention that the mean values of $\{w(t)\}$ and $\{v(t)\}$ are zero, we obtain from formula (18)

$$(A-HFH^{-1}-HGC)Ex(t)=0 \qquad (19)$$

On the other hand, from formulas (1) and (3) we can obtain

$$\frac{d}{dt}Ex(t)=AEx(t)+Bu(t),\ Ex_0=\bar{x}_0$$

Its solution is

$$Ex(t)=e^{At}\bar{x}_0+\int_0^t e^{A(t-\tau)}Bu(\tau)d\tau$$

Generally, $Ex(t) \neq 0$, yet formula (19) is always established for $t > 0$ and thus

$$A-HFH^{-1}-HGC=0$$

For this reason, from the unbiasedness requirements of $t > 0$, we can obtain the relation between the F, H and G matrices of S_E

$$HFH^{-1}=A-HGC \tag{20}$$

If formula (20) is substituted into formula (17), we can obtain

$$\frac{d}{dt}\hat{x}(t)=A\hat{x}(t)+Bu(t)+HG[y(t)-C\hat{x}(\cdot)],\ \hat{x}_0=\bar{x}_0$$

Forward matrix G and output matrix H are joined into a new forward gain matrix:

$$K=HG \tag{21}$$

Then, we can obtain the S_E equation

$$\frac{d}{dt}\hat{x}(t)=A\hat{x}(t)+Bu(t)+K[y(t)-C\hat{x}(t)],\ \hat{x}_0=\bar{x}_0 \tag{22}$$

This type of state estimator is unbiased and is called the unbiased filter. Fig. 2 shows the signal flow chart of estimated system S and unbiased filter S_E.

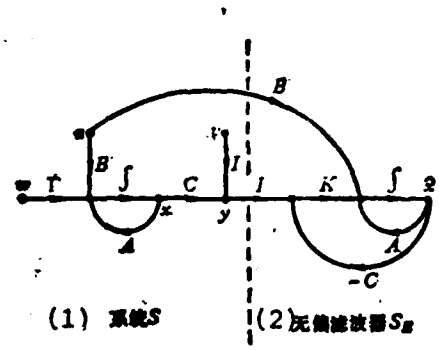

Fig. 2

Fig. 2 System and Unbiased Filter

Key: 1. System S
2. Unbiased filter S_E

IV. Asymptotic Characteristics

We know from the above discussion that for the design of filter S_E the remaining requirements of (2) and (3) mentioned previously are used to determine the forward gain matrix K. This section first studies the asymptotic characteristics of filter S_E and takes the determining of the K matrix as preparation.

When the unbiased filter conditions of formulas (20) and (21) are substituted into formula (18), we can obtain an equation for estimation error:

$$\frac{d}{dt}\tilde{x}(t)=(A-KC)\tilde{x}(t)+\Gamma w(t)-Kv(t),\ \tilde{x}_0=x_0-\bar{x}_0 \qquad (23)$$

Its solution is

$$\tilde{x}(t)=e^{(A-KC)t}\tilde{x}_0+\int_0^t e^{(A-KC)\tau}[\Gamma w(t-\tau)-Kv(t-\tau)]d\tau \qquad (24)$$

When we give attention to formulas (3)-(7), we can obtain a variance matrix for the estimation error

$$P(t)=e^{(A-KC)t}P_0e^{(A-KC)'t}+\int_0^t e^{(A-KC)\tau}(\Gamma Q\Gamma'+KRK')e^{(A-KC)'\tau}d\tau \qquad (25)$$

Now we will study the asymptotic situation of $t\to\infty$. When $t\to\infty$ in formula (25), if A-KC is a steady matrix then the steady estimation error variance matrix is

$$P \triangleq \lim_{t\to\infty} P(t) = \int_0^\infty e^{(A-KC)t}(\Gamma Q\Gamma' + KRK')e^{(A-KC)'t}dt \qquad (26)$$

[Lemma 1] If A-KC is a steady matrix and $(A, \Gamma Q^{\frac{1}{2}})$ is a controllable pair, then the P convergent of formula (25) is positive determine solved by the following Lyapunov equation:

$$P(A-KC)' + (A-KC)P + (\Gamma Q\Gamma' + KRK') = 0 \qquad (27)$$

Proof: from formula (26) we can obtain

$$P(A-KC)' = \int_0^\infty e^{(A-KC)t}(\Gamma Q\Gamma' + KRK')de^{(A-KC)'t}$$

Based on partial integration, we obtain

$$P(A-KC)' = [e^{(A-KC)t}(\Gamma Q\Gamma' + KRK')e^{(A-KC)'t}]_0^\infty - (A-KC)\int_0^\infty e^{(A-KC)t}(\Gamma Q\Gamma' + KRK')e^{(A-KC)'t}dt$$

Taking notice that A-KC is a steady matrix, then from the above formula we know that P satisfies formula (27).

Next, we study the homogeneous system $\dot{\eta}(t) = (A-KC)'\eta(t)$ and take

$$V(\eta) = \eta' P\eta$$

Then

$$\dot{V}(\eta) = \dot{\eta}'P\eta + \eta'P\dot{\eta} = \eta'[(A-KC)P + P(A-KC)']\eta$$
$$= -\eta'(\Gamma Q\Gamma' + KRK')\eta \leqslant 0$$

Because A-KC is a steady matrix, based on the Lyapunov steady theorem [6]: if the arbitrary non zero h R^n, and the $V(\eta) \not\equiv 0$ along the solution locus $\eta(t)=e^{(A-KC)'t}h'$ then $V(\eta)$ is the Lyapunov function and $P>0$. In reality, if

$$\dot{V}(\eta)=-\eta'(\Gamma Q\Gamma'+KRK')\eta\equiv 0$$

then

$$\eta'\Gamma Q\Gamma'\eta\equiv 0,\ \eta'KRK'\eta\equiv 0$$

Because $R>0$, therefore $K'\eta\equiv 0$ and also $K=0$. Thus,

$$\eta'\Gamma Q\Gamma'\eta = h'e^{At}\Gamma Q^{\frac{1}{2}}(\Gamma Q^{\frac{1}{2}})'e^{A't}{}_{h=0}$$
(for all the $t>0$)

This is a controllable relative contradiction with $(A, \Gamma Q^{\frac{1}{2}})$. The lemma proof is completed.

V. Minimum Variance

In view of the steady performance when the traditional steady state Kalman-Bucy filter mainly operates in a $t\to\infty$ steady state, the performance function is taken as

$$J=tr P=tr\int_0^\infty e^{(A-KC)'t}(\Gamma Q\Gamma'+KRK')e^{(A-KC)'t}dt \qquad (28)$$

[Theorem] As regards system S, if (A,C) is a measurable pair and when $(A, \Gamma Q^{\frac{1}{2}})$ is a controllable pair, this causes the performance function of formula (28) to be minimal and the optimal gain matrix K of filter S_E is

$$K=PC'R^{-1} \qquad (29)$$

In the formula, P is the positive definite solution of the following Riccati substitution equation:

$$AP+PA'-PC'R^{-1}CP+\Gamma Q\Gamma'=0 \qquad (30)$$

Moreover, matrix A-KC is a steady matrix.

Proof: see reference [7].

Formulas (29) and (30) are commonly called the substitution conditions of the steady state Kalman-Bucy filter S_E. To further study the transient performance of S_E, we can study the form of the above mentioned substitution conditions in the frequency domain. We have:

[Theorem 2] The frequency domain of the steady state Kalman-Bucy filter S_E is

$$\begin{aligned}&|I+R^{-1/2}C(j\omega I-A)^{-1}KR^{1/2}|^2\\&\quad=I+R^{-1/2}C(j\omega I-A)^{-1}(\Gamma Q\Gamma')(-j\omega I-A')^{-1}C'R^{-1/2}\end{aligned} \qquad (31)$$

Here, $R^{\frac{1}{2}}$ is the square root of the positive definite noise variance matrix R, that is: when $R>0$ and there is a symmetrical matrix $N>0$, $R=NN'=N^2$, noting $N=R^{\frac{1}{2}}$.

Proof: these are also well known results and the proof can be seen in reference [8].

In particular, when estimated system S is a single output (m=1) system, then the frequency domain conditions of formula (31) in the steady state Kalman-Bucy filter S_E changes to

$$|1+c'(j\omega I-A)^{-1}k|^2=1+\frac{1}{r^2}c'(j\omega I-A)^{-1}(\Gamma Q\Gamma')(-j\omega I-A')^{-1}c \qquad (32)$$

In the formula, S's output matrix $c' \in R^{1xn}$. the measured noise's variance $R=r^2$ (scalar quantity), and S_E's optimal gain matrix $k \in R^{nx1}$.

We know form fig. 2 that $G(s)=c'(sI-A)^{-1}k$ is the open loop transfer function of filter S_E and therefore the frequency domain conditions of formula (32) changed to

$$|1+G(j\omega)|^2=1+\frac{1}{r^2}c'(j\omega I-A)^{-1}(\Gamma Q\Gamma')(-j\omega I-A')^{-1}c \qquad (33)$$

that is

$$|1+G(j\omega)|\geq 1 \qquad (34)$$

This signifies that the distance between the open loop Nyquist curve $G(j\omega)$ of the steady state Kalman-Bucy filter and (-1,j0) point on the complex plane is not smaller than 1. In other words, $G(j\omega)$ cannot be advanced into the unit circle taking the (-1,j0) as the center of the circle (see fig. 3).

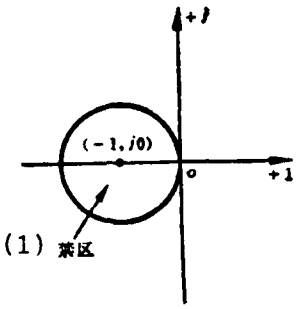

Fig. 3 Restricted Zone of $G(j\omega)$

Key: 1. Restricted zone

It is easily known that the phase capacity of filter S_E is not less than 60° and the gain capacity is unlimited [8].

Although the steady state Kalman-Bucy filter S_E has relatively good asymptotic steady characteristics yet its transient performance is not good enough. In reality, S_E is only a "narrow frequency band" low pass filter.

VI. One Method For Improving Transient Performance

We define the new performance function as

$$J_\alpha = t_r P_\alpha = t_r \int_0^\infty e^{2\alpha t}\left[e^{(A-KC)t}(\Gamma Q \Gamma' + KRK')e^{(A-KC)'t}\right]dt \qquad (35)$$

In the formula, $\alpha > 0$, and the dimension is $\sec^{-1}$. Formula (35) can be changed to

$$J_\alpha = t_0 P_\alpha = t_0 \int_0^\infty e^{(A+\alpha I-KC)t}(\Gamma Q \Gamma' + KRK')e^{(A+\alpha I-KC)'t}dt \qquad (36)$$

In formula (36), the state matrix is already changed to A+aI and the remainder are the same as performance function (28).

[Lemma 2] $(A+\alpha I, C)$ is the measureable pair but only (A,C) acts as the measureable pair, and $(A+\alpha I, \Gamma Q^{\frac{1}{2}})$ is the controllable pair but only $(A, \Gamma Q^{\frac{1}{2}})$ acts as the controllable pair.

Proof: take note that the measureable matrix is

$$R_0 = \begin{bmatrix} C \\ CA \\ \vdots \\ CA^{n-1} \end{bmatrix}, \quad R_{0\alpha} = \begin{bmatrix} C \\ C(A+\alpha I) \\ \vdots \\ C(A+\alpha I)^{n-1} \end{bmatrix}$$

In the formulas

$$C(A+\alpha I) = CA + \alpha C$$
$$C(A+\alpha I)^2 = CA^2 + 2\alpha CA + \alpha^2 C$$
$$\vdots$$

Because after the constant of a certain line multiplies to another line the rank of the matrix is unchanged, therefore

$$\text{rank } R_0 = \text{rank } R_{0\alpha}$$

Proof for the front half of the lemma is completed.

For the back half of the lemma we can use the duality

principle proof of controllability and measureability. Actually, from the duality principle, $(A, \Gamma Q^{\frac{1}{2}})$ is a controllable pair and $(A', Q^{\frac{1}{2}}\Gamma')$ is a measureable pair; from the front half of this lemma, $[(A+\alpha I)', Q^{\frac{1}{2}}\Gamma']$ is a measureable pair and $(A+\alpha I, \Gamma Q^{\frac{1}{2}})$ is a controllable pair. The lemma proof is completed.

After attaining lemma 2, the entire results in sections IV and V can be copied.

Firstly, based on lemma 1, if $A+\alpha I-KC$ is a steady matrix then the P convergence in formula (36) is positive definite solved by the following Lyapunov equation:

$$P_*(A+\alpha I-KC)'+(A+\alpha I-KC)P+(\Gamma Q\Gamma'+KRK')=0 \qquad (37)$$

Secondly, based on theorem 1, we can cause formula (36) which is the smallest optimal gain matrix K_* to be

$$K_*=P_*C'R^{-1} \qquad (38)$$

In the formula, P_* is the positive definite solution of the following Riccati substitution equation:

$$(A+\alpha I)P_*+P_*(A+\alpha I)'-P_*C'R^{-1}CP_*+\Gamma Q\Gamma'=0 \qquad (39)$$

Moreover, matrix $A+\alpha I-K_*C$ is a steady matrix.

To sum up, we then have the following theorem:

[Theorem 3] For system S, if (A,C) is a measureable pair and $(A, \Gamma Q^{\frac{1}{2}})$ is a controllable pair, then the optimal gain matrix K_* of the modified steady state Kalman-Bucy filter S_* satisfies formulas (38) and (39).

We will now analyze the transient performance of the modified Kalman-Bucy filter S_*.

[Theorem 4] The distance of the characteristic value distribution of the modified Kalman-Bucy filter S_* in the left half of the complex plane and of the imaginary distance axis is larger than α_*.

Proof: because matrix $A+\alpha I-K_*C$ is a steady matrix, its characteristic value is distributed in the left side of the complex plane. On the other hand, the corresponding characteristic values of matrix $A-K_*C$ characteristic value relative matrix $A+\alpha I-K_*C$ shift a distance of a to the left. Thus, this theorem is completed.

We saw that the attenuation of filter S_* is greater than α, in other words, the time constant of the major extreme point of S_* is smaller than $1/\alpha_*$.

We will now further compare the transient performances of Kalman-Bucy filter S_E and modified Kalman-Bucy filter S_*. For this reason, it is the same as theorem 2 and thus we have:

[Theorem 5] The frequency domain conditions of modified steady state Kalman-Bucy filter S_* is

$$|I + R^{-1/2}C(j\omega I - A)^{-1}K_*R^{1/2}|^2 = I + R^{-1/2}C(j\omega I - A)^{-1}(\Gamma Q\Gamma' + 2\alpha P_*)(-j\omega I - A')^{-1}C' R^{-1/2} \quad (40)$$

Proof: We use the Riccati substitution equation to rewrite formula (39) as

$$AP_* + P_*A' - P_*C' R^{-1}CP_* + (\Gamma Q\Gamma' + 2\alpha P_*) = 0 \quad (41)$$

Further imitating theorem 2 we can immediately prove that the frequency domain conditions of S_a are formula (40).

When estimated system S is a single output system, the S_* frequency domain conditions of (40) change to

$$|1 + c'(j\omega I - A)^{-1}k_*|^2 = 1 + \frac{1}{r^2}c'(j\omega I - A)^{-1}(\Gamma Q\Gamma' + 2\alpha P_*)(-j\omega I - A')^{-1}c \quad (42)$$

If $G_*(s) = c'(sI - A)^{-1}k_*$ is the open loop transfer function of filter S_* and we also take into account formula (33), then formula (42) can be rewritten as

$$|1 + G_*(j\omega)|^2 = |1 + G(j\omega)|^2 + \frac{2\alpha}{r^2}c'(j\omega I - A)^{-1}P_*(-j\omega I - A')^{-1}c$$

Because $\alpha > 0$ and P_* are positive definite, therefore aside from the ω values, there is

$$|1 + G_*(j\omega)| > |1 + G(j\omega)| \quad (43)$$

This signifies that the open loop Nyquist curve $G_*(j\omega)$ of S_* is further from the (-1,j0) point on the complex plane than the open loop Nyquist curve $G(j\omega)$ of S_E. It is commonly known that generally speaking the open loop Nyquist curve of the unit feedback system is further from the (-1,j0) point and its close loop major extreme point is further from the imaginary axis. Therefore, the modified steady state Kalman-Bucy filter S_* raised transient performance.

VII. Second Method For Improving Transient Performance

Formula (25) gave the changes of the estimation error variance matrix. The first item is the transfer of the estimation error caused by the initial estimation error variance matrix P_0, and the second item is the accumulation of the estimation error variance matrix produced by system noise $\{w(t)\}$ and measured noise $\{v(t)\}$. The transient performance of the filter can be determined by the attenuation speed of the initial estimation error variance matrix. For this reason, we defined another new performance function

$$J_\beta = t_r P_\beta = t_r\left\{\int_0^\infty e^{(A-KC)t}(\Gamma Q\Gamma' + KRK')e^{(A-KC)'t}dt + \beta\int_0^\infty e^{(A-KC)'t}P_1 e^{(A-KC)'t}dt\right\} \tag{44}$$

In the formula, $\beta > 0$. Here, the first item is the accumulated steady state estimation error variance matrix produced by the system noise and measured noise. It delineated the steady state precision of the filter. The second item represents the total accumulation effect produced by the initial estimation error variance matrix. It delineates the transient performance of the filter in a fixed range. β is then the weight coefficient between the steady state precision requirements and transient performance requirements. Therefore, P_β can be called the comprehensive steady state estimation error variance matrix.

Formula (44) can be rewritten as

$$J_\beta = t_r P_\beta = t_r \int_0^\infty e^{(A-KC)t}(\beta P_0 + \Gamma Q \Gamma' + KRK')e^{(A-KC)'t}\,dt \qquad (45)$$

In the formula, the non-negative $\beta P_0 + \Gamma Q \Gamma'$ can be decomposed into: $\beta P_0 = \Gamma Q \Gamma' = M^2$, and M is the non-negative symmetrical matrix.

Therefore, we can have:

[Lemma 3] If $(A, \Gamma Q^{\frac{1}{2}})$ is a controllable pair then (A,M) must be a controllable pair.

Proof: If $(A, \Gamma Q^{\frac{1}{2}})$ is a controllable pair, then it must exist in $T < \infty$ causing

$$\int_0^T e^{At}\Gamma Q^{1/2}\,(\Gamma Q^{1/2})' e^{A't}\,dt = \int_0^T e^{At}\Gamma Q \Gamma' e^{A't}\,dt > 0$$

Further, because $\beta > 0$, the P_0 matrix is non-negative and therefore

$$\int_0^T e^{At} MM' e^{A't}\,dt = \int_0^T e^{At}(\beta P_0 + \Gamma Q \Gamma')\, e^{A't}\,dt$$

$$= \int_0^T e^{At}\Gamma Q \Gamma' e^{A't}\,dt + \beta \int_0^T e^{t} P_0 e^{A't}\,dt > 0$$

This proves that (A,M) is a controllable pair.

After obtaining lemma 3 the entire results of sections IV and V can be copied.

Firstly, based on lemma 1, if A-KC is a steady matrix then the P_β congruence in formula (45) can be positive definite

solved by the following Lyapunov equation:

$$P_\beta(A-KC)'+(A-KC)P_\beta+(\beta P_0+\Gamma Q\Gamma'+KRK')=0 \qquad (46)$$

Secondly, we also have:

[Theorem 6] For system S, if (A,C) is a measureable pair, when $(A, \Gamma Q^{\frac{1}{2}})$ is a controllable pair then the performance function of formula (45) is minimal and the optimal gain matrix K_β of the modified steady state Kalman-Bucy filter S_β is

$$K_\beta=P_\beta C' R^{-1} \qquad (47)$$

In the formula, P_β is the positive definite solution of the following Riccati substitution equation:

$$AP_\beta+P_\beta A'-P_\beta C' R^{-1}CP_\beta+(\beta P_0+\Gamma Q\Gamma')=0 \qquad (48)$$

Moreover, matrix $A-K_\beta C$ is a steady matrix. The frequency domain condition of S_β is

$$|I+R^{-1/2}C(j\omega I-A)^{-1}K_\beta R^{1/2}|^2=I+R^{-1/2}C(j\omega I-A)^{-1}(\beta P_0+\Gamma Q\Gamma')(-j\omega I-A)^{-1}C'R^{-1/2} \qquad (49)$$

Proof: proof obtained from theorems 1 and 2.

To compare the traditional Kalman-Bucy filter S_E with $\beta=0$ and the transient performance of the modified Kalman-Bucy filter S_β with $\beta>0$, we studied the situation wherein estimated S was a single output system. At this time, the filter S_β frequency domain conditions of formula (49) changed to

$$|1+c'(j\omega I-A)^{-1}k_\beta|^2=1+\frac{1}{r^2}c'(j\omega I-A)^{-1}(\beta P_0+\Gamma Q\Gamma')(-j\omega I-A')^{-1}c \quad (50)$$

If $G_\beta(s)=c'(sI-A)^{-1}k_\beta$ is the open loop transfer function of filter S_β and we consider formula (33), then formula (50) can be rewritten as

$$|1+G_\beta(j\omega)|^2=|1+G(j\omega)|^2+\frac{\beta}{r^2}c'(j\omega I-A)^{-1}P_0(-j\omega I-A')^{-1}c$$

Because $\beta>0$ and P_0 are non-negative, therefore

$$|1+G_\beta(j\omega)|\geq|1+G(j\omega)| \quad (51)$$

This signifies that the open loop Nyquist curve $G_\beta(j\omega)$ of S_β is further from the (-1,j0) point on the complex plane than the open loop Nyquist curve $G(j\omega)$ of S_E. Therefore, the modified steady state Kalman-Bucy filter S_β raised transient performance.

VIII. Conclusion

Based on the different requirements for application in engineering, the designs for the steady state estimator for continuous time systems can be carried out in three cases:

(1) Transient design in view of the transient performance. This is the design problem of a state observer;

(2) Steady state design in view of steady state precision. This is the design problem of the traditional Kalman-Bucy filter;

(3) When considering the steady state and transient state synthetic design with steady state precision and transient performance, this paper proposed design methods for two types of modified Kalman-Bucy filters.

References

[1] Kalman, R.E., "A New Approach to Linear Filtering and Prediction Problems",J Basic Eng., Trans. ASME, Series D, Vol.82, No.1, 1960,pp.35-45.

[2] Kalman, R.E., and Bucy, R.S., "New Results in Linear Filtering and Prediction Theory", J. Basic Eng. Trans. ASME, Series D, Vol 83, No. 3, 1961, pp.95-108.

[3] Anderson, B.D.O., and Moore, J.B., "Optimal Filtering", Prentice-Hall, INC., 1979.

[4] "Mathematical Methods For Discrete Time System Filtering", Probability Group of the Mathematics Institute of the Academia Sinica, National Defense Publication, 1975.

[5] Dai Guanzhong, "Model Method of State Estimation", Journal of Northwestern Polytechnical University, No.1 (1979), pp.61-77.

[6] Lasalle,J.P., "The Stability of Dynamical Systems", Society for Industrial and Applied Mathematics, 1976.

SELF-EXCITED RESONANCE OF AEROSTATIC BEARINGS IN A VACUUM ENVIRONMENT

by Fu Xianluo
(Institute of Mechanics, Academic Sinica)

Abstract

The cause of instabilities in an aerostatic bearing system operated in a vacuum environment is studied in this paper. In order to eliminate this type of self-excited resonance, some suitable measures are suggested which can be used to maintain the ambient pressure of the bearing in a range of about $\pm$ 0.2 atm.. This will improve the precision of the instruments using aerostatic bearings as well as increase the percentage yield of qualified bearings.

This work was done under the guidance of comrade Lin Tongji.

I. Suggestion of Problem

The application of aerostatic bearings has become increasingly widespread in many areas of industry, scientific research and national defense. Because their frictional force is small, they possess the special features of small power consumption and cool state operation; they can operate at an extremely high rotating speed, their axis rotating precision is very high and abrasion wear extremely small and therefore has a long operating life; they do not very much require or basically do not require scheduled maintenance but can operate in extremely high or extremely low temperature environments; their noise and vibration are small. Therefore the application of aerostatic bearings is

especially widespread in precision machine tools and precision instruments.

However, it is not that easy for the bearings to realize the above mentioned special features under special application situations. For example, when the ambient pressure of the bearing is very low, in a high vacuum environment, aerostatic bearings can often produce self-excited resonance instability problems. The higher the environmental vacuum the easier it is for the bearing to produce self-excited resonance. To avoid this type of resonance, bearings measurements must be designed accurately and their machining precision requirements are also very high. Therefore, when aerostatic bearings are used in a high vacuum environment, the slightest change in bearing measurements can produce self-excited resonance and thus destroy the normal operation of the precision instruments. Furthermore, the self-excited resonance of aerostatic bearings in this high environment vacuum is also very sensitive to other factors. Errors during machining and measuring, changes of the environmental temperature, the intrinsic frequency of bearings, mounting methods and air feed pressure can possibly bring about self-excited resonance of bearings and cause the normal operation of the aerostatic bearings to break down.

II. Qualitative Analysis

During the design of any aerostatic bearing, the guarantee that it can rotate steadily under certain conditions is an important factor to consider. Naturally, if the bearing system is unstable then before eliminating the instability we consider that the other aspects of the design are worthless. If we do not consider the problem of stability during design or the considerations are incomplete then the vast majority of aerostatic bearings can manifest self-excited resonance.

It has been practically proven that when the aerostatic bearings of a precision instrument is in a high vacuum environment it can manifest self-excited resonance. During resonance a sound can be heard and the resonance can also be felt with the hand. When serious, the bearing makes a shrill sound which shifts the entire base.

The problems of the instabilities in aerostatic bearings has attracted the attention of many researchers who have carried out theoretical analyses of bearings with simple geometric shapes and have adopted stabilization measures [1-3]. However, among many of the actual problems, because the geometric shapes of the bearings were complex (for example, some aerostatic bearings including journal bearings and the Yates bearings of thrust bearings), because it was necessary to use several of these types of bearings in the instrument and because the mounting positions were not matched, the temperature changes and loads endured by the bearings was very large. This caused the calculations of the aerostatic bearings' instabilities to be extremely difficult. Even if the geometric shape were simplified and ideal operation conditions were used so that the set of equations for solving the fluid kinetics becomes possible, we must still use an electronic computer to carry out long computations. Done in this way, the cost is very high and the obtained results can be quite different from the test results.

Therefore, we do not follow the previously used method but simplify the complex geometric shape and appropriately idealize the severe operation conditions so that it is possible to solve the set of kinetic equations. We attempted to carry out qualitative analysis of actual phenomena. Thus, we found the source of the resonance and adopted suitable measures to change the position of the resonance source, and weaken or even eliminate the resonance source.

As regards the aerostatic bearing shown in fig. 1, when the ambient pressure is about atmospheric pressure, operation is normal. When the environmental vacuum is very high, self-excited resonance can appear.

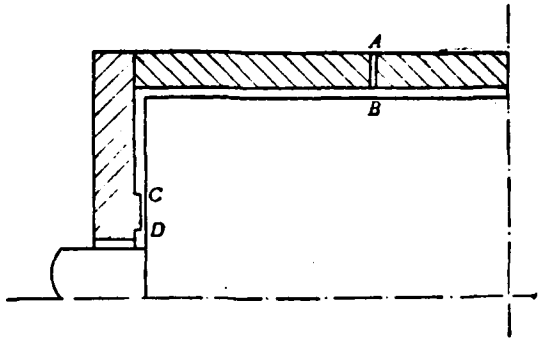

Fig. 1 Scheme of the Aerostatic Bearing

Based on tests, it is only necessary to continually raise the environmental vacuum for this type of aerostatic bearing to produce self-excited resonance. Given this point, we can infer that the resonance source that brought about the self-excited resonance is possibly a supersonic flow appearing in a certain area of the bearing. Naturally, a lowered resonance pressure P_s can cause the vacuity of the self-excited resonance environment to rise. Yet, lowered resonance pressure directly influenced the decrease of the lubricated gas flow and as a result the bearing capacity of the bearing dropped. Although this raised the resonant vacuity of the self-excited resonance we were not able to estimate the maximum load of the instrument during design.

We know from the theories of aerodynamics that to produce a supersonic air flow for a one dimensional flow, as regards geometric shape, it is only necessary to have a first contraction then expansion passage. We can see from fig. 1 that only if there

is an annular intake narrow crevice AB and throttling step CD area on the thrust surface can there be air flow stoppage.

If the resonance source is formed from air flow stoppage caused by the annular intake narrow crevice AB area, then pressures P_B in the B point area must satisfy

$$P_B/P_s \leqslant 0.528 \quad (\gamma = 1.4)$$

Because P_s is positive definite, in order for narrow crevice AB not to become the source of resonance, it is necessary to raise the pressure P_B at the B point, rendering

$$P_B/P_s > 0.528$$

When the width of narrow crevice AB is $\delta\mu$ this produces self-excited resonance and the width of the narrow crevice increases to $(\delta+1)\mu$. When the air flow passes narrow crevice AB the loss will decrease along the way. Thus, P_B is larger than the original value and it possibly does not form the supersonic resonance source. Nevertheless, tests have proven that by enlarging the width of narrow crevice AB, self-excited resonance appears at even lower vacuity than the original vacuity and therefore narrow crevice AB is not the source of resonance. Because the possible source of resonance is only in two areas the source of resonance can only be throttling step CD.

We can also analyze that the source of resonance is the throttling step CD from two other aspects. Firstly, the enlarging of the width of narrow crevice AB caused resonating vacuity to drop. We can see that the enlargement of the intake narrow crevice decreased the loss along the way and thus raised P_B as well as P_C. This can possibly cause $P_D/P_C \leqslant 0.528$. In this way a supersonic air flow is formed beginning from the back edge of throttling step. Secondly, based on tests, when we eliminated the thrust end cover of the bearing, the resonating environment's vacuity noticeably rose. It can also be concluded that throttling

step CD is the source of resonance.

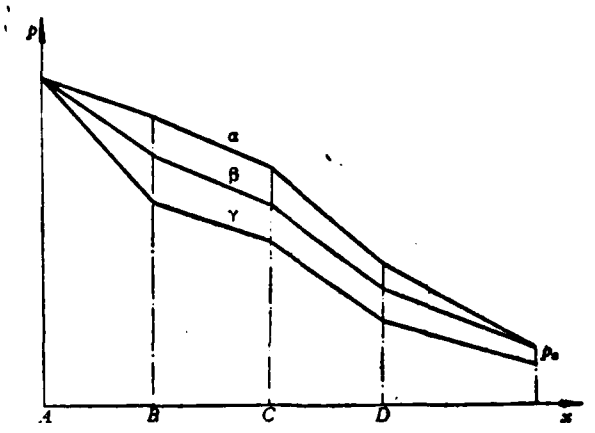

Fig. 2 Schematic of Pressure Distribution

We will use the pressure distribution schematic shown in fig. 2 to further explain. If the air flow in the bearing is an axial symmetrical one dimensional flow, the pressure is a linear distribution, x is the flow line coordinate, the resonance pressure in the A point area is P_s, and the ambient pressure is P_a, the pressures of points, B,C and D are P_B,P_C and P_D.

If pressure distribution curve α corresponds to the width of the intake narrow crevice which is $\delta\mu$, under these conditions, when ambient pressure is P_a self-excited resonance is produced and naturally $P_a/P_c \leqslant 0.528$. If the width of intake narrow crevice AB is decreased, for example decreased to $(\delta - 1)\mu$, then P_c drops and possibly causes $P_a/P_c > 0.528$ and the air flow in front and behind the throttling step to be a subsonic flow. This corresponds to the situation of pressure distribution curve B. If environmental vacuity is continually raised wherein the value of P_a drops, this causes the value of P_a/P_c to drop resulting in

a supersonic flow. If, at this time, the width of the narrow crevice is continually decreased, for example it is $(\delta - 2)\mu$, the value of P_a/P_c corresponding to curve γ also increases, the air flow becomes a subsonic flow and the resonance source is eliminated.

We can see that if the environmental vacuity is raised (P_a is lowered), we can decrease the width of the intake narrow crevice to eliminate the source of resonance. However, if the narrow crevice continually narrows the rate of flow within the bearing will become smaller and smaller and the bearing capacity of the bearings will also become increasingly smaller and not accord with design requirements.

III. Orifice Throttling

We can see from the above qualitative analysis that if ambient pressure continually drops and at the same time a fixed bearing capacity is guaranteed, then the self-excited resonance of the bearing is unavoidable.

To eliminate the resonance source on an aerostatic bearing and guarantee that the bearing itself will not produce self-exciting resonance under any ambient pressure but will be able to operate normally, we can use a sealing cover to seal up the entire instrument using aerostatic bearings. At the same time, we process a critical nozzle (open a specially designated orifice) on the shell of this sealing cover. After causing the ambient pressure to be lower than a certain value, even if the ambient pressure continually drops, the pressure in the sealing cover can be maintained lower than (or close to) a certain design value of atmospheric pressure. Furthermore, for this type of critical nozzle, when the ambient pressure is an atmospheric pressure, it is also necessary to cause the pressure in the sealing cover to be greater than (or close to) a certain design

value of an atmospheric pressure. Done in this way, the resonance source in the bearing is shifted to the shell of the sealing cover.

To find the size of the critical nozzle's aperture we analyzed this problem according to the one dimensional flow theory.

The equation of conservation of momentum for ideal fluid one dimensional constant flows is [4]

$$u\frac{du}{dx}=-\frac{1}{\rho}\frac{dp}{dx} \qquad (1)$$

$$\rho uA=\text{a constant} \qquad (2)$$

Based on the definition of the speed of sound, we have

$$a^2=\frac{dp}{d\rho}$$

We can change equation (1) into

$$udu=-a^2\frac{d\rho}{\rho} \qquad (3)$$

The two sides of equation (2) are logarithmic integrals and when the results are joined with equation (3) and we eliminate $d\rho/\rho$, we obtain

$$\frac{du}{u}=\frac{1}{M^2-1}\frac{dA}{A} \qquad (4)$$

In the formula

$$M=\frac{u}{a} \qquad (5)$$

is the Mach number. We took the logarithmic integral for equation (5) and for the Bernoulli equation

$$\frac{u^2}{2}+\frac{a^2}{\gamma-1}=\text{a constant}$$

integral, we can obtain

$$\frac{dM}{M}=\left(1+\frac{\gamma-1}{2}M^2\right)\frac{du}{u} \qquad (6)$$

Comparing the integrals of equations (4) and (6), we have [4]

$$\frac{A}{A^*}=\frac{1}{M}\left(\frac{1+\frac{\gamma-1}{2}M^2}{\frac{\gamma+1}{2}}\right)^{\frac{\gamma+1}{2(\gamma-1)}}=\Theta^{-1} \qquad (7)$$

In the formula, A* is the critical section of the critical nozzle. Because the volume of the sealing cover is large we can take the flow velocity of the gas in the cover and the Mach number as being equal to zero. We used p_o, ρ_o and T_o to indicate the thermodynamic parameters of the gas in the sealing cover. If the exit section area of the orifice is $\bar{A}$ and counterpressure (ambient pressure) is p', we can deduce that the per second mass flow m of the gas is

$$m=\left(\frac{2}{\gamma+1}\right)^{\frac{\gamma+1}{2(\gamma-1)}}\sqrt{\gamma p_o\rho_o}\,\bar{A}\Theta \qquad (8)$$

Maximum flow m* is

$$m^*=\left(\frac{2}{\gamma+1}\right)^{\frac{\gamma+1}{2(\gamma-1)}}\sqrt{\gamma p_o\rho_o}\,\bar{A} \qquad (9)$$

If the M number in function Θ is indicated as the function of p'/p_o, the [4]

$$\frac{m}{m^*}=\sqrt{\frac{2}{\gamma-1}\left(\frac{\gamma+1}{2}\right)^{\frac{\gamma+1}{\gamma-1}}\left(\frac{p'}{p_0}\right)^{\frac{2}{\gamma}}\left[1-\left(\frac{p'}{p_0}\right)^{\frac{\gamma-1}{\gamma}}\right]} \qquad (10)$$

If m=m*, that is, when the outlet velocity of the gas in the orifice on the sealing cover's shell reaches the speed of sound, the $p'/p_o=0.528$ (taking $\gamma=1.4$). If pressure p_o in the cover must be less than 0.84 atmospheric pressure, then counterpressure p' should be less than or equal to 0.44 atmospheric pressure. In other words, when environmental vacuity is equal to or higher than this value, the pressure in the cover is maintained at 0.84 atmospheric pressure.

Assuming that the gas mass flow flowing into the cover is Q grams/second and the outlet speed of the orifice on its shell reaches the local speed of sound, then the radius of the orifice is

$$R=\sqrt{\frac{Q\sqrt{\tilde{R}T_0}}{\pi\left(\frac{2}{\gamma+1}\right)^{\frac{\gamma+1}{2(\gamma-1)}}\sqrt{\gamma}\,p_0}} \qquad (11)$$

If the flow flowing into the sealing cover is invariant and the size of the orifice is also invariant but the counterpressure rises to an atmospheric pressure, then the pressure of the gas in the sealing cover should satisfy the following formula:

$$\frac{Q}{m^*}=\sqrt{\frac{2}{\gamma-1}\left(\frac{\gamma+1}{2}\right)^{\frac{\gamma+1}{\gamma-1}}\left(\frac{1}{p_e}\right)^{\frac{2}{\gamma}}\left[1-\left(\frac{1}{p_e}\right)^{\frac{\gamma-1}{\gamma}}\right]}$$

Under our conditions, when taking $\gamma=1.4$, the above formula can be changed to:

$$p_{o1}^2=14.92992(p_{o2}^{0.6714}-p_{o2}^{0.2857}) \qquad (12)$$

In order to differentiate, we used p_{o1} and p_{o2} in the above formula to indicate that the orifice's outlet speed is the local speed of sound, and the counterpressure is the pressure in the sealing cover when there is atmospheric pressure.

$$\bar{A}=\left(\frac{2}{\gamma+2}\right)^{-\frac{\gamma+1}{2(\gamma-1)}}\sqrt{\frac{\overline{RT}_{o1}}{\gamma}}\,\frac{Q}{p_{o1}} \qquad (13)$$

To make the selection by designers convenient, table 1 lists the highest counterpressures of supersonic flows brought about under specific flow Q=1.5 grams/second conditions as well as the corresponding pressures p_{o1} and p_{o2} orifice critical sectional area and its radius R.

It should be pointed out that when the ambient pressure is an atmospheric pressure, due to the influence of the boundary layer formed in the throttling orifice, the effective area of the small hole shrinks and therefore pressure p_{02} in the cover is slightly larger than the values listed in table 1.

p'(大气压) (1)	p_{01}(大气压) (2)	p_{02}(大气压) (3)	$\overline{A}$(厘米^2) (4)	R(厘米) (5)
0.10	0.1894	1.0085	0.342	0.330
0.11	0.2083	1.0112	0.311	0.315
0.12	0.2273	1.0121	0.285	0.301
0.13	0.2462	1.0142	0.263	0.289
0.14	0.2652	1.0165	0.244	0.279
0.15	0.2841	1.0189	0.228	0.269
0.16	0.3030	1.0215	0.214	0.261
0.17	0.3220	1.0243	0.201	0.253
0.18	0.3409	1.0273	0.190	0.246
0.19	0.3599	1.0305	0.180	0.239
0.20	0.3788	1.0338	0.171	0.233
0.21	0.3977	1.0382	0.163	0.228
0.22	0.4167	1.0408	0.156	0.223
0.23	0.4356	1.0446	0.149	0.218
0.24	0.4546	1.0486	0.143	0.213
0.25	0.4735	1.0528	0.137	0.209
0.26	0.4924	1.0571	0.132	0.205
0.27	0.5114	1.0616	0.127	0.201
0.28	0.5303	1.0663	0.122	0.197
0.29	0.5492	1.0711	0.118	0.194
0.30	0.5682	1.0761	0.114	0.191
0.31	0.5871	1.0813	0.110	0.187
0.32	0.6061	1.0867	0.107	0.184
0.33	0.6250	1.0922	0.104	0.182
0.34	0.6439	1.0980	0.101	0.179
0.35	0.6629	1.1027	0.0978	0.176
0.36	0.6818	1.1098	0.0950	0.174
0.37	0.7008	1.1160	0.0925	0.172
0.38	0.7197	1.1225	0.0900	0.169
0.39	0.7385	1.1291	0.0877	0.167
0.40	0.7576	1.1359	0.0855	0.165
0.41	0.7765	1.1433	0.0835	0.163
0.42	0.7955	1.1504	0.0815	0.161
0.43	0.8144	1.1572	0.0786	0.159
0.44	0.8333	1.1647	0.0778	0.157
0.45	0.8523	1.1725	0.0760	0.156

Table 1

Table 1 Parameters Associated With Throttling Through An Orifice

Key: 1. (Atmospheric pressure)
2. (Atmospheric pressure)
3. (Atmospheric pressure)
4. (Centimeters^2)
5. (Centimerers)

The instruments with aerostatic bearings are placed in the cover and additional throttling orifices are opened on the cover's shell. This raises the pressure in the cover and eliminates the resonance of the bearing itself. However, resonance caused by supersonic flow appears in the outlet area of the throttling orifices on the sealing cover's shell. The smaller the orifices the higher the resonance frequency and the larger the orifice's outlet speed the greater the resonating energy. Actually, the method of throttling through orifices is to shift the self-excited resonance of the bearing itself to the sealing cover's shell.

Shifting the resonance of the bearing in the sealing cover to the cover's shell is noticeably beneficial because the resonance of the bearing causes precision instruments to work improperly. The resonance of the sealing cover's shell only influences the precision of instruments.

Based on experiences, the influence of the resonance caused by the orifice throttling in the sealed cover's shell on instrument precision can be overlooked but we should use this test to measure the level of this type of influence.

If after measurements this type of influence is found to be formidable, then there are also means to eliminate the influence of this type of resonance on the instruments. For example, we can use a special tube which can easily transfer resonance (its inner diameter must be much larger than the orifice's diameter). The sealing cover's shell is joined to the throttling

orifice and damping equipment is used to fix the throttling orifice on the shell.

We can also directly open the throttling orifice on the shell and mount a muffler in the downstream of the orifice. The muffler can be designed according to information given in related references [5]. However, we should pay attention that the muffler is designed carefully otherwise there is the possibility that it will be unable to muffle sound but rather will cause resonance and intensify the resonance of the sealing cover's shell.

Fine porous throttling can also decrease resonance, that is, a single throttling orifice is made into many fine orifices. When the air flow flows in the fine orifices the viscous formed boundary layer decreasesthe effective area of the fine orifices. Therefore, the area of the fine orifices should be larger than the area of a single orifice. The finer the fine orifices the larger their area. However, they cannot exceed three times the area of an orifice when there is single orifice throttling (this value will be explained in the next section "seepage flow throttling"). Concrete details can be determined from tests.

Seepage-flow throttling discussed in the next section is also a method which can be used for selection.

IV. Seepage Flow Throttling

As regards fine porous throttling, if the orifice's diameter is selected on an increasingly finer basis then the viscosity of the gas becomes the dominant effect. When the orifice's diameter is very fine, which even machining cannot bring about, we can use a porous metal. This is seepage flow throttling. Because the flow speed of seepage flow is very small, seepage flow throttling cannot manifest supersonic resonance.

Based on the Darcy law [6,7] of the seepage flow theory, we can derive

$$m = -\frac{K_p}{\mu} \rho \frac{\Delta p}{\Delta y} S \qquad (14)$$

In the formula, m is the mass flow of the gas, μ is the viscosity, Δ p is the inner and outer pressure difference of the sealed cover, Δ y is the thickness of the porous metal, S is its area, and Kp is the coefficient determined by the porosity of the porous metal. If it is still required that the ratio of the sealed covers ambient pressure and the minimum pressure in the cover be 0.528, and the seepage flow is taken as 1.5 grams/second, then equation (14) can be changed to

$$p_{02}^2 - p_{01}^2 = 0.472 p_{01}^2 \qquad (15)$$

When p_{01}=0.833 atmospheric pressure, ambient pressure p'=0.44 atmospheric pressure, and when the ambient pressure of the sealed cover rises to an atmospheric pressure the pressure in the cover p_{02}=1.2601 atmospheric pressure; when p_{01}=0.568 atmospheric pressure, p_{02}=1.133 atmospheric pressure. Naturally, we can also select an appropriate porous material so that the maximum pressure in the cover is somewhat lower. For example, if p'/p_{01}=0.8, then when p_{01}=0.833 atmospheric pressure, p_{02}=1.1236 atmospheric pressure; when p_{01}=0.568 atmospheric pressure, p_{02}=1.061 atmospheric pressure.

Under our conditions, we can take μ=1.85x10^{-4} grams/centimeter·seconds and if K_p=0.61x10^{-10} meters^2 and Δ y=1 centimeter, then we take the porous metal's sectional area S=1.2146 (centimeters)^2.

Selection of the K_p value is based on the equivalent formula of the seepage flow and fine porous flow [7].

$$K_p = \pi \frac{d_i^4 N_i}{128} \tag{16}$$

In the formula, d_i is the diameter of the fine orifice and N_i is the number of fine orifices on the unit area. If there are twenty-five 0.1 millimeter diameter fine orifices per square millimeter, then

$$K_p = 0.6136 \times 10^{-10} \text{ meters}^2$$

Under these conditions, the aperture rate is 19.63 percent and the aperture area is 3.067 times a single throttling orifice.

Therefore, the selection and placing of $K_p = 0.61 \times 10^{-10}$ meter^2 porous metal 1 centimeter thick and 1.2146 centimeter^2 sectional area on the sealing cover's shell can cause pressure in the cover to be maintained in the 1 ± 0.3 atmospheric pressure range. Naturally, the inner pressure of the sealing cover must be lower in an absolute vacuum.

V. Discussion and Conclusion

If the environmental pressure aerostatic bearing such as the one shown in fig. 1 continually rises, self-excited resonance cannot be avoided under conditions wherein bearing capacity does not influence design. The resonance source at this time is a supersonic flow on the back edge of the throttling step on the thrust surface.

Use of the orifice throttling method can keep the bearing in an environment wherein the sealing cover's ambient pressure continually drops and this will not cause self-excited resonance. However, supersonic flow resonance is produced by the throttling

orifices on the sealing cover's shell. According to experiences, the influence of this resonance on instrument precision can be overlooked.

Under normal ambient pressure, relatively high air feed pressure aerostatic bearings can also produce self-excited resonance. The method suggested in this paper can also be used to resolve this problem.

If after test measurements on the precision of an instrument system it is necessary to eliminate the resonance produced by the throttling orifices on the sealing cover's shell, we can attach a muffler or vibration damper.

Given orifice throttling, because the boundary layer shrinks the orifices of the effective sectional area, when the sealing cover's ambient pressure is an atmospheric pressure, pressure p_{02} in the cover must be slightly higher than the calculated results.

To realize this goal of damping or eliminating vibration we can also use fine porous throttling or seeping flow throttling. As for fine porous throttling, the total sectional area of the fine orifices should be larger than the sectional area of a single throttling orifice. As for seepage flow throttling, when the surrounding ambient pressure is an atmospheric pressure, the pressure is an atmospheric pressure, the pressure in the cover should be higher than orifice throttling under the same conditions. If we select a porous metal with $K_p=0.61\times10^{-10}$ meters^2, 1 centimeter thickness and a 1.2146 centimeter^2 area, then lowest pressure in the cover is lower than the calculated value when in an absolute vacuum.

To sum up, the use of orifice throttling, fine porous throttling and seepage flow throttling can avoid the self-excited

resonance of bearings. The use of orifice throttling can shift this type of vital self-excited resonance from the bearing to the sealing cover's shell and in this way guarantee the normal operation of precision instruments. Although there is no resonance on the shell when seepage flow throttling is used, yet the pressure change range in the cover is large. Fine porous throttling is a compromise plan between the two. However, the size of the orifice apertures and the number of fine orifices must be determined by experimentation. Because of throttling, the bearings always operate in an almost atmospheric pressure ambient pressure. This is not only advantageous to raising the precision of instruments but can also greatly raise the percentage yield of qualified aerostatic bearings.

References

[1] "The Design of Aerostatic Bearings," translated by Ding Weigang et.al., National Defense Publications, 1978.

[2] Licht, L., Elrod, H.G., "An Analytical and Experimental Study of the Stability of Externally Pressurised Gas Lubricated Thrust Bearings", Franklin Institute Report 1-A2049-12, 1961.

[3] Lehmann, R., Wierner, A., Thalkein, E., and Vorberger Hond Walter, R., "Die erste Takstrabe mit luftgelagerten Transporschlitten für 4,5Mp Tragkraft" Neue Technik 6/64, 366-370 and 7/64, 438-441.

[4] "Liquid and Gas Mechanics," Vol. 1, Translated by Lin Hongsen et.al., People's Education Press, 1958.

[5] Fang Danchun, "Aerodynamic Noise and Muffler," Scientific Publications, 1978.

[6] L.Pulangte, author, "An Introduction to Fluid Mechanics," Translated by Guo Yonghuai et.al., Scientific Publications, 1974.

[7] V.N. Constantinesu, 《Gas Lubrication》, New York,ASME.1969.

A NEW COMPLEX ELECTROHYDRAULIC SERVOSYSTEM

by You Jinlu
(China Precision Engineering Institute for Aircraft Industry)

Abstract

The servosystem of a flight motion simulator requires its servovalve-motor combination to possess a great ratio of continuous adjustable rate (e.g. more than 1,100). In general, only the electrohydraulic servosystem is available to the simulator with a great load inertia (e.g. 30 kilograms·centimeters·seconds^2). This paper presents a complex electrohydraulic system, which increases the ratio of adjustable rates from 180 to about 1800, and improves other technical performances so as to meet the requirements of the servosystem in the flight motion simulator.

This paper lists some ratios of adjustable rates of domestic servomotors used in simulators, analyzes the reasons of the low ratio of adjustable rates of the piston type motor and puts forward some measures to improve it. The paper also describes the principles of the complex electrohydraulic servosystem, gives the theoretical analysis and derives the block diagrams and transfer functions. Then, it gives the dynamic analysis of the complex system and makes a comparison with the original one. Finally, it provides the typical data and plots of experiments.

I. Preface

Aside from basic technical requirements, for the following

system of an electrohydraulic flight motion simulator it is especially necessary that the hydraulic servomotor have a large (greater than 1,000) continuous adjustable rate and small low speed pulsation. Domestic flight motion simulators all use the "traditional" electrohydraulic servosystem (called the original system). This type of system can only rely on a motor developed with a great ratio of adjustable rate and a (flow) valve to match it. After tests, we selected a servovalve-motor combination to accord with the above requirements. This design presented even greater technical and manufacturing difficulties for the motor and valve which were not easily realized. Table 1 is the ratio of adjustable rate for a piston type motor developed over many years. Because they are all large, the technical performances of the system could frequently not be realized. The electrohydraulic complex system (called complex system) used the YCM-27-1 motor and DYSF-3Q-1 value (they need not match) which were unable to satisfy the requirements of the original system, and was thus able to increase the servovalve-motor combination's ratio of adjustable rates from 110-180 to over 1,800. Moreover, dynamic characteristics did not change and other performances also improved thus satisfying the requirements of the system.

(1) 马达型号	(2) 转速范围，转/分	(3) 调速比
YMD	20～3000	150
ГМ-00	(4) (13至32)～3000	100～230
YCM-27-1	(5) (6至10)～1100	110～180
ZM-40	10～2500	250
ZM-25	4～2500	750

Table 1

Key: 1. Motor model
2. Rotational speed, rotations/minute
3. Ratio of adjustable rate
4. (13 to 22)
5. (6 to 10)

II. Means For Improving the Piston Type Motor

1. The Friction Torques of the Running Components in a Piston Type Motor is the Major Factor Influencing the Motor's Low Speed Performance

The total friction torque T_f [1] of the running components in the motor is

$$T_f \propto D_m(P_1+P_2) \qquad (1)$$

and the running friction torque T_f [1] is

$$T_f = \frac{\dot{\theta}_m}{|\dot{\theta}_m|} C_f D_m (P_1+P_2) \qquad (2)$$

In the formula, $\dot{\theta}_m$, D_m, P_1 and P_2 are the motor's rotating speed displacement and pressures of the two chambers; in $P_1+P_2=P_s$, P_s is the power source pressure; and C_{fs} and C_f are the static and running friction coefficients in the motor. C_f and C_{fs} change in accordance with $\dot{\theta}_m$ (see fig. 1). The difference between the static running friction torques is the reason for the production of the motor's (very low) starting rotating speed.

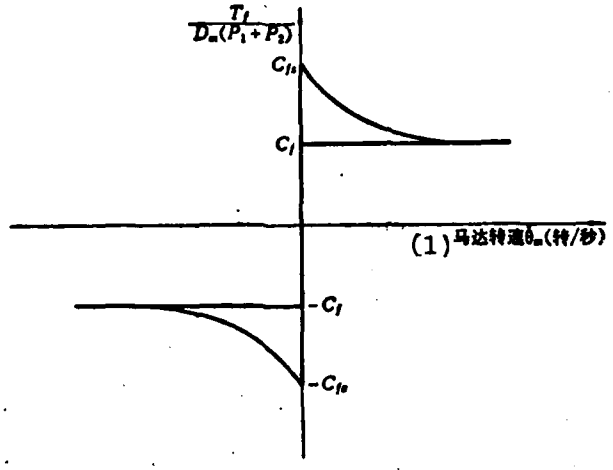

Fig. 1 Starting and Running Friction Torques Due to Pressure in the Motor Chambers

Key: 1. Motor's rotating speed $\dot{\theta}_m$ (rotations/second

We can see from fig. 1 and formulas (1) and (2) that as P_2 increases the starting rotating speed of the motor rises. Table 2 is typical test data for the starting rotating speed of the YCM-27-1 motor. We can obtain the same conclusions from table 2 and reference [1], 4-4. At low speed P_1-P_2 is very small and thus lowering P_s is one effective method for improving the motor's low speed.

(1)P_s, 千克/厘米²	P_1, 千克/厘米² (2)	P_2, 千克/厘米² (3)	P_1-P_2, 千克/厘米²	(4) 起动转速, 转/秒 (5)
50	7.5	6.2	1.3	3/68
80	10	8.5	1.5	6/65
100	12	9	3	7/65
140	60	51	9	9/57

Table 2

Table 2

Key: 1. P_s, kilograms/centimeter^2
2. P_1, kilograms/centimeter^2
3. P_2, kilograms/centimeter^2
4. P_1-P_2, kilograms/centimeter^2
5. Starting rotating speed, rotations/second

2. The Motor's Lowered Energy Source Pressure During Low Speed Does Not Influence the Motor's Output Torque (Specified Inertia Time of Load Inertia)

The torque T_L of the external load conveyed by the motor is [1]

$$T_L=D_mP_L-C_dD_m\mu\dot{\theta}_m-\frac{\dot{\theta}_m}{|\dot{\theta}_m|}C_fD_m(P_1+P_2)-\frac{\dot{\theta}_m}{|\dot{\theta}_m|}T_c \qquad (3)$$

In the formula, $P_L=P_1-P_2$; C_d is the damping coefficient, and μ is the absolute viscosity of the liquid. The mean flow Q_L of the motor is [1]

$$Q_L=D_m\dot{\theta}_m+\left(C_{im}+\frac{C_{em}}{2}\right)P_L \qquad (4)$$

C_{im} and C_{em} are the internal and external leakage coefficients of the motor. At the same time, Q_L is

$$Q_L=C_dWX_v\sqrt{\frac{1}{\rho}(P_s-P_L)} \qquad (5)$$

W and X_v are the valve opening area gradient and opening travel; and ρ is the density of the liquid. By solving formulas (4) and (5) we obtain P_L letting $K=C_dWX_v\sqrt{\rho}$; $K_1=2C_mD_m$; $C_m=C_{im}+C_{em}/2$,

afterwards we substituted P_L value into formula (3) and obtained formula (6)

$$T_L = D_m \frac{-(K_1\dot{\theta}_m + K^2) + \sqrt{(K_1\dot{\theta}_m + K^2)^2 + 4C_m^2(K^2P_s - \dot{\theta}_m D_m^2)}}{2C_m^2} - C_s D_m^2 \dot{\theta}_m$$

$$- \frac{\dot{\theta}_m}{|\dot{\theta}_m|} C_f D_m (P_1 + P_2) - \frac{\dot{\theta}_m}{|\dot{\theta}_m|} T_c \qquad (6)$$

At low speed, when the valve-motor combination is under the same inertial load, $\dot{\theta}_m$ is identical and P_s decreases. The first item on the right side of formula (6) decreases very little[F.N.1], the third item forms a ratio with $P_1+P_2=P_s$ which decreases and during low speed $P_s \gg P_L$. Therefore, T_L [formula (6)] does not decrease because of the decrease of P_s and T_L (with the same inertia) is only related to $\dot{\theta}_m$ and is not influenced by P_s (naturally, there should be sufficient P_s at the time to guarantee the motor's displacement necessary at this $\dot{\theta}_m$). Table 3 lists experimental data. Therefore, if we use the P_s which rises and falls with the high and low of $\dot{\theta}_m$, that is to say, use the P_s which rises and falls with the size of the input speed signal u_{in}, this can improve the low speed performance of the valve-motor combination.

F.N.1 Actually in $P_s \downarrow \rightarrow Q_L \downarrow \rightarrow \dot{\theta}_m$, in order for $\dot{\theta}_m$ not to change, X_v must be enlarged. However, K^2P_s drops a little and $C_m \ll 1$. Therefore, the first item on the right side of formula (6) decreases even less with the P_s drop.

(1) P_s千克/厘米²	20	20	42	60	70	90	100	110	120	130
(2) $\dot{\theta}_m$转/秒	1/6	1/7	1/9	1/7	1/7	1/8	1/8	1/7.5	1/5	1/6
(3) F●千克	8.2	7.9	9	10	8.6	10	9	8	9.2	8.2

(4) P_s千克/厘米²	15	20	30	41	50	60	70
(5) $\dot{\theta}_m$转/秒	1/24	1/20	1/27	1/21	1/22	1/19	1/17
(6) F●千克	3.4	3.3	3.4	2.6	2	.5	2

(7)● 实验时力臂相同，所以力矩T_L用力F表示。

Table 3 Experimental Data of Function $T_L(P_s)$ (Load and $\dot{\theta}_m$ Unchanged)

Key: 1. P_s kilograms/centimeter^2
2. $\dot{\theta}_m$ rotations/second
3. F (F.N.1) kilograms
4. P_s kilograms/centimeter^2
5. $\dot{\theta}_m$ rotations/second
6. F (F.N.1) kilograms
7. F.N.1 The arm was the same during testing and therefore torque T_L was indicated by force F

3. Analysis of the Valve-Motor Combination With P_s Rising and Falling In Accordance with the High and Low of $\dot{\theta}_m$

The flow Q_L of the ideal zero (square) four opening flow valve is [1]

$$Q_L = C_d W X_v \sqrt{\frac{1}{\rho}\left(P_s - \frac{X_v}{|X_v|} P_L\right)} \qquad (5')$$

For convenience of deduction, if $X_v > 0$, therefore

$$Q_L = C_d W X_v \sqrt{\frac{1}{\rho}(P_s - P_L)} \qquad (5)$$

As shown in fig. 2(a), we let

$$P_s = P_Q = P_{s0} + \Delta P_s \qquad (7)$$

In the formula, P_{so} and ΔP_s are the constant and variable parts of the variable pressure.

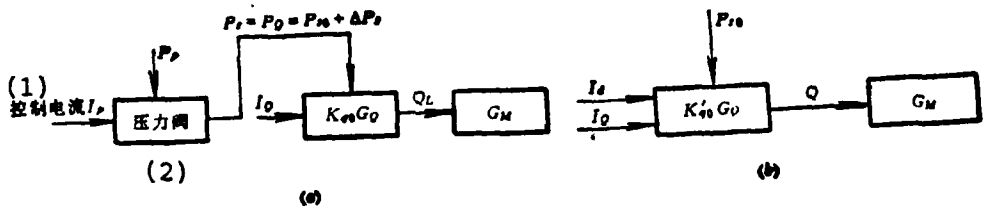

Fig. 2 Schematic Diagram of Flow Servovalve-Motor With Pressure Control Servo

Key: 1. Control current I_p
2. Pressure valve

When formula (7) is substituted into formula (5), we obtain

$$Q_L = C_d W X_v \sqrt{\frac{1}{\rho}(P_{s0} + \Delta P_s - P_L)} = K'_{q0} X_v \sqrt{1 - \frac{P'_L}{P_{s0}}} \qquad (8)$$

In the formula, $K'_{qo} = C_d W \sqrt{P_s 0/\rho}$; and $P'_L = P_L - \Delta P_s$. We can see that the flow valve can use the I_d equivalent for its flow because the P_Q is limited. Moreover, $K_q o = C_d W \sqrt{P_s \rho}$ shrinks to

k'_{qo} and P_s changes to P_{so} as shown in fig. 2(b). Because $P'_L < P_L$, under ideal conditons P'_L is close to a constant. When we compare formulas (5) and (8) we know that function $Q_L(X_v)$ [or $Q_L(I_Q)$] is even closer to being linear and therefore the pressure control flow valve is even more suitable as a control element.

We can see from formula (8) that the analysis of the valve-motor combination in reference [1] is suitable for use here. However, it must use P_{so}, P'_1, P'_2, P'_L and K'_{qo} to replace P_s, P_1, P_2, P_L and K_{qo}. We can also obtain from its dynamic analysis: (1) because $\sqrt{1-P'_L/P_{so}}$ is close to a constant, this causes the fixed position spring effect of the steady flow force in the flow valve and the non-linearity of the damping coefficient produced by the transient flow force to decrease; (2) the liquid flow force produced by the liquid flow impact baffler on the loaded spring effect produced on the baffler decreased which was advantageous to the stability of the baffle valve; (3) the static state rigidity of the valve-motor combination decreased little with the increase of P_L [1].

III. The Complex Electrohydraulic Servosystem

1. Function Principles of the Complex Electrohydraulic System

See fig. 3 for the functional diagram of the complex electrohydraulic (velocity) servosystem.

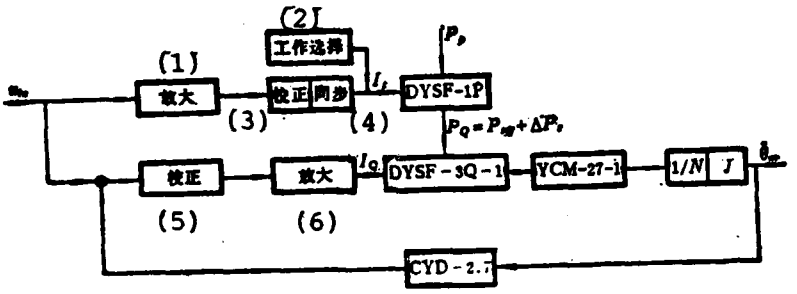

Fig. 3 Functional Diagram of the Complex Electrohydraulic (Velocity) Servosystem

Key: 1. Amplification
2. Operation selection
3. Correction
4. Synchronous
5. Correction
6. Amplification

The complex system allows the valve-motor combination to operate under variable oil pressure P_Q . P_Q is realized by the pressure control servovalve (called the pressure valve). P_Q forms a direct ratio with control current I_p [2,3]. The frequency band width of the pressure valve is about 100 cycles/second and the influence of its dynamic characteristics on the flight motion system with a frequency band width of 10 cycles/second can be overlooked. The complex system synchronizes the control pressure valve and flow valve by the given signal u_{in} (see fig.3). In this way, when there is a small signal the flow valve operates in low pressure, and with a small opening (small flow) the motor operates at a low speed; when there is a large signal the flow valve operates in a high oil pressure and with a large opening (large flow) the motor operates at a high speed. Thus, the low speed performance and dynamic performance of the valve-motor combination satisfies the requirements of the system. The

stability performance of the system is the same as that of the original system because the open-loop segment's stability does not have any influence on the closed-looped loop included in the complex system [4].

2. Block Diagram and Transfer Functions of Complex Servosystem (Velocity System)

(1) Block Diagram of Flow Valve-(Valvecontrolled) Motor With Pressure Control Servo

We can infer the block diagram of flow valve-(valvecontrolled) motor with pressure control servo from formula (8) and motor torque equation [1]. $P_L - \Delta P_s$ replaces P_L' and after structure transformation we obtain fig. 4.

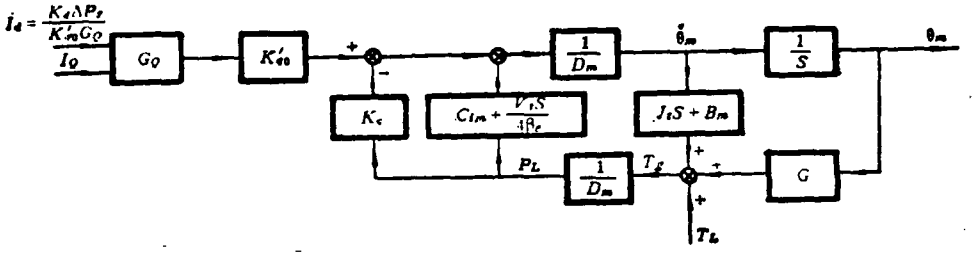

Fig. 4 Block Diagram of (Flow-) Valve (Valve-Controlled) Motor With Pressure Control Servo

In the figure, G_Q is the flow valve's transfer function, the valve frequency band is within 100-200 cycles/second, for this system $G_Q \approx 1/(T_Q S + 1)$, and T_Q is a time constant. The other symbols in the figure are the basic parameters of the valve and motor [1]. Letting $K_d = K_c + C_{im} + V_t S/4\beta_e$, we can see that because the pressure control's controlling effect on the flow valve's flow is equivalent the control current I_d is $I_d = K_d \Delta P_s / K'_{qo} G_Q$. From the above mentioned $\Delta P_s = G_p I_p$, $G_p = K_p/(T_p S+1)$. G_p is the pressure valve's transfer function; K_p is the pressure gain; and T_p is the time constant. When $\Delta P_s = I_p G_p$ is substituted into

the I_d formula we obtain the equivalent transfer function G_d from I_p to I_d

$$G_d = \frac{I_d}{I_p} = \frac{K_d G_p}{K'_{d0} G_Q} = \frac{(K_e + C_{lm} + V_t S/4\beta_e) K_p (T_Q S + 1)}{K'_{d0} (T_p S + 1)}$$

Thus, we obtain the block diagram of the complex (velocity) system (see fig. 5).

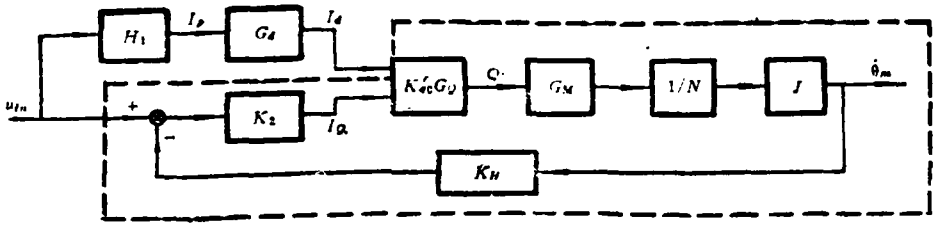

Fig. 5 Block Diagram of Complex (Velocity) Servosystem

In the figure, H_1 is the transfer function of the corrected segment, and $H_1 = H_1'(T_1 S+1)$. H_1' is the amplification coefficient; T_1 is the time constant; $G_M = K_M / (T_M^2 S^2 + 2\xi T_M S + 1)$ is the motor's transfer function and $K_M = 1/D_m$; K_H is the amplification coefficient of CYD-2.7.

(2) Transfer Function of Electrohydraulic (Velocity) Closed System

After the complex system's closed-loop transfer function [5] written from fig. 5 is revised, it is

$$\phi_{\text{复}(1)}=\frac{K_M J\left[K_e+C_{im}+V_t S/(4\beta_e)\right](T_Q S+1)(T_1 S+1)H_1' K_p+K_2 K_{q0}'(T_f S+1)\}}{\left[K_2 K_{q0}' K_M K_H J+N(T_Q S+1)(T_M^2 S^2+2\xi T_M S+1)\right](T_p S+1)} \tag{9}$$

Key: 1. Complex

The closed-loop transfer function ϕ_{original} of the original system (velocity system) is (see the inner part of the broken line of the block diagram in fig. 5)

$$\phi_{\text{复}(1)}=\frac{K_2 K_{q0} G_Q G_M J/N}{1+K_2 K_{q0} G_Q G_M J/N}=\frac{K_2 K_{q0} K_M J}{K_2 K_{q0} K_M K_H J+N(T_Q S+1)(T_M^2 S^2+2\xi T_M S+1)} \tag{10}$$

Key: 1. Original

3. Analysis of the Dynamic Characteristics of an Electrohydraulic Complex (Velocity) Closed System

The characteristic equation of the complex closed system obtained from formula (9) is

$$\left[K_2 K_{q0}' K_M K_H J+N(T_Q S+1)(T_M^2 S^2+2\xi T_M S+1)\right](T_p S+1)=0 \tag{11}$$

The characteristic equation of the original system's (velocity system) closed system is obtained from equation (10)

$$K_2 K_{q0} K_M K_H J+N(T_Q S+1)(T_M^2 S^2+2\xi T_M S+1)=0 \tag{12}$$

Equations (11) and (12) separately show the dynamic characteristics of two types of closed systems and there is only an extreme point $s=-\frac{1}{Tp}$ difference between them. From

the point of view of the root locus [5,6], because $T_M \gg T_p$ on the S complex plane, when compared to the pair of conjugate extreme points of the motor, extreme point $s = -\frac{1}{T_p}$ is far from the imaginary axis and its influence on the system's dynamic characteristics can be overlooked. The dynamic characteristics of these two types of systems are mainly derived from the conjugate extreme points of the motor, in other words, the dynamic characteristics of the two types of systems are identical. We know from equation (9) that after H_1', K_p and K_{qo}' are suitably disposed, the $\Phi_{complex}$ numerator and the third degree factor of the denominator cancel eachother. In this way, the dynamic characteristics of the complex system are improved even more.

IV. Comparison Test of the Complex Electrohydraulic (Velocity) System and the Original (Velocity) System (Equivalent Load of System Band and Flight Motion Simulator Load Equal Inertia)

Two rounds of multiple open-loop and closed-loop static tests and dynamic tests were carried out on the two systems composed of different DYSF-3Q-1P and DYSF-3P (flow) valves and the YCM-27-1 motor (after systems tests this motor was found to be unable to satisfy the technical index of the original system) with DYSF-1P and DYSF-3P pressure valves and CYD-2.7 and ZCF-16 velocity (they need not match). Table 4 is typical data of two rounds of open-loop low speed tests on the two types of systems.

	(1)组 别	(2)原 系 统	(3)复 合 系 统
(4)最低转速	1	10～17	0.6～0.7
(5) 转/分	2	7～20	0.3～0.4

Table 4

Table 4

Key: 1. Set
2. Original system
3. Complex system
4. Lowest rotating speed
5. Rotations/minute

We can see that the complex system's valve-motor combination ratio of adjustable rate enlarged more than ten fold and satisfied the requirements of the flight motion simulator. Figs. 6 and 7 are two rounds of open-loop dynamic tests of the amplitude (phase)-frequency responses of small signals in the two types of systems (the signals are rated values of 0.4~16 percent and 1.6~68 percent). In the second round of tests, when the frequency is 0.1 cycles/second, the open-loop amplification multiple is: the complex system is 130 1/second , and the original system only reaches 89 1/second because of instability.

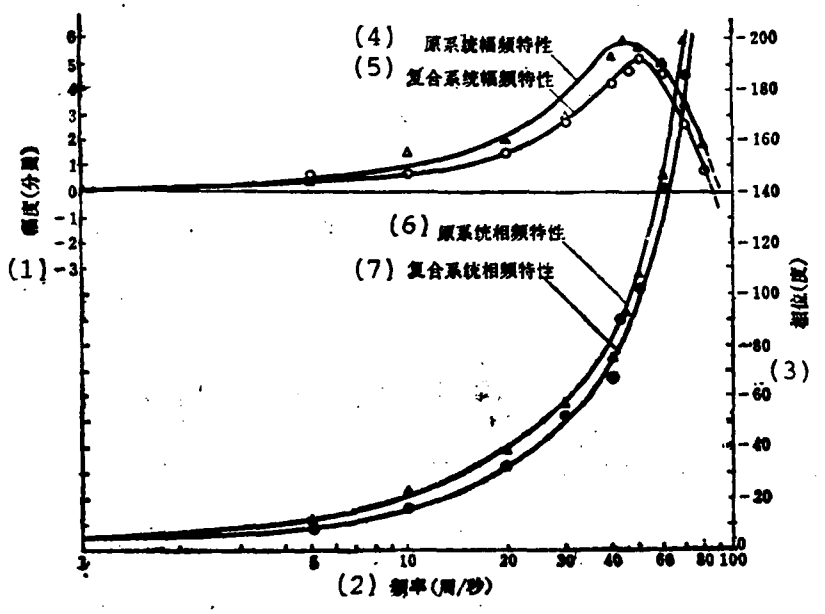

Fig. 6 Amplitude (Phase)-Frequency Responses of Small Signals in the Open-Loop System

Flow valve DYSF-3Q-1(08#); pressure valve DYSF-1P; YCM-27-1 (03#) motor; 16 percent of amplitude's rated value. K_{on} 1/50 1/second; K_{off} 1/50 1/second

Key: 1. Amplitude (decibels)
2. Frequency (cycles/second)
3. Phase (degrees)
4. Amplitude-frequency responses of original system
5. Amplitude frequency responses of complex system
6. Phase-frequency responses of original system
7. Phase-frequency responses of complex system

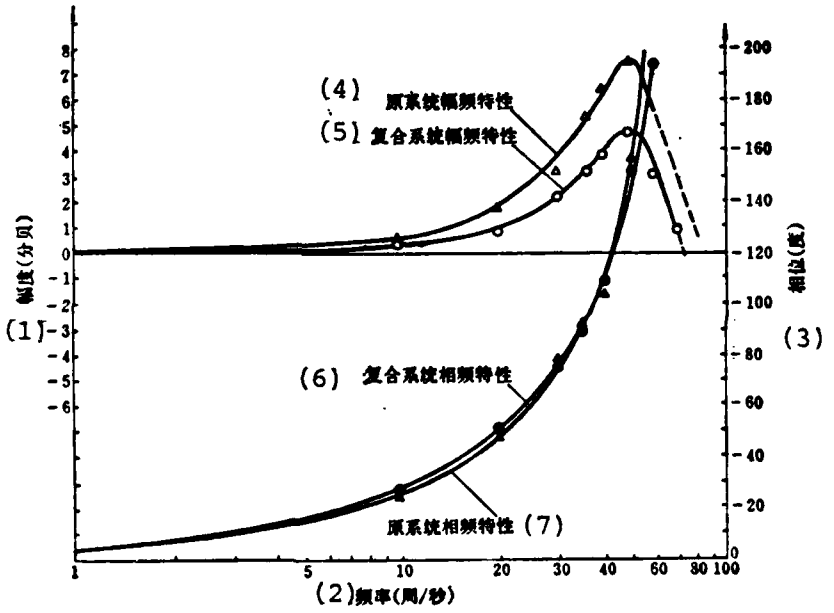

Fig. 7 Amplitude (Phase)-Frequency Responses of Small Signals in the Open-Loop Systems

Flow valve DYSF-3Q-1 (04#); pressure valve DYSF-3P YCM-27-1 (05#) motor; 7 percent of amplitude's rated value

Key: 1. Amplitude (decibels)
2. Frequency (cycles/second)
3. Phase (degrees)
4. Amplitude-frequency responses of original system
5. Amplitude-frequency responses of complex system
6. Phase-frequency responses of complex system
7. Phase-frequency responses of original system

Fig. 8 is two rounds of tests on the output signal wave forms of two types of closed-loop systems (there is no phase relationship between each wave form and their amplitude scale's are also unrelated).

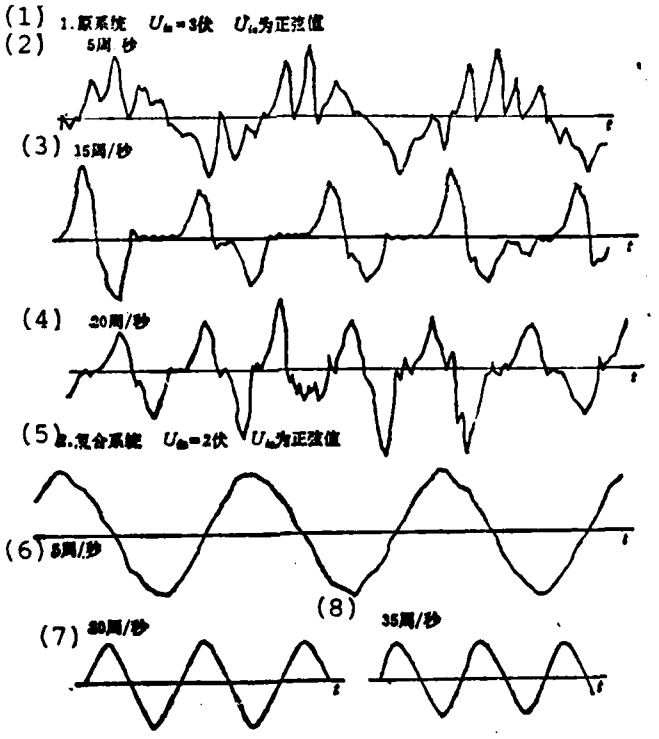

Fig. 8

Fig. 8 Output Signal Wave Forms of (Velocity) Closed-Loop Systems

Key: 1. Original system U_{in}= 3 volts, U_{in} is the sine value
2. 5 cycles/second
3. 15 cycles/second
4. 20 cycles/second
5. Complex system, U_{in}=2 volts, U_{in} is the sine value
6. 5 cycles/second
7. 30 cycles/second
8. 35 cycles/second

Fig. 9 is the amplitude (phase)-frequency response of big signals in the open-loop complex system (68 percent of the rated value). The frequency band width drop from the 35 cycles/second of the small signals to 30 cycles/second is rational [7].

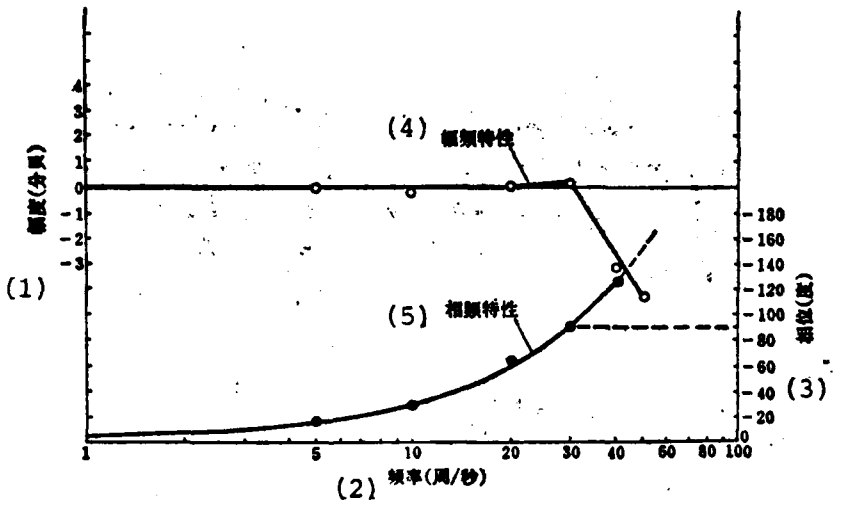

Fig. 9 Amplitude (Phase_-Frequency Response of Big Signals in the Open-Loop Complex System

Flow valve DYSF-3Q-1 (04#); pressure valve DYSF-3P; YCM-27-1 (05#) motor; 16 percent of amplitude's rated value.

Key: 1. Amplitude (decibels)
2. Frequency (cycles/second)
3. Phase (degrees)
4. Amplitude-frequency responses
5. Phase-frequency responses

Figs. 6 and 7 show that the dynamic characteristics of the two systems are the same and that the damping of the complex system is larger. Fig. 8 shows that the complex system's output distortion is small, its dead area is small and its damping coefficient is large so that controllability and stability are both good.

To sum up, when similar motors and valves are used, the complex system, as compared to the original system, can greatly improve the low speed performance of the valve-motor combination and cause the ratio of the adjustable rate of the valve-motor to enlarge more than ten fold, the system to be non-linear, the dead area to be relatively small and the system's damping coefficient to be relatively large. When the open-loop amplification multiple is the same, the system's stability is good and thus it is easy to realize the technical performance of the flight motion simulator's servosystem. This decreases the harsh technical requirements for the motor and valve and decreases the difficulty of developing motors. It also raises the technical performance of the system.

References

[1] "Hydraulic Control System" (United States) H.E. Meilite, author, Chen Yanqing, translator, Scientific Publications, 1978, pp. 46-52, 75-170.

[2] Moog Series 15 pressure control servovales (U.S. patent No2.931.398).

[3] Scientific and Technological Information, Vol. 2(1978), Edited by China Precision Engineering Institute for Aircraft Industry.

[4] "Automatic Regulation Theory of Frequency Method," (Soviet Union) H.T. Kuzuofukefu, author, Zhang Minghua, translator, National Defense Industries Publications, 1966, p. 190.

[5["Modern Control Engineering," (Japan) Xufangshengyan, author, Hu Boying et.al., translation, Scientific Publications, 1978, Chapter 8.

[6] "The Root Locus Method in the Automatic Control Theory," (Soviet Union) Э .Г . Wujieerman, author, Sun Wu, translator, Shanghai Science and Technology Press, 1966.

[7] "The Selection Method of Electrohydraulic Servovalves," Electrohydraulic Servotechnology, 1978.1, Edited by Electrohydraulic Servotechnology Editing Group, translated by Li Yixuan from (Japans) Oil Pressure Technology, 1973.4.

A COMPUTATIONAL GEOMETRY METHOD FOR BLADE SPACE GEOMETRIC DESIGN

by Liu Dingyuan
(Fudan University)

Zhao Yuqi, Zhang Tingxiong and Xiao Hongen
(Nanhua Powerplant Research Institute)

Abstract

This paper presents a new method of computer-aided blade geometric design which combines several typical methods of computational geometry developed recently (including Bézier patches, B-spline patches and Bézier-B-spline mixed patches etc.) with the space shaping for aerojet blades. An integral mathematical model for a blade configuration is obtained and the curved blade is jointed by a set of 3 times 2 order mixed surface patches. Thus, it is advantageous to the computational analysis of the blade's three dimensional flow field performance and limited strength as well as combining with numerical control processing. Actual cases show that this method is simple, has a small amount of computations and is effective for the design of blades with large curvatures.

I. Preface

Blade shape design is an important key in computer-aided blade design and is closely connected to the blade's aerodynamic and strength computations. In the past, plane surface shaping was commonly used in engineering and later they carried out the method of space superposition for the given profile's center of gravity law along the high point of the blade. There

is no integral mathematical model for the blade and processing is complex which presents difficulties for computer-aided design and manufacture.

Present computational geometry has attained remarkable advancements in configuration designs[1-4]. This paper attempts to find and investigate the application of certain of the newest achievements [4,5] in the configuration design of aerojet blades as well as the manufacturing laws for high load large curved turbine blades. A certain number of design examples have shown that the space shaping method for blades suggested in this paper is simple, flexible, directly perceived and requires a small amount of computations. The blade profile has an integral mathematical formula which can conveniently find the contour of an arbitrary section, is convenient for computing the aerodynamics of the blade's three-dimensional flow and analyzing the finite element's strength. Moreover, processing is simple and it is not necessary to carry out blade fitting [6]. This method is also easily extended to conical and flow surfaces.

II. Mathematical Model

Although the curvature of the blade is large chordwise, yet the blade's high direction becomes level approaching a straight line. Therefore, the twisted space patch is close to a ruled surface or is a ruled surface. For this reason, we use a surface patch along the high part of the blade and use any surface patch chordwise to describe the blade profile. Moreover, in the surface patch used, the u line uses the parametric cubic curve and the v line uses the parametric quadratic curve, that is, the 3 times 2 order mixed surface patch. They can utilize a unified mathematical formula:

$$\vec{P}(u,v)=[u^3\ u^2\ u\ 1][M]_k\begin{bmatrix}\vec{B}_{k_{i,0}} & \vec{B}_{k_{i,1}} & \vec{B}_{k_{i,2}}\\ \vec{B}_{k_{i+1,0}} & \vec{B}_{k_{i+1,1}} & \vec{B}_{k_{i+1,2}}\\ \vec{B}_{k_{i+2,0}} & \vec{B}_{k_{i+2,1}} & \vec{B}_{k_{i+2,2}}\\ \vec{B}_{k_{i+3,0}} & \vec{B}_{k_{i+3,1}} & \vec{B}_{k_{i+3,2}}\end{bmatrix}[N]\begin{bmatrix}v^2\\ v\\ 1\end{bmatrix} \qquad (1)$$

In the formula, $[\vec{B}]$ is the characteristic polyhedron vertex position vector matrix; i is surface patch sequence number; and k is the mixed surface patch type index.

When k=1, the u line of the surface patch is a uniform cubic B-spline curve and should take

$$[M]_1=\frac{1}{6}\begin{bmatrix}-1 & 3 & -3 & 1\\ 3 & -6 & 3 & 0\\ -3 & 0 & 3 & 0\\ 1 & 4 & 1 & 0\end{bmatrix} \qquad (1a)$$

When k=2, the u line is the X-spline suggested by Sun Jiachang and at this time

$$[M]_2=\frac{1}{2}\begin{bmatrix}-1 & 5 & -5 & 1\\ 3 & -9 & 6 & 0\\ -3 & 3 & 0 & 0\\ 1 & 1 & 0 & 0\end{bmatrix} \qquad (1b)$$

When k=3, the u line is the cubic Bézier curve and at this time

$$[M]_3=\begin{bmatrix} -1 & 3 & -3 & 1 \\ 3 & -6 & 3 & 0 \\ -3 & 3 & 0 & 0 \\ 1 & 0 & 0 & 0 \end{bmatrix} \qquad (1c)$$

When the v line is a quadratic Bézier curve and there are no interpolation requirements, at this time

$$[N]=\begin{bmatrix} 1 & -2 & 1 \\ -2 & 2 & 0 \\ 1 & 0 & 0 \end{bmatrix}$$

In order for the contour formed from the surface to satisfy points E and H, we used $\overline{EF}$ and $\overline{HG}$ as its tangent. Therefore, its vertex must be extrapolated according to the parabolic qualities (see fig. 1).

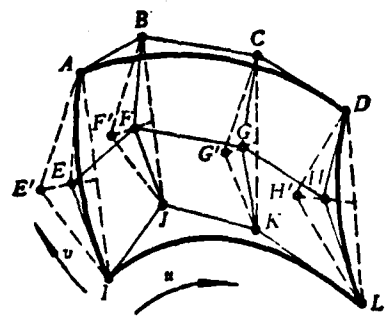

Fig. 1 3 Times 2 Order Bézier Patches

After deduction

$$[N]=\begin{bmatrix} 2 & -3 & 1 \\ -4 & 4 & 0 \\ 2 & -1 & 0 \end{bmatrix} \qquad (1d)$$

Naturally, after this type of processing, the v line of the surface is the quadratic Bézier curve of the interpolation requirement. Moreover, the u line in the middle section must be tangent to the given leading and trailing edge points of tangency.

III. Design Method

How do we provide the characteristic polyhedron vertex position vector and how many patches are used to describe the blade prfile? This is the crux of this method.

We divided the apex position vortex of the characteristic polyhedron in space into three basic sections. Firstly, based on past blade shaping experience [7] we gave the basic point of the characteristic polygon on the basic section and afterwards gave the necessary control points based on the type k of the computational geometry method and went through revision for final complete shaping. For this reason, we used the two paths ard three types method for specific shaping.

1. The Bézier Method of Blade Shaping

This is a method which uses a small amount of surface patch to individually describe the curve and back profile of the blade. Because the curvature changes of the blade curve's contour are relatively uniform, we used 3 times 2 Bézier surface patches; the curvature changes of the back profile of the blade were

relatively large and therefore was joined by two Bézier surface patches (see fig. 2).

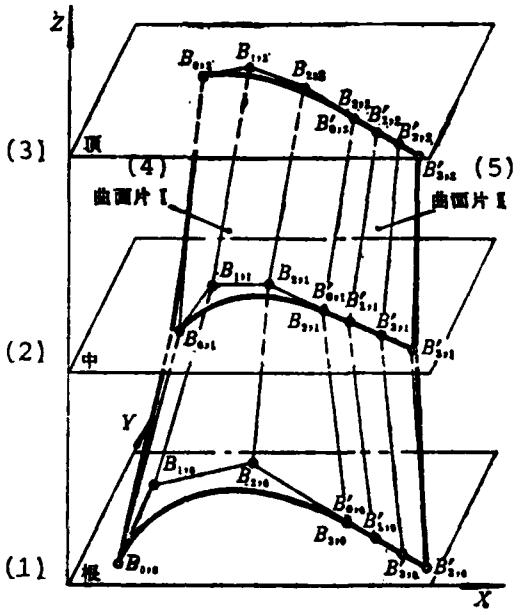

Fig. 2 A Surface Built by Two 3 Times 2 Order Brézier Patches

Key: 1. Root
2. Middle
3. Apex
4. Surface patch I
5. Surface patch II

To satisfy joining C^1 continuously, we used strong ample conditions, and not including

$$\vec{B}_{3j} = \vec{B}'_{0j} \quad (j = 0, 1, 2) \qquad (2)$$

the collinear three points must also satisfy:

$$\vec{B}'_{1j} - \vec{B}'_{0j} = \lambda (\vec{B}_{3j} - \vec{B}_{2j}) \qquad (3)$$

In the formula, λ is the proportionality constant.

When using the Bézier method for blade shaping it is necessary to give the boundary conditions of the surface patch. The two joining point position vectors and common tangent directions must also be determined for the back of the blade. Generally, this joining point has the straight line section in back of the blade as the starting point and the tangent direction is its linear direction. If there is no linear section then this point is selected on the throat tangent point G area. Its tangent direction is determined by the tail end corner on the back of the blade. In short, the determination of the cubic Bézier curve on the basic section is similar to the two point two tangent method commonly seen in engineering curve shaping. The different ones still must determine the other two apex $\vec{B}_{1j}$ and $\vec{B}_{2j}$ along the tangent direction of the two extreme points. This paper used a large curvature blade back and blade curve as references. They were determined by test gathering method and the results were excellent.

2. The B-Spline Method of Blade Shaping

The whole blade profile is composed of a set of 3 times 2 order B-spline-Bézier mixed surface p. tches and the joining area maintains C^2 continuously (see fig. 3).

AD-A118 973 FOREIGN TECHNOLOGY DIV WRIGHT-PATTERSON AFB OH F/G 12/1
ACTA AERONAUTICA ET ASTRONAUTICA SINICA.(U)
JUL 82
UNCLASSIFIED FTD-ID(RS)T-0518-82 NL

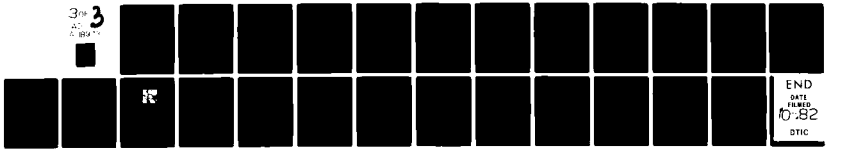

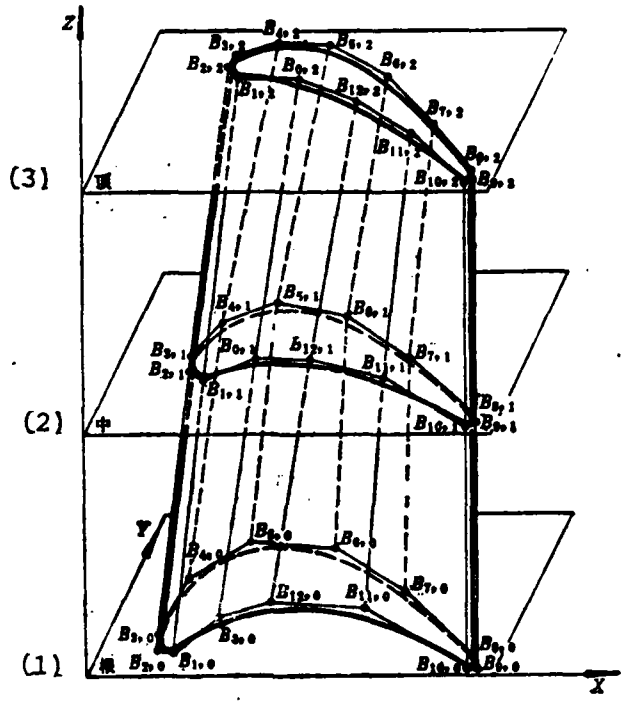

Fig. 3 Shaping by Bézier-B-Spline Mixed Patches

Key: 1. Base
2. Middle
3. Apex

The central problem of this method is giving the vertex position vortices of the sealed polygons on the three basic sections.

Naturally, it is not enough to only rely on the polygon formed from the basic points to describe the blade profile. It is also necessary to give the control points based on the special features of the different blade profiles as well as the specific requirements for each shaping. Because there are so many blade profile types there are differences in each of the

shaping requirements. Therefore, it is very difficult to give a uniform pattern. We will only list a few principles below as a reference for concrete implementation.

(1) It is best that the characteristic polygon in the leading and trailing edge areas cause the curve approximation to be round;

(2) A control point can be selected in the large curvature area near the leading edge of the blade profile;

(3) If a_i is the length of the side of the characteristic polygon and a_i is the corner of the adjacent side, then $a_i tg(a_i/2)$ can roughly realize the curve radius of this area's B-spline curve. Thus, we can use the length of the side and the corner of the control characteristic polygon to satisfy the changing tendency of the blade profile's curvature. For example, if the blade profile's curvature radius requires monotone increasing, then it is necessary for the series formed from $a_i tg\left(\frac{a_i}{2}\right)$ to also monotone increase.

3. The X-Spline Method of Blade Shaping

For convenience of narration, we called the spline method proposed in reference [5] the "X-spline." In this way, the whole blade profile is composed from a set of 3 times 2 order X-spline-Bézier mixed surfaces and the joining area maintains C^1 continuously. Its special feature is that there is interpolation in the u line. It is only necessary to properly select the apex of the polygon for the contour to be able to use the control points. The other situations are the same as the B-spline shaping method and need not be explained here.

Because the blade's configuration design not only seeks the

"beauty" of shaping but more importantly must satisfy certain aerodynamic and mechanical performance requirements, the method presented in this paper is only a designing tool for the blade's space analytical forming. Whether or not the designed blade is satisfactory it is still necessary to calculate the flow around the cascade and evaluate by means of checking velocity and pressure distribution. When compared to other shaping methods, this method is very flexible in respect to modifying the design.

IV. Design Examples

To guarantee the triangle of velocity for the aerodynamic design, we depend on engineering experience to first select initial geometric parameters for blade shaping on each basic section as shown in table 1.

(1)序号	符(2)号	(3)名称	(19)单位	叶根(20)	叶中(21)	叶顶(22)
1	r_1	前缘半径 (4)	(23) 毫米	0.66	0.8	1.06
2	r_2	后缘半径 (5)	(24) 毫米	0.36	0.38	0.68
3	β_{1k}	进口构造角(6)	(25) 度	40	59	113
4	β_{2k}	出口构造角(7)	(26) 度	29	24	22
5	ω_1	前缘楔角 (8)	(27) 度	48	48	42
6	ω_2	后缘楔角 (9)	(28) 度	6	3.6	4
7	B_w	轴向弦长 (10)	(29) 毫米	37	27.3	23.2
8	γ	安装角 (11)	(30) 度	70	46	30
9	σ	喉部半径 (12)	(31) 毫米	10.54	12.72	13.2
10	t	栅距 (13)	(32) 毫米	22.64	30	37.36
11	δ	叶背出气边转角 (14)	(33) 度	10.5	10	12
12	C_{max}	最大厚度 (15)	(34) 毫米	8.6	5.2	3.44
13	X_0	原点在基准坐标之X (16)	毫米 (35)	0	4.7	5.84
14	Y_0	原点在基准坐标之Y (17)	毫米 (36)	0	2.6	13.26
15	Z_0	原点在基准坐标之Z (18)	毫米 (37)	0	48	96

Table 1. Initial Geometric Parameters For Blade Shaping

Key: 1. Sequence number
2. Symbol
3. Name
4. Leading edge radius

Key:
5. Trailing edge radius
6. Inlet structural angle
7. Outlet structural angle
8. Leading edge wedge angle
9. Trailing edge wedge angle
10. Axial chord
11. Setting angle
12. Throat radius
13. Grid pitch
14. Exit edge corner on back of blade
15. Maxium thickness
16. Original point on basic coordinate X
17. Original point on basic coordinate Y
18. Section on basic coordinate Z
19. Unit
20. Blade root
21. Middle of blade
22. Blade apex
23. Millimeters
24. Millimeters
25. Degrees
26. Degrees
27. Degrees
28. Degrees
29. Millimeters
30. Degrees
31. Millimeters
32. Millimeters
33. Degrees
34. Millimeters
35. Millimeters
36. Millimeters
37. Millimeters

Based on the geometric relationship on the basic section, it is very easy to find basic points A, B, C, D, E, F, G and Q of the control blade profile as well as the tangent directions of related points (see fig. 4).

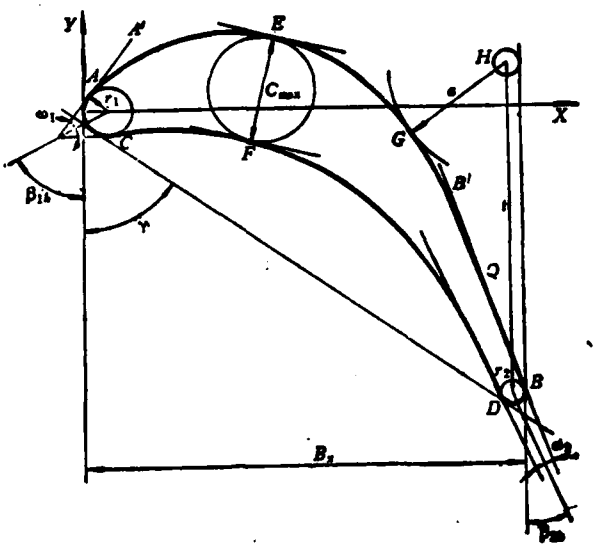

Fig. 4 Initial Geometric Parameters and Basic Points of a Blade Profile

The shaping method for B-spline and X-spline blades also requires that an additional adjustable basic point be added between the A, F point and F, G point on the back of the blade as well as one between the C, E point and E, D point on the curvature of the blade. The induced adjustable parameters KJ, KI_1 .....KI_4 and other related adjustable parameters are listed in table 2.

(1) 序号	符(2)号	名(3)称	单(13)位	叶(15)根	叶(16)中	叶(17)顶
1	F_L	F点坐标X与B_2之比 (4)	—	0.435	0.358	0.34
2	F_H	F点坐标Y与B_2之比 (5)	—	0.285	0.115	-0.17
3	α_F	F点的斜角 (6)	度(14)	-7.5	-23	-52
4	K_Q	叶背直线段可调参数 (7)	—	0.5	0.3	0.35
5	KJ	补充基础点可调参数 (8)	—	0.7	0.7	0.7
6	KI_1	补充基础点可调参数 (9)	—	0.4	0.34	0.4
7	KI_2	补充基础点可调参数 (10)	—	0.46	0.588	0.7
8	KI_3	补充基础点可调参数 (11)	—	0.5	0.6	0.6
9	KI_4	补充基础点可调参数 (12)	—	0.44	0.5	0.522

Table 2

Table 2 Adjustable Parameters of the Control Polygon

Key:
1. Sequence number
2. Symbol
3. Name
4. Ratio of F point coordinates X and B_x
5. Ratio of F point coordinates Y and B_x
6. Oblique angle of F point
7. Adjustable parameters of linear section on back of blade
8. Supplementary basic point adjustable parameters
9. Supplementary basic point adjustable parameters
10. Supplementary basic point adjustable paramenters
11. Supplementary basic point adjustable parameters
12. Supplementary basic point adjustable parameters
13. Unit
14. Degrees
15. Blade root
16. Middle of blade
17. Blade apex

In order for the leading and trailing edges to be approximately round, we formed a regular polygon by evenly dividing a central angle between two tangent points (for example, the A and C points in fig. 4) of the leading and trailing edges (as shown in fig. 5).

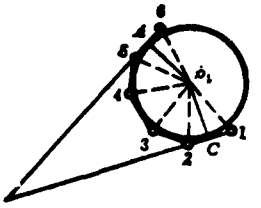

Fig. 5

Fig. 5 Formation of Polygonal Vertices at the Leading Edge of a Blade Profile

This not only controls the basic contour of the blade profile from the basic point but also guarantees shaping requirements. Moreover, depending on this, there is basically formed a control polygonal apex. The three basic sections are controlled in this way, that is, they form control polygons of the blade profile's space patches. Limited by space, this paper only lists the initial geometric parameters and adjustable parameters of the X-spline method for blade shaping in tables 1 and 2. See fig. 6 for the design results.

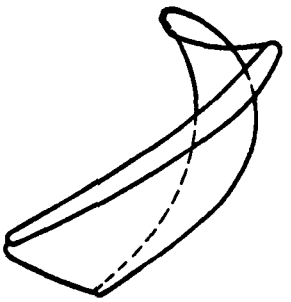

Fig. 6 Shaping a Blade by the X Spline Method

They are directly drawn on a drawing instrument by computer. Aside from this, the B-spline and Bézier methods are separately used to design the shapes of the other two blade profiles. Only the related results are drawn in figs. 7 and 8.

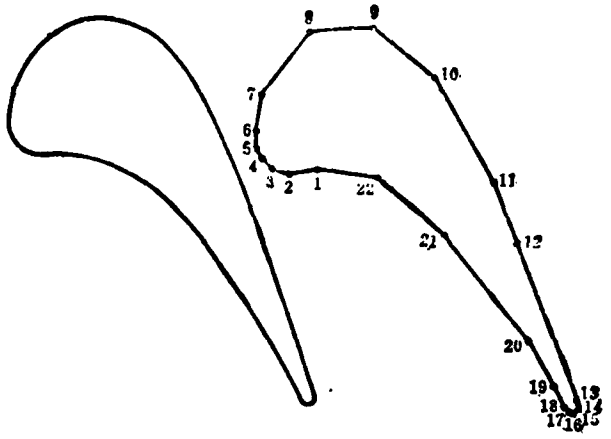

Fig. 7 A Profile Shaped by the B-Spline Method and Its Characteristic Polygon

Fig. 8 Shaping a Blade by the Bézier Method

V. Conclusion

1) After analysis and sample calculations we know that an effective new shaping method can directly and competently form the design for the space of various types of large curvature blades. The whole blade profile has an integral mathematical model which is very convenient for the computer-aided design and manufacture of blades.

2) Each of the three types of shaping methods have their special features. B-spline shaping has high patch smoothness, revisions are flexible and its localized strength gives people the feeling that its shaping curve is "flexible." The contour made by the Bézier method is "hard," its smoothness is good and its required surface patches are small. Yet, to guarantee a certain smoothness at the joining area of the surface patches it is necessary to consider special allocation of the apex. X-spline shaping lies between the two and its one outstanding point is that it has interpolation like that of the Bézier method. Moreover, it can also automatically guarantee C^1 smoothness on the patch's joining area.

3) This new shaping method is beneficial to three dimensional flow field calculations, finite element strength analysis and numerical control processing. It is also a useful tool in making an integral whole of the CAD/CAM blade. However, this is only a beginning and we must await a large quantity of design practice and the accumulation of experiences. The improvements are not sufficient especially when used for flow surface shaping. The problem of how to give the characteristic polyhedron apex position vortex based on requirements also requires detailed discussion.

References

[1] Coons, S.A., Surfaces for Computer Aided Design, Design Division Mechanical Engineering Department, Massachusetts Institute of Technology (2964), revised 1967.

[2] Bezier, P.E., Numerical Control-Mathematics and Applications, John Wiley and Sons, London 1972.

[3] Gordon, W.J. Riesenfeld, R.F., Bernstein-Bezier Methods for the Computer Aided Design of Free-Form Curves and Surfaces, J. ACM, Vol. 21, No.2, 293-319 (1974).

[4] Su Buqing and Liu Dingyuan, "Computational Geometry," Shanghai Science and Technology Press, 1981.

[5] Sun Jiachang, "A Matrix Method For Showing Curved Surfaces," 1980 Annual Meeting of International CAD.

[6] Computational Geometry Scientific Research Group of Zhejiang University, "Establishment of Computer Aided Space Surface Mathematical Model and Its Application in Torsional Processing," Scientific Research Achievement Report of Zhejiang University, 1979.

[7] Chu Yuqi, Sun Jiachang and Liu Rongguang, "Gas Turbine Blade Shaping and Its Computer Display Design," Scientific Research Work Report of Institute 608, 1979.

OVERSPEED AND OVERTEMPERATURE TESTS AND DISSECTION EXAMINATION OF THE TURBINE DISCS MADE OF A IRON-NICKEL BASE SUPERALLOY

by Guo Jianting and Zhang Jinyan
(Institute of Metal Research, Academia Sinica)

A 35 Ni-15 Cr type iron-nickel base superalloy is a sort of engine turbine disc material developed in China. It possesses outstanding comprehensive properties and microstructure stability. Therefore, it can meet the requirements of the turbine discs of aeroengines for long time use below 650~700°C. For a new type of material to be formally used in an engine it is necessary to go through long time test runs and test flights However, these types of tests are expensive and long, and so to examine the turbine disc's body and tenon it is reasonable to first conduct overspeed and overtemperature tests on the finished disc.

These tests were conducted on Chinese made vertical testers. Six thermoelectric couples are installed on different positions of the turbine disc to measure the temperature field. A photoelectric velocity measurement apparatus and gear velocity measurement apparatus are used simultaneously to measure rotation. To measure the size change of the diameter after a turbine disc overspeed test, four different position marks were made on the turbine disc prior to the test. Overtemperature tests were conducted on the third level turbine disc of a turboprop engine and the free turbine disc of a turbine axis engine.

An overspeed test (overspeed 15 percent) on the turbine disc of the turboprop engine is first carried out at normal

temperature and after operating for 5 minutes in the designed temperature field, the turbine disc successfully passed the 5 minute 15 percent overspeed examination. After examining the turbine disc it was put through overtemperature tests. The turbine disc went through a 45°C, 5 minute test under maximum design temperature.

After the turbine disc of the turbine axis engine was in a design temperature field of 10 percent and 20 percent overspeed, the engine was stopped for cooling examination and when a magnifier was used on the surface there were no abnormalities. Measurement of the diameter showed an increase of 0.61 percent, overspeed of 30 percent and after being stable for 3 minutes, examinations revealed that all was normal. Later, rotation slowly climbed to overspeed of 43 percent and there was a "pinging" sound. Immediately after stopping the engine examinations showed that the turbine disc had broken and flown out and that the blades on the disc were thrown out. Nine mortise of the disc were broken and most of the mortise locations had cracks. There were relatively light rippled flows on the surface of the disc, and the fixed screw holes became elliptical and most of the holes had cracks. Measurement of the size of the disc showed that the mean increase of the size of the diamter was a weak 1.8 percent.

We carried out dissection examination tests to understand the properties of the overspeed broken disc and to see whether there was a change in its structure.

Hardness measurement of the disc's longitudinal section showed that the hardness value was basically the same from the center to the edge. See fig. 1 for the tensile and shock tests at room temperature and 550°C.

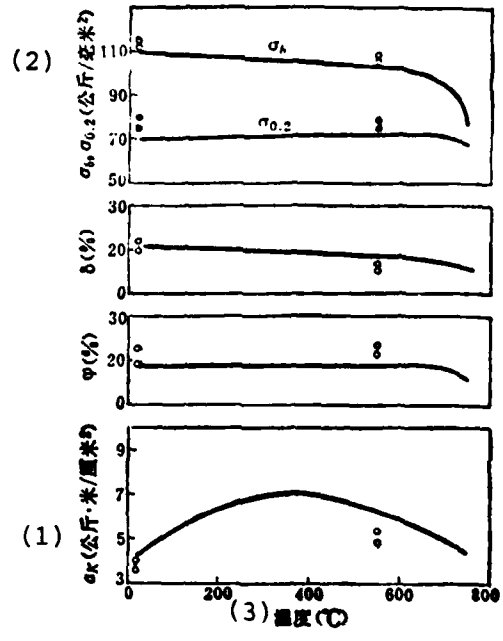

Fig. 1 Transient Mechanical Properties of the Broken Disc Under Overspeed Test (Curves - of Its Forge Disc Broken Properties; Points - of the Overspeed Disc Properties)

Key: 1. (Kilograms·meters/centimeters^2)

2. (Kilograms/millimeters^2)
3. (Temperature ($^{\circ}$C)

When compared with a turbine disc forging, tensile strength, yield strength, plasticity and toughness are on the same level. See fig. 2 for endurance time at 550 and 750°C.

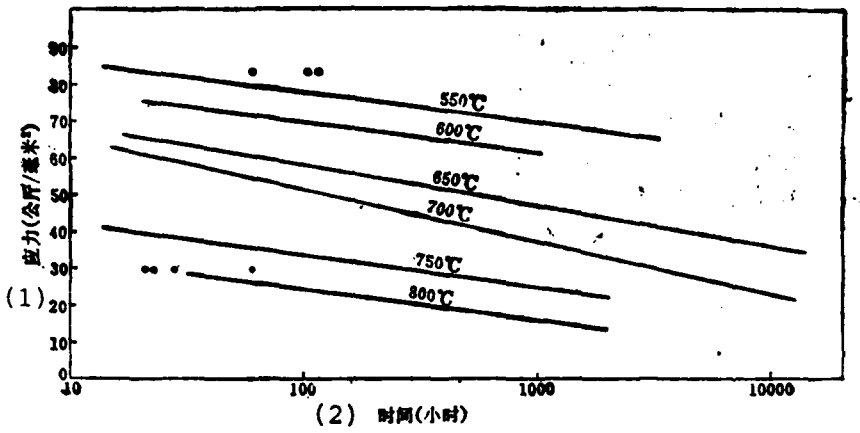

Fig. 2 Stress-Rupture Properties of the Disc Under Overspeed Test (Curves - of its Forge Disc Broken Properties; Points - of the Overspeed Disc Properties)

Key: 1. Stress (kilograms/millimeter^2)
2. Time (hours)

We can see that under 550°C, 83 kilograms/millimeter ^{2} conditions, endurance life does not drop. Under 750°C, 30 kilogram/millimeter^2 conditions, endurance time lowers.

See fig. 3 for a scanning electron micrograph of the mortise fracture of the turbine disc

Fig. 3 A Scanning Electron Micrograph of the Mortise Fracture of the Overspeed-Tested Disc (x200)

The fracture has a crystal sugar type structure and is a typical crystalline fracture. Examination of the longitudinal low multiple structure of the overspeed broken disc shows that the structure is normal and there are no low multiple alloy defects. See fig. 4 for the metal phase structure.

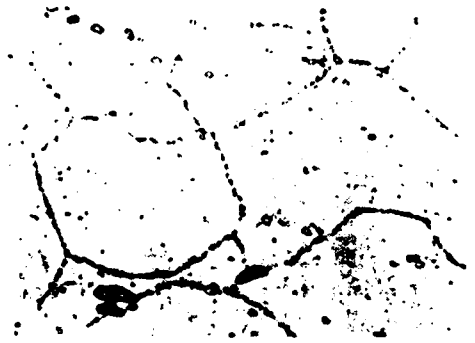

Fig. 4

Fig. 4 Metal Phase Structure of the Overspeed-Tested Disc (x500)

Aside from the TiC and M_3B_2 seen in the normal structure, there were no abnormal phases or abnormal structures. The quantity of carbides is 0.58 percent which is the same as the quantity of TiC contained in the normal structure of the 35Ni-15Cr alloy. There is about 15 percent γ' phase in the alloy and this is the major strength phase of the alloy. Yet, because its diameter is only about 500 Å, the metal phase photo is not shown. Aside from this, the alloy also contains a minute amount of σ phase. Long time testing of 2,000 hours showed that this quantity of σ phase had a very small effect on performance and use.

Because the results of the overspeed and overtemperature tests were excellent, after all of the turbine discs were installed in the engine they underwent multiple trial runs. Several types of engines withstood all of the long-time trial flight tests.

We can derive the following conclusions from the above test results:

Turbine discs manufactured from 35Ni-15Cr type iron-nickel base superalloy successfully withstood 10, 15, 20 and 30 percent overspeed tests. The former also smoothly underwent 45°C overtemperature tests and the situation was excellent. From calculations of overspeed broken rotating velocity, the latter's safety coefficient reached to about 1.43.

The transient strength, plasticity and toughness of the overspeed broken disc, the endurance time of 550°C and the hardness from the center to the edge can still maintain the original levels. Low multiple and metal phase structures are normal.

We would like to express our thanks to the comrades of the Zhuzhou Engine Research Institute, Dongan Machinery Plant and Hongxiangjiang Machine Plant for their participation in the testing.

THE DELEGATION OF CSAA TOOK PART IN THE FIRST INTERNATIONAL AEROSPACE SYMPOSIUM IN PARIS

A delegation of four people from the CSAA led by Shen Yuan, director of the CSAA, took part in the First International Aerospace Symposium held in Paris from June 2 to 3 of 1981.

This symposium was proposed and sponsored by the United States Department of Commerce, United States Airforce and United States Aerospace Bureau, was agreed upon by the Aerospace Industry Federation of France, and was arranged by the United States Association of Aeronautics and Astronautics.The stated aim of the conference was to "promote the true international understanding in the quality of aeronautics and astronautics and provide an opportunity for beneficial exchange among the aerospace nations of the world." When considering the "leaders of the aeronautics circles of each nation, the Paris Aeronautics Exhibition was the most magnificent as well as the most pleasing site." Therefore, the Paris exhibition site was chosen and during the two days prior to the exhibit the symposium was convened there. The United States proposed that the exhibit hall be the location of the first symposium and hoped that this type of symposium would be convened once a year in the future.

The general membership preparatory committee invited 250 representatives from over 20 nations to participate in the symposium including the United States, France, England, West Germany, Japan, Italy etc. Prior to the meeting, the Soviet Union had confirmed that they would participate but they did not attend the meeting. There were also reporters from various nations.

The symposium was divided into four units and each unit was held for one half day. The speakers were invited and issued written materials before the meeting. During the two days a total of 25 papers were delivered.

The general subject of the first morning were government policies and plans in aeronautics and astronautics. The speakers were all technical leaders of each nation's aerospace science and technology leading organization or large research units. The contents included: 1. a speech by Luofulaisi, Deputy of the United States Department of Aeronautics and Astronautics, on the policies of that department; 2. a speech by Professor Telela, Head of the European Bureau of Space Technology, on the policies of that bureau; 3. a speech by Yoshiki, Chairman of the Japanese Commission on Space Enterprises, on Japan's space activities and plans; 4. a speech by General Smith, Chief of the General Staff of the European Alliance, on the military use of aeronautics and astronautics; 5. a speech by Shen Yuan on certain aspects of China's aeronautics and astronautics; 6. a speech by Kelukasi, Chairman of the World Communications Satellite Association, on the use of satellites for international communications; 7. a speech by Haweilan-Faerke, Chief Engineer of France's Dasuo Company, on the problems of the military use of aeronautics and international policies. Shen Yuan's speech was well received by the members and was helpful for foreign nations to understand the past and present developments of China's aerospace enterprises, related Chinese policies, and the general situation of China's aeronautical education. The 250 copies of the speech carried by our delegation were very quickly distributed and after the symposium there was still a demand for them. This speech was printed in abstract form in the Daily News of the Aerospace Exhibition.

The main speeches of the second unit were speeches by Caisi Taile, Vice President of the Being Company, on the development of transporters in the 1980's; Simoerwote, Marshal of the Royal Airforce and Advisor to the British Aerospace Company, on the

future military use of aircraft; and Professor Bosangkentang, Director of the International Cooperation Department of France's Aerospace Research Institute, on the institute's research work. The main speeches of the third unit were by Bulacai, Director of the Applied Plans Department of France's Aerospace Research Institute, on the prospects of space technology for ground observations; Professor Dengnisi, Chairman of the Space Research Committee, on space science and international plans; Cailierlike, Vice President of the Luokeweier International Company, on space transport systems. It was originally planned that Liuming, astronaut of the "Salute 6", was to give a speech on the use of orbiting space stations and their effects on the people's economy but this did not come about. The first half of the fourth unit were speeches by Caiqiewalei, Vice President of the French Aerospace Company, on civil aviation; Cailuojiesi, Vice President in charge of international plans for the F-16 at the General Motors Company of the United States, on the prospects of the military use of aircraft etc.. The second half were speeches by the American astronauts Young and Kilibenzuo, on the first orbital flight of a spacecraft.

After the symposium, the Chinese delegation also accepted French invitations to visit the "Alian" delivery vehicle manufacturing plant, the Paris Aerospace Exhibit, the French Aerospace Research Institute in Paris, and two aviation schools in Toulouse.

A SUCCESSFUL CONFERENCE ON TRANSONIC AERODYNAMICS

The China Aeodynamics Research Committee, China Aviation Committee and China Aerospace Institute jointly sponsored a Transonic Aerodynamics Conference in Xian from May 26 to 30.

Transonic aerodynamics includes both subsonic and supersonic aerodynamics and the complex phenomena of their existing shock boundary layers are difficult to study and calculate. Because of the application of electronic computers, research work on transonics has developed quickly. In recent years, China's aerodynamics researchers have given full attention to the problems of this area and have attained pleasing results. There were 74 professors, specialists and engineers from 31 units participating in this academic conference and 42 papers were read, each of which discussed in detail technical problems in transonic aerodynamics. This conference had the effect of further promoting Chinese research in this area.

THE CSAA SPONSORED CONFERENCE ON GEARS AND REDUCERS IN AIRCRAFT

The CSAA sponsored a conference on gears and reducers in aircraft in Changsha from June 12 to 17 of 1981. This was the first national special conference on gears and reducers in aircraft. The conference received 65 papers on design, technology, testing and measuring, 45 of which were delivered. Other related specialists were invited to the conference to give special reports on the developments of gears and reducers in aviation both domestically and abroad.

The papers received by the conference revealed the following outstanding features: firstly, because of the high speed and heavy load features of aviation gears, the finite element method has been widely applied for stress analysis so as to raise the gear's strength design level. Secondly, research on the design and technology of the height and shape of aviation gear teeth have attained new advancements as well as certain achievements in reducing gear transmission noise and vibration. Furthermore, the most recent research achievements on the development and application of gear integral error analysis and the integral error measurer were also reported at the conference. These topics drew enthusiastic interest from the participants. Several papers systematically introduced the newest technology recently imported from abroad for the design, manufacture, testing and measuring of gears and reducers in power sets. This was given special attention by related specialists who considered many of the new techniques quite worthy of study and research.

During the conference, they also heard an introduction on formulating "criterion for gear strength in aviation" and also held discussions on this special topic. All of the participants considered this item of work of great significance, that is, to overcome many difficulties to attain achievements and to gain results as quickly as possible. They also offered valuable and constructive suggestions for future work.

To sum up, the participants considered that this conference reflected the new levels of scientific research, design and production of aviation gears and reducers in China. The academic atmosphere of the conference was enthusiastic, the representatives spoke out freely and discussions were lively. Anticipated goals were reached and excellent goals were attained. Finally, proposals were made on the questions of the arrangements of future activities and the establishment of specialized academic organizations.

FIRST CONFERENCE ON SCIENTIFIC MANAGEMENT SPONSORED BY THE CSAA

The CSAA convened the First Conference on Scientific Management from July 18 to 22 of 1981 in Chengdu, The conference had two aims: one was academic exchange and the other was deliberations on the setting up of a corresponding academic organiztion. Over 90 papers were collected at the conference and among these some were delivered and some exchanged in small groups. The contents of the papers widely reflected the basic research developments of scientific management in the aviation industry and also discussed the various problems of organization, using qualified personnel, economic quality and systems analysis, planned appraisals and behavioral science.

The conference opened with enthusiasm and the representatives spoke freely thus realizing an academic atmosphere of letting a hundred flowers bloom and a hundred schools contend. Specially invited representatives gave speeches on "Scientific Policy-Making and Modern Brain Trusts," "Modern Leadership Techniques," :The Application of the Network Method in the Launching of Chinese Carrier Rockets" etc. which were warmly received by the representatives. The papers acted to expand everyone's scope and raise their understanding. The participants further comprehended that scientific policy-making is the key to the realization of making management scientific, is an important factor in guaranteeing successful development in social, economic, scientific

and educational areas, and is also a basic indication of testing the level of leadership.

The conference addressed itself to the problems of the development, planned management, scientific research management and economic quality of China's new organizations, and held discussions in small groups. The representatives integrated past model developments, introduced special research experiences and summarized lessons. It was unanimously considered that model development and special research should handle well scientific policy-making and also should use the network method to guarantee coordination between the various systems. In this way, management will become scientific and raise economic achievements.

To sum up, after participating in the conference, the comrades understood that the scientific management discussed was not the general planning and management work of the past but a new branch of learning which integrates the social sciences and natural sciences. Therefore, the representatives agreed to set up a Chinese Aeronautics Conference Scientific Management Special Academic Organization to further promote the future development of management science.

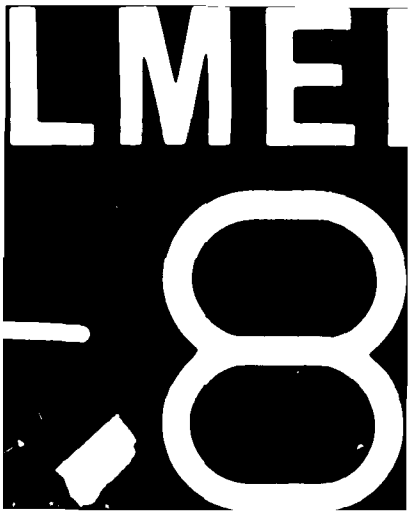
LME
8